MESOSCALE EDDIES AND SEA SURFACE TEMPERATURE FRONTS IN EASTERN BOUNDARY CURRENT SYSTEMS

by

CAITLIN M. AMOS

(Under the Direction of Renato M. Castelao)

ABSTRACT

Eastern Boundary Current Systems (EBCS) are highly productive ecosystems due to upwelling that brings cold, nutrient-rich waters to the surface along the coasts. The distribution of the upwelled water can be influenced by several physical processes in these regions, which can impact biological activity. Satellite-derived measurements of particulate organic carbon (POC) are used as a tracer of coastal water to quantify the eddy-induced offshore enrichment of POC in the California Current System (CCS). Cyclonic eddies located offshore that were generated near the coast in general contain higher POC concentrations in their interior than cyclones of similar size generated locally offshore. This analysis was expanded to the other major EBCS, revealing regions within each EBCS where the offshore transport of POC by eddies is most important. These regions are often associated with upwelling jet separation, which helps produce favorable conditions for eddy-induced transport of coastal water to occur. These results provide large-scale observational-based evidence that nonlinear cyclonic eddies can trap and

transport coastal water offshore. This mechanism can substantially widen the area influenced by highly productive upwelled waters in the EBCS and influence the marine ecosystems. EBCS also feature sea surface temperature (SST) fronts that form between cold, upwelled water and warmer offshore water. Thirty-seven years of satellite SST data are used to detect SST fronts in the two eastern Pacific Ocean EBCS to investigate the interannual variability of fronts due to the El Niño-Southern Oscillation (ENSO). Results indicate that frontal activity generally decreases during El Niño events and increases during La Niña events along most of the coastline in both regions. Satellite measurements of wind stress and sea level anomaly were utilized to investigate the oceanic and atmospheric forcing mechanisms associated with ENSO and how they affect frontal activity. This analysis revealed regions in both EBCS where one mechanism is likely dominant and regions that are influenced by both forcing mechanisms. Overall, this dissertation expands our understanding of the physical dynamics associated with upwelling in the EBCS and how they may influence the marine ecosystems.

INDEX WORDS: coastal oceanography, Eastern Boundary Current Systems, upwelling, mesoscale eddies, offshore transport, particulate organic carbon, sea surface temperature fronts, El Niño-Southern Oscillation, satellite observations

MESOSCALE EDDIES AND SEA SURFACE TEMPERATURE FRONTS IN EASTERN BOUNDARY CURRENT SYSTEMS

by

CAITLIN M. AMOS

BS, North Carolina State University, 2016

A Dissertation Submitted to the Graduate Faculty of The University of Georgia in Partial Fulfillment of the Requirements for the Degree

DOCTOR OF PHILOSOPHY

ATHENS, GEORGIA

2021

MESOSCALE EDDIES AND SEA SURFACE TEMPERATURE FRONTS IN EASTERN BOUNDARY CURRENT SYSTEMS

by

CAITLIN M. AMOS

Major Professor:	Renato M. Castelao
Committee:	Adrian Burd
	Daniela Di Iorio
	Catherine Edwards
	Melanie Fewings

Electronic Version Approved:

Ron Walcott
Vice Provost for Graduate Education and Dean of the Graduate School
The University of Georgia
December 2021

ACKNOWLEDGEMENTS

I am sincerely grateful to my advisor, Dr. Renato Castelao, for encouraging me to pursue a PhD and supporting me along the way. He helped develop me into the researcher I am now through his mentoring and guidance. He challenged me to think more critically and problem solve and helped me to become a more knowledgeable and confident researcher. I'm also thankful for his encouragement and guidance in applying for NASA's Earth and Space Science Fellowship, which has financially support me during much of my PhD. I'm truly thankful for his emotional, intellectual, and financial support during my PhD journey.

I also want to thank my committee members, Drs. Adrian Burd, Melanie, Fewings, Catherine Edwards, and Daniela Di Iorio, who provided helpful guidance, suggestions, and support during my PhD. A special thank you to Melanie for helping me find an amazing cruise opportunity and for your hospitality while in Oregon. I want to thank Dr. Brock Woodson for also providing guidance and feedback on my research.

My PhD would not have been possible without the generous support from my family and friends. To my family, especially my parents, thank you for your continuous love and support during this journey. Even if you never really understood what I was researching, you still encouraged me to succeed and become who I am today. Special thanks to my partner, Shep, for his love, support, and encouragement; I'm so happy that grad school brought us together. I also appreciate you teaching me about "biology stuff"

and helping me with statistics. Thank you to all of my friends, both inside and outside of marine sciences, old and new. I could name you all here but that would take up a lot of room. To all of you, thanks for providing lots of laughter, entertainment, support, food, beer, and much more over the years. I'd also like to thank my lab mates, Carolina Ernani Da Silva, Hilde Oliver, and Sudip Majumder. I learned a lot from our numerous conversations about research and how to code things in MATLAB, and enjoyed sharing delicious meals with you all.

Lastly, to my feathered friends – Eliza, Mulan, Polla, Petunia, Dodo, Spot, Red Stripe, and Oreo – thank you for providing endless entertainment, stress relief, and lots of eggs during the last year of my PhD.

TABLE OF CONTENTS

Page

LIST OF TABLES

Page

LIST OF FIGURES

Page

CHAPTER 1

INTRODUCTION AND LITERATURE REVIEW

The physical, chemical, and biological processes occurring in Eastern Boundary Current Systems (EBCS) have been the subject of great interest for the last several decades. The four major EBCS are the California and Humboldt Current Systems in the eastern Pacific Ocean and the Canary and Benguela Current Systems in the eastern Atlantic Ocean. These systems are associated with large-scale anticyclonic flow, and with coastlines generally aligned in the meridional direction, these regions are favorable for coastal upwelling (Bakun and Nelson, 1991). Prevailing equatorward winds blowing parallel to the coastline during local summer result in offshore Ekman transport and upwelling along the coast, bringing cold, nutrient-rich waters to the surface and creating highly productive ecosystems in these regions (Huyer, 1983; Carr and Kearns, 2003). Winds generally switch during local winter and flow poleward which pushes water inshore and causes downwelling. The overall goal of the research presented in this dissertation is to expand our understanding of the physical dynamics associated with upwelling in EBCS by utilizing satellite observations. Satellites have made it possible to study large regions of the surface ocean, filling in gaps where in situ observations are lacking.

In the EBCS, coastal upwelling leads to a strong cross-shore gradient in physical and biogeochemical properties, with cold, nutrient-rich water near the coast and warm,

low-nutrient water offshore (Bakun and Nelson, 1991; Carr, 2001; Carr and Kearns, 2003; Chavez and Messié, 2009; Letelier et al., 2009). The upwelling can also produce a strong equatorward alongshore jet in geostrophic balance with upwelled isopycnals that generally forms at the surface along the boundary of the coastal upwelling (Huyer, 1983; Strub and James, 2000). The upwelled isopycnals create vertical shear in the alongshore velocities (strong equatorward flow near the surface and weaker equatorward or even poleward flow at depth) which is in thermal wind balance with the cross-shelf density gradients. Early EBCS studies focused on two-dimensional upwelling, which explains a lot of the physical dynamics in these systems but is constrained to a narrow offshore extent (<50 km; e.g., Huyer and Smith, 1974; Barton et al., 1977; Allen, 1980; Brink et al., 1983; Huyer, 1983; Allen et al., 1995).

Several studies over the last few decades have shown that the upwelling circulation in EBCS can be highly three-dimensional, however, with the upwelling jet often separating from the coast at topographic perturbations and with the formation of meanders, filaments and high mesoscale activity (e.g., Lynn and Simpson, 1987; Batteen et al., 1995; Barth et al., 2000; Batteen et al., 2000; Strub and James, 2000; Relvas and Barton, 2002; Chaigneau et al., 2009; Letelier et al., 2009; Meunier et al., 2012; Castelao and Luo, 2018). Three-dimensional aspects of upwelling account for a wider area (several hundreds of kilometers offshore) that is influenced by upwelling circulation via several processes, including jet separation and the formation of filaments (e.g., Bakun and Nelson, 1991; Barth et al., 2005; Wang et al., 2015; Lovecchio et al., 2018). For example, studies have shown that jet separation and filament formation can result in large fluxes of heat, salt and biogeochemical properties for up to 500 km from the coast in many sectors

of EBCS (e.g., Lovecchio et al., 2018). Another process that has received more attention recently involves the transport of water by nonlinear mesoscale eddies (radius on the order of 100 km), which are ubiquitous features in EBCS (Haynes and Barton, 1991; Ramp et al., 1991; Strub et al., 1991; Capet et al., 2008; Chaigneau et al., 2009; Chelton et al., 2011). Eddies are generated through barotropic and baroclinic instabilities in the alongshore currents and jets in the EBCS (Strub et al., 1991; Strub and James, 2000; Marchesiello et al., 2003; Capet et al., 2008; Kurian et al., 2011) and then propagate westward in the EBCS (Chelton et al., 2011; Kurian et al., 2011; Nagai et al., 2015). In the nearshore region, barotropic and baroclinic instabilities associated with horizontal shears and horizontal density gradients in the jet, respectively, lead to the conversion of energy from the mean flow to the meander and eddy fields. In the offshore region, the upwelling jet has moved away from the stabilizing effect of the sloping continental margin bathymetry and baroclinic instabilities in the jet become the main source of energy for producing eddies (Marchesiello et al., 2003; Capet et al., 2008). When these eddies are nonlinear (the ratio of their rotational speed to translational speed is greater than 1) they can theoretically trap water parcels and associated properties during formation (Chelton et al., 2011). Eddies that form near the coast in the EBCS can potentially trap and redistribute the nutrient-rich upwelled water for hundreds of kilometers offshore, influencing the horizontal and vertical distribution of biogeochemical properties both near the coast and in the offshore region (Gruber et al., 2011; Combes et al., 2013; Nagai et al., 2015; Chenillat et al., 2016; Lovecchio et al., 2018).

Modeling studies support this idea and have suggested that eddies contribute to the redistribution of carbon, nutrients, and other properties in upwelling systems (Liang et al., 2009; Combes et al., 2013; Nagai et al., 2015; Chenillat et al., 2016; Lovecchio et al., 2018). Previous observational studies have shown individual examples of eddies transporting materials in various regions of the ocean (Crawford et al., 2007; Lehahn et al., 2011; Gaube et al., 2014; Gaube and McGillicuddy Jr., 2017), however no large-scale observational study has systematically quantified eddy-induced transport and its influence on carbon distribution in highly productive upwelling systems. The redistribution of upwelled, coastal water that is rich in carbon and nutrients could have important implications for the marine ecosystems in the EBCS. Therefore, quantifying the eddy-induced transport using large-scale observations is important for further understanding the influence of eddies in these systems. Chapters 2 and 3 address this using satellite-derived measurements of particulate organic carbon (POC) as a tracer of coastal water to quantify the offshore transport of coastal upwelled water by mesoscale eddies in EBCS.

In chapter 2, a procedure is developed to isolate the satellite-derived POC anomalies associated with mesoscale eddies in the California Current System (CCS). POC is a useful tracer of coastal water because concentrations are highest near the coast due to the coastal upwelling and are much lower offshore. As cyclonic eddies (rotating counterclockwise in the Northern Hemisphere) form near the coast, they can potentially trap the coastal water containing high concentrations of POC and transport it offshore. Eddies generated in the offshore region outside of the upwelling zone contain lower concentrations of POC compared to those eddies generated near the coast that propagated

offshore. The POC anomalies associated with these two groups of cyclonic eddies are used to quantify the eddy-induced offshore enrichment of POC. The analyses presented in this chapter provides large-scale observational evidence that eddies can indeed trap coastal water in their interior as they propagate offshore in the CCS.

The four major EBCS share similarities in mesoscale eddy activity and upwelling dynamics (e.g., Chaigneau et al., 2009; Chavez and Messié, 2009; Pegliasco et al., 2015; Wang et al., 2015; Yuan and Castelao, 2017), therefore, eddy-induced offshore transport of coastal water may also be important in the other EBCS. Chapter 3 explores this by applying the procedure developed in chapter 2 to the other major EBCS, the Humboldt, Canary, and Benguela Current Systems (HCS, CanCS, and BCS, respectively). The offshore enrichment of POC due to cyclonic eddies is quantified in each EBCS. There are also many differences among these systems, including the degree of spatial variability within each EBCS with regard to upwelling, jet separation, and mesoscale activity (Chaigneau et al., 2009; Chavez and Messié, 2009; Chelton et al., 2011; Strub et al., 2013; Wang et al., 2015; Yuan and Castelao, 2017). This led to the hypothesis that the eddy-induced transport mechanism that was investigated in chapter 2 will also vary spatially within these systems. This is explored in chapter 3 by quantifying the volume transport and offshore enrichment of POC by eddies in subregions within each EBCS and identifying regions where eddy-induced transport is most important.

In addition to mesoscale eddies, SST fronts are also ubiquitous features associated with upwelling in EBCS (Castelao et al., 2006; Letelier et al., 2009; Meunier et al., 2012; Nieto et al., 2012; Santos et al., 2012; Vazquez-Cuervo et al., 2013; Wang et al., 2015; Veitch and Penven, 2017; Oerder et al., 2018; Mauzole et al., 2020). Upwelling often

establishes sea surface temperature (SST) fronts that separate cold, upwelled water along the coast from warmer offshore waters (Kostianoy and Lutjeharms, 1999). Fronts are characterized by convergent flow at the surface, making them hotspots for biological activity. As free-floating biota accumulate in the frontal zone, higher trophic levels are attracted to these regions, establishing productive food webs (Walsh, 1977; Bowman, 1978; Chavez and Messié, 2009; Woodson and Litvin, 2015). The upwelling jet that forms at the surface along the upwelling front (Huyer, 1983) makes the locations of SST fronts good proxies for the location of flow intensification in these regions (Strub and James, 2000).

In the CCS and HCS, the two EBCS located in the eastern Pacific Ocean, fronts have been shown to exhibit latitudinal and seasonal variability, largely due to the seasonality of upwelling (Strub et al., 1998; Letelier et al., 2009; Kahru et al., 2012; Vazquez-Cuervo et al., 2013; Castelao and Wang, 2014; Wang et al., 2015; Wang et al., 2021) and mesoscale dynamics (Kahru et al., 2012; Vazquez-Cuervo et al., 2013; Yuan and Castelao, 2017) in these regions. Interannual variability in wind patterns, sea level anomaly (SLA), and SST anomalies have been linked to large-scale climatic indices, such as the El Niño-Southern Oscillation (ENSO; e.g., Enfield and Allen, 1980; Huyer et al., 1987; Meyers et al., 1998; Strub et al., 1998; Ulloa et al., 2001; Carr et al., 2002; Huyer et al., 2002; Schwing et al., 2002; Strub and James, 2002; Macias et al., 2012; Jacox et al., 2014; Jacox et al., 2015; Stramma et al., 2016; Espinoza-Morriberón et al., 2017). Although a clear link has been identified between ENSO events and these physical dynamics, which affect coastal upwelling in the CCS and HCS, the role that ENSO plays in the interannual variability of SST fronts has received less attention (Kahru et al., 2018;

Wang et al., 2021). Chapter 4 aims to fill this void by investigating the interannual variability of SST fronts using satellite observations of SST. SST gradients are computed from satellite SST measurements and used to detect fronts along the west coasts of North and South America using an edge-detection algorithm (Canny, 1986) following Castelao et al. (2006) and Wang et al. (2015). Satellite measurements of sea level anomaly and wind stress are also utilized to investigate the oceanic and atmospheric forcing mechanisms associated with ENSO and how they influence frontal activity.

The main findings of this dissertation are summarized in chapter 5. Also included in chapter 5 are suggestions for future work to expand on the analyses and results presented in chapters 2-4.

References

Allen, J. (1980), Models of wind-driven currents on the continental shelf, *Annual Review of Fluid Mechanics*, *12*(1), 389-433, doi:10.1146/annurev.fl.12.010180.002133.

Allen, J., P. Newberger, and J. Federiuk (1995), Upwelling circulation on the Oregon continental shelf. Part I: Response to idealized forcing, *Journal of Physical Oceanography*, *25*(8), 1843-1866, doi:10.1175/1520-0485(1995)025<1843:UCOTOC>2.0.CO;2.

Bakun, A., and C. S. Nelson (1991), The Seasonal Cycle of Wind-Stress Curl in Subtropical Eastern Boundary Current Regions, *Journal of Physical Oceanography*, *21*(12), 1815-1834, doi:10.1175/1520-0485(1991)021<1815:TSCOWS>2.0.CO;2.

Barth, J. A., S. D. Pierce, and T. J. Cowles (2005), Mesoscale structure and its seasonal evolution in the northern California Current System, *Deep-Sea Research II*, *52*(1-2), 5-28, doi:10.1016/j.dsr2.2004.09.026.

Barth, J. A., S. D. Pierce, and R. L. Smith (2000), A separating coastal upwelling jet at Cape Blanco, Oregon and its connection to the California Current System, *Deep-Sea Research II*, *47*, 783-810, doi:10.1016/S0967-0645(99)00127-7.

Barton, E. D., A. Huyer, and R. L. Smith (1977), Temporal variation observed in the hydrographic regime near Cabo Corveiro in the northwest African upwelling region, February to April 1974, *Deep Sea Research*, *24*(1), 7-23, doi:10.1016/0146-6291(77)90537-9.

Batteen, M. L., C.-P. Hu, J. L. Bacon, and C. S. Nelson (1995), A numerical study of the effects of wind forcing on the Chile Current System, *Journal of Oceanography*, *51*(5), 585-614, doi:10.1007/BF02270526.

Batteen, M. L., J. R. Martinez, D. W. Bryan, and E. J. Buch (2000), A modeling study of the coastal eastern boundary current system off Iberia and Morocco, *Journal of Geophysical Research: Oceans*, *105*(C6), 14173-14195, doi:10.1029/2000JC900026.

Bowman, M. J. (1978), Oceanic fronts in coastal processes, in *Oceanic Fronts in Coastal Processes*, edited by M. Bowman and W. Esias, pp. 2-5, Springer, NY.

Brink, K., D. Halpern, A. Huyer, and R. Smith (1983), The physical environment of the Peruvian upwelling system, *Progress in Oceanography*, *12*(3), 285-305, doi:10.1016/0079-6611(83)90011-3.

Canny, J. (1986), A Computational Approach to Edge Detection, *IEEE Transactions on Pattern Analysis and Machine Intelligence*, *PAMI-8*(6), 679-698, doi:10.1109/TPAMI.1986.4767851.

Capet, X., F. Colas, J. C. McWilliams, P. Penven, and P. Marchesiello (2008), Eddies in eastern boundary subtropical upwelling systems, *Ocean Modeling in an Eddying Regime*, *177*, 350, doi:10.1029/177GM10.

Carr, M.-E. (2001), Estimation of potential productivity in Eastern Boundary Currents using remote sensing, *Deep Sea Research Part II: Topical Studies in Oceanography*, *49*(1-3), 59-80, doi:10.1016/S0967-0645(01)00094-7.

Carr, M.-E., and E. J. Kearns (2003), Production regimes in four Eastern Boundary Current systems, *Deep Sea Research Part II: Topical Studies in Oceanography*, *50*(22-26), 3199-3221, doi:0.1016/j.dsr2.2003.07.015.

Carr, M. E., P. T. Strub, A. C. Thomas, and J. L. Blanco (2002), Evolution of 1996–1999 La Niña and El Niño conditions off the western coast of South America: a remote sensing perspective, *Journal of Geophysical Research: Oceans*, *107*(C12), 29-21-29-16, doi:10.1029/2001JC001183.

Castelao, R. M., and H. Luo (2018), Upwelling jet separation in the California Current System, *Scientific Reports*, *8*, 16004, doi:10.1038/s41598-018-34401-y.

Castelao, R. M., T. P. Mavor, J. A. Barth, and L. C. Breaker (2006), Sea surface temperature fronts in the California Current System from geostationary satellite observations, *Journal of Geophysical Research*, *111*, C09026, doi:10.1029/2006jc003541.

Castelao, R. M., and Y. Wang (2014), Wind-driven variability in sea surface temperature front distribution in the California Current System, *Journal of Geophysical Research: Oceans*, *119*, 1861-1875, doi:10.1002/2013jc009531.

Chaigneau, A., G. Eldin, and B. Dewitte (2009), Eddy activity in the four major upwelling systems from satellite altimetry (1992–2007), *Progress in Oceanography*, *83*, 117-123, doi:10.1016/j.pocean.2009.07.012.

Chavez, F. P., and M. Messié (2009), A comparison of Eastern Boundary Upwelling Ecosystems, *Progress in Oceanography*, *83*, 80-96, doi:10.1016/j.pocean.2009.07.032.

Chelton, D. B., M. G. Schlax, and R. M. Samelson (2011), Global observations of nonlinear mesoscale eddies, *Progress in Oceanography*, *91*, 167-216, doi:10.1016/j.pocean.2011.01.002.

Chenillat, F., P. J. S. Franks, and V. Combes (2016), Biogeochemical properties of eddies in the California Current System, *Geophysical Research Letters*, *43*, 5812-5820, doi:10.1002/2016gl068945.

Combes, V., F. Chenillat, E. Di Lorenzo, P. Rivière, M. D. Ohman, and S. J. Bograd (2013), Cross-shore transport variability in the California Current: Ekman upwelling vs. eddy dynamics, *Progress in Oceanography*, *109*, 78-89, doi:10.1016/j.pocean.2012.10.001.

Crawford, W. R., P. J. Brickley, and A. C. Thomas (2007), Mesoscale eddies dominate surface phytoplankton in northern Gulf of Alaska, *Progress in Oceanography*, *75*, 287-303, doi:10.1016/j.pocean.2007.08.016.

Enfield, D. B., and J. S. Allen (1980), On the Structure and Dynamics of Monthly Mean Sea Level Anomalies along the Pacific Coast of North and South America, *Journal of Physical Oceanography*, *10*, 557-578, doi:10.1175/1520-0485(1980)010<0557:OTSADO>2.0.CO;2.

Espinoza-Morriberón, D., V. Echevin, F. Colas, J. Tam, J. Ledesma, L. Vásquez, and M. Graco (2017), Impacts of El Niño events on the Peruvian upwelling system productivity, *Journal of Geophysical Research: Oceans*, *122*(7), 5423-5444, doi:10.1002/2016JC012439.

Gaube, P., and D. J. McGillicuddy Jr. (2017), The influence of Gulf Stream eddies and meanders on near-surface chlorophyll, *Deep-Sea Research I*, *122*, 1-16, doi:10.1016/j.dsr.2017.02.006.

Gaube, P., D. J. McGillicuddy Jr., D. B. Chelton, M. J. Behrenfeld, and P. G. Strutton (2014), Regional variations in the influence of mesoscale eddies on near-surface chlorophyll, *Journal of Geophysical Research: Oceans*, *119*, 8195-8220, doi:10.1002/ 2014JC010111.

Gruber, N., Z. Lachkar, H. Frenzel, P. Marchesiello, M. Münnich, J. C. McWilliams, T. Nagai, and G.-K. Plattner (2011), Eddy-induced reduction of biological production in eastern boundary upwelling systems, *Nature Geoscience*, *4*, 787-792, doi:10.1038/ngeo1273.

Haynes, R., and E. D. Barton (1991), Lagrangian observations in the Iberian coastal transition zone, *Journal of Geophysical Research: Oceans*, *96*(C8), 14731-14741, doi:10.1029/91JC00907.

Huyer, A. (1983), Coastal upwelling in the California Current System, *Progress in Oceanography*, *12*, 259-284, doi:10.1016/0079-6611(83)90010-1.

Huyer, A., and R. L. Smith (1974), A subsurface ribbon of cool water over the continental shelf off Oregon, *Journal of Physical Oceanography*, *4*(3), 381-391, doi:10.1175/1520-0485(1974)004<0381:ASROCW>2.0.CO;2.

Huyer, A., R. L. Smith, and J. Fleischbein (2002), The coastal ocean off Oregon and northern California during the 1997-9 El Niño, *Progress in Oceanography*, *54*, 311-341, doi:10.1016/S0079-6611(02)00056-3.

Huyer, A., R. L. Smith, and T. Paluszkiewicz (1987), Coastal upwelling off Peru during normal and El Niño times, 1981–1984, *Journal of Geophysical Research: Oceans*, *92*(C13), 14297-14307, doi:10.1029/JC092iC13p14297.

Jacox, M. G., J. Fiechter, A. M. Moore, and C. A. Edwards (2015), ENSO and the California Current coastal upwelling response, *Journal of Geophysical Research: Oceans*, *120*, 1691-1702, doi:10.1002/ 2014JC010650.

Jacox, M. G., A. M. Moore, C. A. Edwards, and J. Fiechter (2014), Spatially resolved upwelling in the California Current System and its connections to climate variability, *Geophysical Research Letters*, *41*, 3189-3196, doi:10.1002/2014gl059589.

Kahru, M., E. Di Lorenzo, M. Manzano-Sarabia, and B. G. Mitchell (2012), Spatial and temporal statistics of sea surface temperature and chlorophyll fronts in the California Current, *Journal of Plankton Research*, *34*(9), 749-760, doi:10.1093/plankt/fbs010.

Kahru, M., M. G. Jacox, and M. D. Ohman (2018), GCE1: Decrease in the frequency of oceanic fronts and surface chlorophyll concentration in the California Current System during the 2014-2016 northeast Pacific warm anoamlies, *Deep-Sea Research I*, *140*, 4-13, doi:10.1016/j.dsr.2018.04.007.

Kostianoy, A. G., and J. R. E. Lutjeharms (1999), Atmospheric effects in the Angola-Benguela frontal zone, *Journal of Geophysical Research: Oceans*, *104*(C9), 20963-20970, doi:10.1029/1999jc900017.

Kurian, J., F. Colas, X. Capet, J. C. McWilliams, and D. B. Chelton (2011), Eddy properties in the California Current System, *Journal of Geophysical Research*, *116*, C08027, doi:10.1029/2010jc006895.

Lehahn, Y., F. d'Ovidio, M. Lévy, Y. Amitai, and E. Heifet (2011), Long range transport of a quasi isolated chlorophyll patch by an Agulhas ring, *Geophysical Research Letters*, *38*, L16610, doi:10.1029/2011GL048588.

Letelier, J., O. Pizarro, and S. Nuñez (2009), Seasonal variability of coastal upwelling and the upwelling front off central Chile, *Journal of Geophysical Research: Oceans*, *114*(C12), doi:10.1029/2008JC005171.

Liang, J. H., J. C. McWilliams, and N. Gruber (2009), High-frequency response of the ocean to mountain gap winds in the northeastern tropical Pacific, *Journal of Geophysical Research: Oceans*, *114*(C12), doi:10.1029/2009JC005370.

Lovecchio, E., N. Gruber, and M. Münnich (2018), Mesoscale contribution to the long-range offshore transport of organic carbon from the Canary Upwelling System to the open North Atlantic, *Biogeosciences*, *15*, 5061-5091, doi:10.5194/bg-15-5061-2018.

Lynn, R. J., and J. J. Simpson (1987), The California Current System: The Seasonal Variability of its Physical Characteristics, *Journal of Geophysical Research*, *92*(C12), 12947-12966, doi:10.1029/JC092iC12p12947.

Macias, D., M. Landry, R., A. Gershunov, A. J. Miller, and P. J. S. Franks (2012), Climatic control of upwelling variability along the western North-American coast, *PloS one*, *7*(1), e30436, doi:10.1371/journal.pone.0030436.

Marchesiello, P., J. C. McWilliams, and A. Shchepetkin (2003), Equilibrium structure and dynamics of the California Current System, Journal of Physical Oceanography, 33, 753-783, doi:10.1175/1520-0485(2003)33<753:esadot>2.0.co;2.

Mauzole, Y., H. Torres, and L. L. Fu (2020), Patterns and Dynamics of SST Fronts in the California Current System, *Journal of Geophysical Research: Oceans*, *125*(2), e2019JC015499, doi:10.1029/2019JC015499.

Meunier, T., E. D. Barton, B. Barreiro, and R. Torres (2012), Upwelling filaments off Cap Blanc: Interaction of the NW African upwelling current and the Cape Verde frontal zone eddy field?, *Journal of Geophysical Research: Oceans*, *117*(C8), doi:10.1029/2012JC007905.

Meyers, S. D., A. Melsom, G. T. Mitchum, and J. J. O'Brien (1998), Detection of the fast Kelvin wave teleconnection due to El Niño-Southern Oscillation, *Journal of Geophysical Research: Oceans*, *103*(C12), 27655-27663, doi:10.1029/98jc02402.

Nagai, T., N. Gruber, H. Frenzel, Z. Lachkar, J. C. McWilliams, and G.-K. Plattner (2015), Dominant role of eddies and filaments in the offshore transport of carbon and nutrients in the California Current System, *Journal of Geophysical Research: Oceans*, *120*, 5318-5341, doi:10.1002/2015jc010889.

Nieto, K., H. Demarcq, and S. McClatchie (2012), Mesoscale frontal structures in the Canary Upwelling System: New front and filament detection algorithms applied to spatial and temporal patterns, *Remote Sensing of Environment*, *123*, 339-346, doi:10.1016/j.rse.2012.03.028.

Oerder, V., J. P. Bento, C. E. Morales, S. Hormazabal, and O. Pizarro (2018), Coastal upwelling front detection off central Chile (36.5–37 S) and spatio-temporal variability of frontal characteristics, *Remote sensing*, *10*(5), 690, doi:10.3390/rs10050690.

Pegliasco, C., A. Chaigneau, and R. Morrow (2015), Main eddy vertical structures observed in the four major Eastern Boundary Upwelling Systems, *Journal of Geophysical Research: Oceans*, *120*, 6008-6033, doi:10.1002/2015jc010950.

Ramp, S. R., P. F. Jessen, K. H. Brink, P. P. Niiler, F. L. Daggett, and J. S. Best (1991), The physical structure of cold filaments near Point Arena, California, during June 1987, *Journal of Geophysical Research: Oceans*, *96*(C8), 14859-14883, doi:10.1029/91JC01141.

Relvas, P., and E. D. Barton (2002), Mesoscale patterns in the Cape Sao Vicente (Iberian peninsula) upwelling region, *Journal of Geophysical Research: Oceans*, *107*(C10), 28-21-28-23, doi:10.1029/2000JC000456.

Santos, F., M. Gomez-Gesteira, M. DeCastro, and I. Alvarez (2012), Differences in coastal and oceanic SST trends due to the strengthening of coastal upwelling along the Benguela current system, *Continental Shelf Research*, *34*, 79-86, doi:10.1016/j.csr.2011.12.004.

Schwing, F. B., T. Murphree, L. deWitt, and P. M. Green (2002), The evolution of oceanic and atmospheric anomalies in the northeast Pacific during the El Niño and La Niña events of 1995-2001, *Progress in Oceanography*, *54*, 459-491, doi:10.1016/S0079-6611(02)00064-2.

Stramma, L., T. Fischer, D. S. Grundle, G. Krahmann, H. W. Bange, and C. A. Marandino (2016), Observed El Niño conditions in the eastern tropical Pacific in October 2015, *Ocean Science*, *12*, 861-873, doi:10.5194/os-12-861-2016.

Strub, P. T., V. Combes, F. A. Shillington, and O. Pizarro (2013), Currents and Processes along the Eastern Boundaries, in *Ocean Circulation and Climate: A 21st Century Perspective*, edited by G. Siedler, S. M. Griffies, J. Gould and J. A. Church, pp. 339-384, Academic Press, doi:10.1016/b978-0-12-391851-2.00014-3.

Strub, P. T., and C. James (2000), Altimeter-derived variability of surface velocities in the California Current System: 2. Seasonal circulation and eddy statistics, *Deep-Sea Research II*, *47*, 831-870, doi:10.1016/S0967-0645(99)00129-0.

Strub, P. T., and C. James (2002), The 1997–1998 oceanic El Niño signal along the southeast and northeast Pacific boundaries—an altimetric view, *Progress in Oceanography*, *54*, 439-458, doi:10.1016/S0079-6611(02)00063-0.

Strub, P. T., P. M. Kosro, and A. Huyer (1991), The Nature of the Cold Filaments in the California Current System, *Journal of Geophysical Research*, *96*, 14,743-714,768.

Strub, P. T., J. M. Mesias, V. Montecino, J. Rutllant, and S. Salinas (1998), Coastal ocean circulation off western South America, in *The Sea*, edited by A. R. Robinson and K. H. Brink, pp. 273-313, John Wiley & Sons.

Ulloa, O., R. Escribano, S. Hormazabal, R. A. Quiñones, R. R. González, and M. Ramos (2001), Evolution and biological effects of the 1997-98 El Niño in the upwelling ecosystem off northern Chile, *Geophysical Research Letters*, *28*(8), 1591-1594, doi:10.1029/2000gl011548.

Vazquez-Cuervo, J., B. Dewitte, T. M. Chin, E. M. Armstrong, S. Purca, and E. Alburqueque (2013), An analysis of SST gradients off the Peruvian Coast: The impact of going to higher resolution, *Remote Sensing of Environment*, *131*, 76-84, doi:10.1016/j.rse.2012.12.010.

Veitch, J. A., and P. Penven (2017), The role of the Agulhas in the Benguela Current system: A numerical modeling approach, *Journal of Geophysical Research: Oceans*, *122*(4), 3375-3393, doi:10.1002/2016JC012247.

Walsh, J. J. (1977), A biological sketchbook for an eastern boundary current, in *The Sea*, edited by E. D. Goldbert, I. N. McCave, J. J. O'Brien and J. H. Steele, pp. 923-968, Wiley-Interscience, Hoboken, N. J.

Wang, Y., R. M. Castelao, and Y. Yuan (2015), Seasonal variability of alongshore winds and sea surface temperature fronts in Eastern Boundary Current Systems, *Journal of Geophysical Research: Oceans*, *120*, 2385-2400, doi:10.1002/2014jc010379.

Wang, Y., J. Liu, H. Liu, P. Lin, Y. Yuan, and F. Chai (2021), Seasonal and interannual variability in the sea surface temperature front in the eastern Pacific Ocean, *Journal of Geophysical Research: Oceans*, e2020JC016356, doi:10.1029/2020JC016356.

Woodson, C. B., and S. Y. Litvin (2015), Ocean fronts drive marine fishery production and biogeochemical cycling, *Proceedings of the National Academy of Sciences of the United States of America*, *112*(6), 1710-1715, doi:10.1073/pnas.1417143112.

Yuan, Y., and R. M. Castelao (2017), Eddy-induced sea surface temperature gradients in Eastern Boundary Current Systems, *Journal of Geophysical Research: Oceans*, *122*, 4791-4801, doi:10.1002/2017JC012735.

CHAPTER 2

OFFSHORE TRANSPORT OF PARTICULATE ORGANIC CARBON IN THE CALIFORNIA CURRENT SYSTEM BY MESOSCALE EDDIES [1]

[1] Amos, C.M., R.M. Castelao, and P.M. Medeiros. 2019. *Nature Communications*, 10, 4940. Reprinted here with permission of the publisher.

2.1. Abstract

The California Current System is characterized by upwelling and rich mesoscale eddy activity. Cyclonic eddies generally pinch off from meanders in the California Current, potentially trapping upwelled water along the coast and transporting it offshore. Here, we use satellite-derived measurements of particulate organic carbon (POC) as a tracer of coastal water to show that cyclones located offshore that were generated near the coast contain higher carbon concentrations in their interior than cyclones of the same amplitude generated offshore. This indicates that eddies are in fact trapping and transporting coastal water offshore, resulting in an offshore POC enrichment of 20.9 ± 11 Gg year^{-1}. This POC enrichment due to the coastally-generated eddies extends for 1000 km from shore. This analysis provides large-scale observational-based evidence that eddies play a quantitatively important role in the offshore transport of coastal water, substantially widening the area influenced by highly productive upwelled waters in the California Current System.

2.2. Introduction

Mesoscale eddies with radius on the order of 100 km are ubiquitous features (Chelton et al., 2011b) known to influence the horizontal and vertical distribution of physical and biogeochemical properties throughout the global ocean (Strub et al., 1991; Chaigneau et al., 2011; Chelton et al., 2011a; Gaube et al., 2013; Chenillat et al., 2015; Amores et al., 2017). The majority of these eddies are nonlinear (ratio of rotational speed to translational speed greater than 1), meaning they can theoretically trap water parcels and associated properties during formation (Chelton et al., 2011b). Eddies can then potentially transport the trapped properties for hundreds of kilometers throughout the ocean (Early et al., 2011; Lehahn et al., 2011).

In the California Current System (CCS), a highly productive Eastern Boundary Current System (EBCS; Huyer, 1983), eddies are commonly observed (Strub and James, 2000; Chelton et al., 2011b; Pegliasco et al., 2015) and are thought to play a role in redistributing nutrients into the oligotrophic, offshore region (Gruber et al., 2011; Kurian et al., 2011; Nagai et al., 2015). Persistent equatorward winds during the summer produce offshore surface Ekman transport and upwelling along the coast, bringing cold, nutrient-rich waters to the surface. This results in a band of elevated nutrients and particulate organic carbon (POC) concentrations near the coast (Huyer, 1983; Lynn and Simpson, 1987; Bakun and Nelson, 1991; Chavez and Messié, 2009; García-Reyes and Largier, 2012). As the California Current flows southward along the coast, meanders in the current produce filaments that can pinch off as cyclonic (counterclockwise in the Northern Hemisphere) and anticyclonic (clockwise) eddies which then propagate westward (Strub et al., 1991; Strub and James, 2000; Kurian et al., 2011; Nagai et al.,

2015). During formation of the eddies, the nutrients and properties associated with the upwelled coastal water could be potentially trapped in their interior (Gaube et al., 2014). Modeling studies suggest that eddies can transport the trapped coastal water offshore, contributing to the redistribution of carbon, nutrients, and other properties in the CCS (Liang et al., 2009; Combes et al., 2013; Nagai et al., 2015; Chenillat et al., 2016) and in other upwelling systems (Lovecchio et al., 2018). While previous observational studies have shown individual examples of eddies transporting materials in various regions of the ocean (Crawford et al., 2007; Lehahn et al., 2011; Gaube et al., 2014; Gaube and McGillicuddy Jr., 2017), no large-scale observational study has systematically quantified eddy-induced transport and its influence on carbon distribution in highly productive upwelling systems. The offshore transport of coastal water that is rich in carbon and nutrients in the CCS could have important implications for the marine ecosystem. Therefore, quantifying the eddy-induced transport using observations is important for further understanding the influence of eddies in EBCS. Using satellite-derived measurements of POC as a tracer of coastal water, we show that cyclonic eddies located offshore that were generated near the coast contain higher carbon concentrations in their interior than cyclonic eddies of the same amplitude generated locally offshore, contributing to the enrichment of POC in the offshore region.

2.3. Results

2.3.1. Effects of eddies on particulate organic carbon distribution

Developments in eddy detection and tracking algorithms using altimetry data have made it possible to study mesoscale eddies and their properties over large spatial areas

and long-time periods (Stegmann and Schwing, 2007; Chaigneau et al., 2009; Chelton et al., 2011b). Here, we use thirteen years of satellite-derived measurements of POC (Stramski et al., 2008) as a tracer of coastal water to show that eddies can play an important role in redistributing carbon from the coastal region to offshore areas in the CCS (Figure 2.1). Meanders and filaments (Haidvogel et al., 1991) extending westward from the California Current are often distinguished by elevated POC concentrations as they initiate the offshore transport of coastal water (Figure 2.1a). A filament can pinch off to the west of the current as a cyclonic eddy (Figure 2.1b-c), entraining upwelled coastal water that is rich in carbon and nutrients from the shoreward side of the current. The trapped coastal water then gets transported offshore for hundreds of kilometers, as indicated by the elevated POC concentrations remaining months later in the interior of the eddy compared to the surrounding offshore waters (Figure 2.1d).

The fraction of surface POC in the CCS that is found in the interior of eddies is calculated from the thirteen years of satellite-derived POC using the locations and sizes of eddies identified in this region from an existing global eddy dataset (Chelton et al., 2011b). In the region 300-1200 km from the coast between 33° and 43° N, which is outside of the 300 km nearshore band where POC concentrations are the highest, about 6.9% of the total amount of POC can be found inside cyclonic eddies that are generated in this region, and these eddies occupy about 7% of the total area (Figure 2.2a). In contrast, 13.4% of the total amount of POC is found inside cyclones generated inshore of 300 km and propagated to the offshore region, but these eddies only occupy 10.4% of the total offshore area during September-February (Figure 2.2c). The relative enrichment of POC content in the interior of cyclones that were generated near the coast and propagated

offshore compared to the area occupied by those eddies in the offshore region is largest from late summer to early winter (Figure 2.2c). This is consistent with eddies being generated near the coast during late spring/early summer (May-August) and propagating offshore at ~2 km day^{-1} (Strub and James, 2000; Stegmann and Schwing, 2007; Chaigneau et al., 2009; Kurian et al., 2011), reaching the offshore region 3-6 months later.

Although anticyclonic eddies are also capable of trapping and transporting materials, they have less of an impact on the redistribution of recently upwelled, carbon- and nutrient-rich water in the CCS compared to cyclones due to differences in the water that is entrained during formation. Anticyclonic eddies are often generated from meanders that pinch off from the shoreward side of the California Current (Gaube et al., 2014; Nagai et al., 2015), trapping oligotrophic offshore water that contains lower concentrations of POC and nutrients than the water closer to the coast that is trapped by cyclones (as shown in Figure 2.1). Because of this, anticyclones formed inshore of 300 km from the coast that propagated offshore contained lower percentages of the total POC in the offshore region compared to cyclones (Figure 2.2b,d), further indicating that anticyclones are trapping water with less POC, nutrients, and other properties associated with the upwelled coastal water when they form. Anticyclonic eddies therefore do not contribute substantially to the offshore transport of coastal water like their cyclonic counterparts.

2.3.2. Lateral transport of coastal tracers by cyclonic eddies

To detect eddies transporting trapped coastal water via satellite observations, the anomalous POC signature associated with each eddy was isolated and compared between cyclones generated inshore and offshore of 300 km from the coast (see Methods and Figures A.1 and A.2). Cyclonic eddies in the CCS are associated with positive POC anomalies (Figure 2.3a-c). The concentration of POC in the eddies' interior is generally highest for cyclones generated and located inshore of 300 km from the coast (Figure 2.3a,d). Except for eddies of small amplitude (3-5 cm), cyclones that are generated inshore and propagate offshore of 300 km from the coast have higher POC anomalies than cyclones of the same amplitude generated offshore between 300-600 km (Figure 2.3b-d). The POC enrichment in the cyclones generated inshore and located offshore in comparison to those generated offshore could be due to the offshore transport of the POC that was trapped during eddy formation near the coast, to remineralization of the trapped POC and recycling into new carbon, and to local production as the eddy propagates offshore through the utilization of nutrients that were trapped at formation. All of these sources of POC are influenced by the trapping of POC- and nutrient-rich coastal upwelled water by eddies during formation and subsequent offshore lateral transport. On average it takes cyclonic eddies about 4-6 months to reach 300-600 km offshore. Extending the analyses farther offshore in additional 300 km width bands reveals that the POC signature associated with cyclonic eddies generated inshore that propagated offshore remains higher than the signature for cyclones generated in the offshore region in the 600-900 km and the 900-1200 km bands from the coast (Figure 2.4). No significant difference in POC content is observed offshore of 1200 km from the coast, indicating that

POC enrichment in offshore waters due to the influence of coastally-generated eddies is most important within about 1000 km from shore. For both cyclonic eddies generated inshore or offshore of 300 km from the coast, the mean POC anomaly decreases as the eddies propagate westward (Figure 2.4).

For cyclonic eddies formed and located inshore of 300 km from the coast, the monthly mean POC anomaly is highest during May to July (Figure 2.5a), following a seasonal pattern that is consistent with the seasonality of eddy generation (Stegmann and Schwing, 2007; Chaigneau et al., 2009; Kurian et al., 2011) and upwelling (Bakun and Nelson, 1991; García-Reyes and Largier, 2012) along the coast in the CCS. About 55% of cyclonic eddies formed inshore of 300 km from the coast propagate to the 300-600 km offshore region (Table A.1). The mean POC anomaly associated with these eddies peaks between November-January (Figure 2.5b), about 4-6 months after the peak in the POC anomaly associated with the eddies is observed when they were located less than 300 km offshore (Figure 2.5a). The distance that the eddies that are generated inshore travel to the offshore region and the delay in the timing of the peak POC anomaly between when the eddies are located inshore and offshore of 300 km indicate propagation speeds of ~2 km day^{-1}, which is consistent with the known eddy propagation speeds in the CCS (Stegmann and Schwing, 2007; Chaigneau et al., 2009; Kurian et al., 2011). This consistency in eddy propagation speed and the time difference in the peak in POC anomaly between cyclones located inshore and offshore provides further evidence that cyclones are indeed transporting coastal water offshore. Cyclonic eddies generated offshore between 300-600 km show no clear seasonal trend in the POC anomalies, except for a small decrease during summer (Figure 2.5c).

The mean volume transport by cyclones can be calculated by using the average volume associated with the cyclonic eddy occurrences of different amplitudes that are generated near the coast and then propagate offshore. We focus on cyclones because of their larger influence on the offshore transport of coastal water that is influenced by upwelling (Figure 2.2a,c) compared to anticyclones (Figure 2.2b,d). In the CCS, on average 6.0 ± 0.6 cyclonic eddies with lifetimes longer than 4 weeks are generated inshore of 300 km from the coast and propagate offshore of 300 km annually between 33° and 43°N (Figure 2.6a; Chelton et al., 2011b). Considering an average trapping depth inside cyclones of 400 m that was estimated from our modeling results using large cyclonic eddies that are comparable to the satellite-detected eddies and is consistent with previous studies (Kurian et al., 2011), our analyses indicate that 65 ± 7% of the volume of water initially trapped inside cyclones remains trapped after the eddies propagate offshore (see Methods and Figure A.3). Using this trapping efficiency, the resulting annual volume transport in the top 400 m by cyclonic eddies in the CCS is 1.06 ± 0.2 Sv (1 Sv = 10^6 m^3 s^{-1}; Figure 2.6b; see Equation 2 in methods). To provide error bounds for this estimate, using the ±7% error in the trapping efficiency results in volume transports of 0.95 and 1.2 Sv. This range of values for the volume transport is comparable to the estimated annual mean integrated transport due to eddies in the Canary Current System (1.3 Sv in the top 300 m; Sangrà et al., 2009). The relationship between in situ POC at the surface and integrated from the surface to 100 m depth (see Methods and Figure A.4; Allison et al., 2010) can also be used to estimate the amount of POC that is added to the offshore region by cyclonic eddies generated near the coast that are trapping the upwelled coastal water and transporting it offshore (Figure A.5). For that, the differences in the

POC content between cyclonic eddies located 300-600 km offshore that were formed inshore of 300 km and those formed offshore between 300-600 km from the coast are used (Equation 1; see also Figure A.5 and Figure 2.3b-c). Lateral transport by cyclonic eddies results in a POC enrichment offshore of 20.9 ± 11 Gg year^{-1} in the top 100 m (Figure 2.6c). As mentioned before, this POC enrichment may be associated with the direct lateral transport of POC from the coastal region that was trapped in the interior of cyclonic eddies during formation, but it could also be related to the offshore transport of nutrient-rich water that is also trapped inside the eddies which supports production or to the trapped POC being locally remineralized and recycled into new carbon. All of these sources of POC are resultant of coastal water being trapped by cyclonic eddies and transported offshore. We note that changes in the mixed layer depth (Gaube et al., 2018) or the euphotic zone depth may result in different amounts of POC being trapped inside the eddies. If the calculations are repeated for shallower layers of 20 m or 50 m, the enhancement of POC in the offshore region is estimated at 5.4 ± 2.9 Gg year^{-1} and 12.2 ± 6.1 Gg year^{-1}, respectively. We note that the correlation coefficient between surface POC and integrated POC for different depth ranges is approximately depth independent in the top 100 m.

2.4. Discussion

Previous observational studies have shown examples of mesoscale eddies transporting properties in different regions of the ocean (Crawford et al., 2007; Lehahn et al., 2011; Gaube and McGillicuddy Jr., 2017). Modeling studies have also suggested that eddies can trap and transport materials offshore in the CCS (Combes et al., 2013; Nagai

et al., 2015) and in other EBCS (Lovecchio et al., 2018), resulting in reduced biological production in the nearshore environment (Gruber et al., 2011). In this study, we present the first observational evidence that this process is important enough to produce a systematic signature in eddies far from the coast in the CCS. Our results indicate that cyclonic eddies formed near the coast are capable of trapping carbon- and nutrient-rich coastal water and transporting it offshore for hundreds of kilometers. Cross-shelf transport in the CCS is important for increasing the area influenced by highly productive upwelled waters. Studies have shown that the offshore deflection of the surface-intensified upwelling jet and its associated meanders and filaments extends about 400 km offshore on average (Lynn and Simpson, 1987; Strub and James, 2000; Barth et al., 2005), inducing cross-shelf transport of 1-2 Sv (Mooers and Robinson, 1984; Kosro and Huyer, 1986; Barth et al., 2000; Castelao and Barth, 2005). These filaments can transport organic carbon offshore in a very intense but coastally confined manner, dominating the mesoscale offshore transport in EBCS within 500 km from shore and contributing to up to 80% of the total flux of organic carbon at 100 km offshore (Lovecchio et al., 2018). Our novel observational-based study reveals that the signature of the enhanced POC in the interior of cyclonic eddies generated near the coast is detectable until about 1000 kilometers from shore, indicating the role of eddies in redistributing POC and coastal water across a wider area. We estimate that cyclonic eddies transport ~1 Sv offshore, indicating that this mechanism can be just as important as the offshore deflection of the upwelling jet (Barth et al., 2000). Furthermore, the enrichment of POC in the offshore region induced by cyclonic eddies generated near the coast is estimated to be about 20.9 ± 11 Gg year^{-1}, with about 70% occurring between late summer and early winter.

The annual POC enrichment offshore due to cyclonic eddies can be as high as 30-35% of the total amount of POC introduced into the CCS by the Columbia River (U.S.A.) annually (Dahm et al., 1981; Sullivan et al., 2001; Small and Prahl, 2004). Total carbon redistributed by cyclonic eddies is likely to be significantly larger since our estimate only includes the particulate phase and dissolved organic carbon concentrations can be 10-25 times larger than POC content in near-surface waters in the CCS (Druffel et al., 1996; Bauer et al., 1998). In addition to carbon and nutrients, the trapped coastal water contains other materials that are also presumably being redistributed to the offshore region by cyclonic eddies.

The estimates of volume transport and POC enrichment are influenced by the limitations associated with detecting the eddies using satellite observations. Imperfections in the eddy detection and tracking algorithms may result in distortions in the identified eddies, especially when eddies are interacting with other eddies or other mesoscale features (Amores et al., 2018). Uncertainties in eddy characteristics, such as radius and amplitude, could affect the transport calculations. Additionally, only eddies with radii larger than 40-50 km are detectable with altimetry data (Chelton et al., 2011b). The processing of the satellite-derived POC observations, specifically the use of a Gaussian fit to isolate the eddy signature, also results in smoothed fields removing small-scale variability. Since submesoscale eddies are also abundant in the CCS and may further contribute to offshore transport and subduction of materials (Capet et al., 2008; McWilliams, 2016; Dauhajre et al., 2017), it will be important for future studies to further understand the role of these smaller eddies and to quantify their relative importance on offshore transport in the CCS.

The CCS is one of four major EBCS, all of which share similarities in eddy activity (Chaigneau et al., 2009; Pegliasco et al., 2015; Yuan and Castelao, 2017). The eddy-driven offshore transport of coastal water will presumably be important in the other EBCS as well. Eddy activity, mesoscale variability, and upwelling in EBCS are linked to winds (Strub and James, 2000), which are likely to change in the future (Bakun, 1990; Snyder et al., 2003; Sydeman et al., 2014; Xiu et al., 2018). Therefore, changes in the seasonality of mesoscale activity and eddy generation are also possible. Our analyses suggest that changes in eddy activity would likely result in changes in offshore transport of coastal water that is rich in carbon and nutrients and this could have important implications for the marine ecosystem in highly-productive EBCS.

2.5. Methods

2.5.1. Mesoscale Eddies

The location and characteristics of mesoscale eddies in the CCS used in this study were obtained from the 4th release of an existing global dataset of mesoscale eddies (Chelton et al., 2011b; wombat.coas.oregonstate.edu/eddies/index.html). To detect mesoscale eddies, daily sea level anomaly (SLA) fields produced by Archiving, Validation, and Interpretation of Satellite Oceanographic data (AVISO) are first spatially-filtered to remove large scale variability. Mesoscale eddies in the 4th release of the dataset are detected using a method that grows eddies from individual SLA extrema (Schlax and Chelton, 2016). The growing method starts with individual SLA extrema (positive for anticyclones and negative for cyclones) and finds all neighboring pixels whose SLA values lie above a sequence of thresholds. An eddy is defined when the set of connected

pixels satisfies a set of criteria used to define compact and coherent structures. Eddies are then tracked by pairing eddy realizations that are within allowable ranges of amplitude, radius and distance of the initial eddy at subsequent time steps. The eddy detection and tracking algorithms are described in detail in Chelton et al. (2011b) and Schlax and Chelton (2016). Given the resolution of the AVISO satellite fields, only mesoscale eddies with radius larger than ~ 40-50 km are resolved, therefore submesoscale and smaller mesoscale variability are not included in the dataset and in the analyses. Also, complications can arise when eddies merge or interact with other eddies or from noisiness in the SLA fields. This can result in imperfections in the detection of the boundaries and characteristics (e.g., radius, amplitude) of the eddies (Chelton et al., 2011b; Amores et al., 2018). Despite these limitations, animations of the eddy tracks on SLA fields indicated that the dataset captures most large mesoscale eddies in the CCS.

Nonlinear eddies located in the CCS between 33°-43°N and 0-1500 km from the coast during the time period of the satellite POC data (1997-2010) were identified from the dataset for the analyses. Eddies are considered nonlinear if the ratio $U/c > 1$, where U is the maximum rotational speed and c is the translation speed of the eddy estimated at each point along the trajectory (Chelton et al., 2011b). In total, 553 cyclonic eddy tracks were studied. Calculations of the nonlinearity parameters indicated that the majority of the eddies were nonlinear for at least 80% of their lifetime. The distance between the coastline and the location of the eddy centers at each point along the eddy trajectories was calculated to distinguish eddies generated or located inshore and offshore of 300 km from the coast (Figure A.1). The threshold of 300 km from the coast was chosen to define inshore and offshore based on the average width of the band of high POC concentrations

along the coast. The band of high POC extends about 250 km from the coast on average. Since POC is used here as a tracer of coastal water, a distance larger than the average width of the band with high POC was chosen to distinguish between upwelled coastal water and offshore water. The distance of 300 km is also consistent with the average width of the coastal band with high sea surface temperature frontal activity and of the meandering upwelling jet (Wang et al., 2015). To check that the results are not sensitive to the distance threshold, the analyses were repeated using other distances from the coast, e.g., 350 km, and the results were consistent to those presented here. The offshore region was divided into bands of 300 km in width for the analyses (300-600 km, 600-900 km, 900-1200 km, and 1200-1500 km from the coast). The width of the offshore bands was chosen to be the same as the inshore region (0-300 km).

2.5.2. Particulate Organic Carbon Measurements

Daily remote sensing reflectance (Rrs) data from Sea-Viewing Wide Field-of-View Sensor (SeaWiFS; oceandata.sci.gsfc.nasa.gov/SeaWiFS/) were used to estimate POC concentrations (Stramski et al., 2008). Data are available daily from September 1997 to December 2010 at 9 km resolution. To reduce the influence of cloud coverage, data were averaged at a 7-day interval (Figure A.2a). The mesoscale structures that are of primary interest here are obscured by the large-scale POC background distribution. Spatial high-pass filtering (Chelton et al., 2004; Schlax and Chelton, 2016) the weekly POC fields (6° longitude by 6° latitude window) to remove the large-scale patterns allowed for isolating the POC anomaly associated with mesoscale activity in the region (Gaube et al., 2013; Gaube et al., 2014; Gaube and McGillicuddy Jr., 2017; Figure A.2b).

Quantitatively similar results are obtained if the large-scale patterns in the region were removed by computing the long-term weekly-averaged POC distribution, instead of using a spatial filter. Cyclonic eddies, which were identified using altimetry data (Chelton et al., 2011b; black box in Figure A.2b), were generally characterized by positive POC anomalies, while anticyclones were generally associated with negative POC anomalies.

To further isolate the signature associated with each eddy (Yuan and Castelao, 2017) from other mesoscale features, we extracted the POC anomaly within 2 by 2 eddy radii from the eddy center (Figure A.2c). To facilitate comparisons among eddies of various radii, the distance from the eddy center was normalized by the eddy radius on each 2 by 2 radii grid (Gaube et al., 2014; Figure A.2c). Only eddies with at least 90% cloud-free pixel coverage for POC data within one eddy radius and 75% pixel coverage within two eddy radii (black box in Figure A.2b) were used. To remove noisy, small-scale variability not related to the eddy, a 2-D Gaussian function was fitted to the resulting POC anomaly field (Yuan and Castelao, 2017). The fit is consistent with the average eddy shape which is well represented as Gaussian (Chelton et al., 2011b). Lastly, the center of the Gaussian fitted POC anomaly was shifted to align with the center of the eddy (Figure A.2d). Repeating the analyses without using the Gaussian fit produced results that are qualitatively similar to those presented here (e.g., cyclonic eddies generated near the coast that propagated offshore are enriched in POC compared to those generated locally offshore). However, visual inspection of the POC anomaly fields indicated that large anomalies associated with other mesoscale features (e.g., upwelling front, filaments) are often observed around individual eddies, especially around the edges of the 2 by 2 eddy radii boxes, which influence the composites of the POC anomalies for

each eddy amplitude bin (Figure 2.3). Using the Gaussian fit allowed for the eddy signature to be isolated from the signature of these other mesoscale features.

In situ POC concentrations were measured in the CCS since 2006 as part of the CCS Long Term Ecological Research monitoring efforts (Aluwihare, 2018). Data availability is larger at the surface, decreasing significantly below 100 m depth. A depth range of 100 m for estimating organic carbon fluxes has been used in previous modeling studies (Lovecchio et al., 2018). In situ POC integrated from the surface to 100 m depth is correlated with surface concentrations ($r = 0.73$, $p < 0.01$; Figure A.4), which allowed for the integrated POC content in the top 100 m to be estimated from satellite data following Allison et al. (2010). Eddy-induced anomalies in the integrated POC content in the top 100 m (Figure A.5) were extracted from each eddy following the procedure described above (Figure A.2). Those anomalies were then used to calculate the offshore enrichment of POC (Gg year^{-1}) in the top 100 m by eddies (Figure 2.6) as

$$POC\ enrichment\ (\text{Gg year}^{-1}) = \Delta(POC_{100}) \times eddy\ area \times N \qquad \text{(Eq. 1)}$$

where $\Delta(POC_{100})$ is the difference between the integrated POC content inside cyclones located offshore that were generated near the coast and those generated offshore for each amplitude bin (Figure A.5) and N is the number of eddies per year for each amplitude bin that are generated inshore of 300 km from coast and propagate offshore. The POC enrichment was then summed for the multiple amplitude bins.

2.5.3. Ocean Model

We use a previous regional implementation of the Regional Ocean Modeling System (ROMS; Haidvogel et al., 2008) to the CCS (Castelao and Luo, 2018). The model resolution is 4 km in the horizontal with 30 vertical terrain-following layers. Initial and boundary conditions for the regional model are obtained from a ROMS implementation to the entire North Pacific Ocean. The regional model is forced by surface wind stress from the SeaWinds scatterometer onboard NASA's Quick Scatterometer (QuikSCAT) satellite, and by heat and freshwater fluxes from NCEP North American Regional Reanalysis (NARR). Additional details of the model implementation are presented in Castelao and Luo (2018). A passive tracer with unit concentration that does not sink was released uniformly throughout the entire water column inside 4 cyclonic eddies in different seasons (see Figure A.3 for one example). These eddies in the model were generated near the coast and propagated offshore and they had radii ranging from 55 to 85 km, which is consistent with characteristics of the satellite-detected eddies. The percentage of the tracer remaining inside each eddy in the top 400 m was then calculated as the eddy propagated offshore, which provided a measure of the fraction of the water effectively trapped by the eddy. The analysis revealed that 65 ± 7% of the water initially present in the interior of eddies generated near the coast remained trapped when those eddies reached over 300 km from the coast. This trapping efficiency was used to estimate the volume of water transported offshore by eddies in the CCS in the top 400 m as

$$\textit{Volume transport}\ (\mathrm{Sv}) = (\textit{eddy area} \times \textit{trapping depth} \times N \times \textit{trapping efficiency}) \,/\, T \quad \text{(Eq. 2)}$$

where T is the number of seconds in 1 year. The volume transport was then summed for the multiple amplitude bins. Trapping efficiencies of 58% and 72% were also assumed to provide error bounds in the volume transport estimate. We note that the computation of POC enrichment in offshore regions (Eq. 1) is not dependent on this model estimate of the trapping efficiency.

Data availability

The data/reanalysis that support the findings of this study are publicly available online at http://wombat.coas.oregonstate.edu/eddies/index.html, https://oceandata.sci.gsfc.nasa.gov/SeaWiFS/, and https://doi.org/10.6073/pasta/20c05dd205be2225ecb32a5fede1c36c.

Code availability

Model codes are available at www.myroms.org.

2.6. Acknowledgements

We gratefully acknowledge support by NASA's Ocean Vector Winds Science Team (NNX14AM70G), Ocean Surface Topography Science Team (NNX13AD80G), Physical Oceanography (80NSSC18K0766) and Earth and Space Science Fellowship (80NSSC18K1342) programs, and by NSF (OPP-1643468).

References

Allison, D. B., D. Stramski, and B. G. Mitchell (2010), Seasonal and interannual variability of particulate organic carbon within the Southern Ocean from satellite ocean color observations, *Journal of Geophysical Research*, *115*, C06002, doi:10.1029/2009jc005347.

Aluwihare, L. (2018), Particulate organic carbon and nitrogen measurements at selected depths in the water column in the CCS region since 2006 - 2016 (ongoing), edited by E. D. Initiative, doi:10.6073/pasta/20c05dd205be2225ecb32a5fede1c36c.

Amores, A., G. Jordà, T. Arsouze, and J. Le Sommer (2018), Up to what extent can we characterize ocean eddies using present-day gridded altimetric products?, *Journal of Geophysical Research: Oceans*, *123*, 7220-7236, doi:10.1029/2018JC014140.

Amores, A., O. Melnichenko, and N. Maximenko (2017), Coherent mesoscale eddies in the North Atlantic subtropical gyre: 3-D structure and transport with application to the salinity maximum, *Journal of Geophysical Research: Oceans*, *122*, 23-41, doi:10.1002/2016JC012256.

Bakun, A. (1990), Global climate change and intensitifcation of coastal ocean upwelling, *Science*, *247*(4939), 198-201, doi:10.1126/science.247.4939.198.

Bakun, A., and C. S. Nelson (1991), The Seasonal Cycle of Wind-Stress Curl in Subtropical Eastern Boundary Current Regions, *Journal of Physical Oceanography*, *21*(12), 1815-1834, doi:10.1175/1520-0485(1991)021<1815:TSCOWS>2.0.CO;2.

Barth, J. A., S. D. Pierce, and T. J. Cowles (2005), Mesoscale structure and its seasonal evolution in the northern California Current System, *Deep-Sea Research II*, *52*(1-2), 5-28, doi:10.1016/j.dsr2.2004.09.026.

Barth, J. A., S. D. Pierce, and R. L. Smith (2000), A separating coastal upwelling jet at Cape Blanco, Oregon and its connection to the California Current System, *Deep-Sea Research II*, *47*, 783-810, doi:10.1016/S0967-0645(99)00127-7.

Bauer, J. E., E. R. M. Druffel, P. M. Williams, D. M. Wolgast, and S. Griffin (1998), Temporal variability in dissolved organic carbon and radiocarbon in the eastern North Pacific Ocean, *Journal of Geophysical Research*, *103*(C2), 2867-2881.

Capet, X., J. C. McWilliams, M. J. Molemaker, and A. F. Shchepetkin (2008), Mesoscale to submesoscale transition in the California Current System. Part I: Flow structure, eddy flux, and observational tests, *Journal of Physical Oceanography*, *38*, 29-43, doi:10.1175/2007JPO3671.1.

Castelao, R. M., and J. A. Barth (2005), Coastal ocean response to summer upwelling favorable winds in a region of alongshore bottom topography variations off Oregon, *Journal of Geophysical Research*, *110*, C10S04, doi:10.1029/2004JC002409.

Castelao, R. M., and H. Luo (2018), Upwelling jet separation in the California Current System, *Scientific Reports*, *8*, 16004, doi:10.1038/s41598-018-34401-y.

Chaigneau, A., G. Eldin, and B. Dewitte (2009), Eddy activity in the four major upwelling systems from satellite altimetry (1992–2007), *Progress in Oceanography*, *83*, 117-123, doi:10.1016/j.pocean.2009.07.012.

Chaigneau, A., M. Le Texier, G. Eldin, C. Grados, and O. Pizarro (2011), Vertical structure of mesoscale eddies in the eastern South Pacific Ocean: A composite analysis from altimetry and Argo profiling floats, *Journal of Geophysical Research*, *116*, C11025, doi:10.1029/2011JC007134.

Chavez, F. P., and M. Messié (2009), A comparison of Eastern Boundary Upwelling Ecosystems, *Progress in Oceanography*, *83*, 80-96, doi:10.1016/j.pocean.2009.07.032.

Chelton, D. B., P. Gaube, M. G. Schlax, J. J. Early, and R. M. Samelson (2011a), The Influence of Nonlinear Mesoscale Eddies on Near-Surface Oceanic Chlorophyll, *Science*, *334*, 328-334, doi:10.1126/science.1208897.

Chelton, D. B., M. G. Schlax, M. H. Freilich, and R. F. Milliff (2004), Satellite measurements reveal persistent small-scale features in ocean winds, *Science*, *303*, 978, doi:10.1126/science.1091901.

Chelton, D. B., M. G. Schlax, and R. M. Samelson (2011b), Global observations of nonlinear mesoscale eddies, *Progress in Oceanography*, *91*, 167-216, doi:10.1016/j.pocean.2011.01.002.

Chenillat, F., P. J. S. Franks, and V. Combes (2016), Biogeochemical properties of eddies in the California Current System, *Geophysical Research Letters*, *43*, 5812-5820, doi:10.1002/2016gl068945.

Chenillat, F., P. J. S. Franks, P. Rivière, X. Capet, N. Grima, and B. Blanke (2015), Plankton dynamics in a cyclonic eddy in the Southern California Current System, *Journal of Geophysical Research: Oceans*, *120*, 5566-5588, doi:10.1002/2015JC010826.

Combes, V., F. Chenillat, E. Di Lorenzo, P. Rivière, M. D. Ohman, and S. J. Bograd (2013), Cross-shore transport variability in the California Current: Ekman upwelling vs. eddy dynamics, *Progress in Oceanography*, *109*, 78-89, doi:10.1016/j.pocean.2012.10.001.

Crawford, W. R., P. J. Brickley, and A. C. Thomas (2007), Mesoscale eddies dominate surface phytoplankton in northern Gulf of Alaska, *Progress in Oceanography*, *75*, 287-303, doi:10.1016/j.pocean.2007.08.016.

Dahm, C. N., S. V. Gregory, and P. K. Park (1981), Organic Carbon Transport in the Columbia River, *Estuarine, Coastal and Shelf Science*, *13*, 645-658.

Dauhajre, D. P., J. C. McWilliams, and Y. Uchiyama (2017), Submesoscale coherent structures on the continental shelf, *Journal of Physical Oceanography*, *47*, 2949-2976, doi:10.1175/JPO-D-16-0270.1.

Druffel, E. R. M., J. E. Bauer, P. M. Williams, S. Griffin, and D. Wolgast (1996), Seasonal variability of particulate organic radiocarbon in the northeast Pacific Ocean, *Journal of Geophysical Research*, *101*(C9), 20,542-520,552.

Early, J. J., R. M. Samelson, and D. B. Chelton (2011), The Evolution and Propagation of Quasigeostrophic Ocean Eddies, *American Meteorological Society*, *41*, 1535-1555, doi:10.1175/2011JPO4601.1.

García-Reyes, M., and J. L. Largier (2012), Seasonality of coastal upwelling off central and northern California: New insights, including temporal and spatial variability, *Journal of Geophysical Research: Oceans*, *117*, C03028, doi:10.1029/2011jc007629.

Gaube, P., D. B. Chelton, P. G. Strutton, and M. J. Behrenfeld (2013), Satellite observations of chlorophyll, phytoplankton biomass, and Ekman pumping in nonlinear mesoscale eddies, *Journal of Geophysical Research: Oceans*, *118*, 6349-6370, doi:10.1002/2013jc009027.

Gaube, P., and D. J. McGillicuddy Jr. (2017), The influence of Gulf Stream eddies and meanders on near-surface chlorophyll, *Deep-Sea Research I*, *122*, 1-16, doi:10.1016/j.dsr.2017.02.006.

Gaube, P., D. J. McGillicuddy Jr., D. B. Chelton, M. J. Behrenfeld, and P. G. Strutton (2014), Regional variations in the influence of mesoscale eddies on near-surface chlorophyll, *Journal of Geophysical Research: Oceans*, *119*, 8195-8220, doi:10.1002/ 2014JC010111.

Gaube, P., D. J. McGillicuddy Jr., and A. J. Moulin (2018), Mesoscale eddies modulate mixed layer depth globally, *Geophysical Research Letters*, *46*(3), 1505-1512, doi:10.1029/2018GL080006.

Gruber, N., Z. Lachkar, H. Frenzel, P. Marchesiello, M. Münnich, J. C. McWilliams, T. Nagai, and G.-K. Plattner (2011), Eddy-induced reduction of biological production in eastern boundary upwelling systems, *Nature Geoscience*, *4*, 787-792, doi:10.1038/ngeo1273.

Haidvogel, D. B., et al. (2008), Ocean forecasting in terrain-following coordinates: Formulation and skill assessment of the Regional Ocean Modeling System, *Journal of Computational Physics*, *227*, 3595-3624, doi:10.1016/j.jcp.2007.06.016.

Haidvogel, D. B., A. Beckmann, and K. S. Hedström (1991), Dynamical simulations of filament formation and evolution in the coastal transition zone, *Journal of Geophysical Research*, *96*(C8), 15,017-015,040.

Huyer, A. (1983), Coastal upwelling in the California Current System, *Progress in Oceanography*, *12*, 259-284, doi:10.1016/0079-6611(83)90010-1.

Kosro, P. M., and A. Huyer (1986), CTD and velocity surveys of seaward jets off northern California, July 1981 and 1982, *Journal of Geophysical Research*, *91*(C6), 7680-7690, doi:10.1029/JC091iC06p07680.

Kurian, J., F. Colas, X. Capet, J. C. McWilliams, and D. B. Chelton (2011), Eddy properties in the California Current System, *Journal of Geophysical Research*, *116*, C08027, doi:10.1029/2010jc006895.

Lehahn, Y., F. d'Ovidio, M. Lévy, Y. Amitai, and E. Heifet (2011), Long range transport of a quasi isolated chlorophyll patch by an Agulhas ring, *Geophysical Research Letters*, *38*, L16610, doi:10.1029/2011GL048588.

Liang, J. H., J. C. McWilliams, and N. Gruber (2009), High-frequency response of the ocean to mountain gap winds in the northeastern tropical Pacific, *Journal of Geophysical Research: Oceans*, *114*(C12), doi:10.1029/2009JC005370.

Lovecchio, E., N. Gruber, and M. Münnich (2018), Mesoscale contribution to the long-range offshore transport of organic carbon from the Canary Upwelling System to the open North Atlantic, *Biogeosciences*, *15*, 5061-5091, doi:10.5194/bg-15-5061-2018.

Lynn, R. J., and J. J. Simpson (1987), The California Current System: The Seasonal Variability of its Physical Characteristics, *Journal of Geophysical Research*, *92*(C12), 12947-12966, doi:10.1029/JC092iC12p12947.

McWilliams, J. C. (2016), Submesoscale currents in the ocean, *Proceedings of the Royal Society A*, *472*, 20160117, doi:10.1098/rspa.2016.0117.

Mooers, C. N. K., and A. R. Robinson (1984), Turbulent jets and eddies in the California Current and inferred cross-shore transports, *Science*, *223*(4631), 51-53, doi:10.1126/science.223.4631.51.

Nagai, T., N. Gruber, H. Frenzel, Z. Lachkar, J. C. McWilliams, and G.-K. Plattner (2015), Dominant role of eddies and filaments in the offshore transport of carbon and nutrients in the California Current System, *Journal of Geophysical Research: Oceans*, *120*, 5318-5341, doi:10.1002/2015jc010889.

Pegliasco, C., A. Chaigneau, and R. Morrow (2015), Main eddy vertical structures observed in the four major Eastern Boundary Upwelling Systems, *Journal of Geophysical Research: Oceans*, *120*, 6008-6033, doi:10.1002/2015jc010950.

Sangrà, P., et al. (2009), The Canary Eddy Corridor: A major pathway for long-lived eddies in the subtropical North Atlantic, *Deep-Sea Research I*, *56*(12), 2100-2114, doi:10.1016/j.dsr.2009.08.008.

Schlax, M. G., and D. B. Chelton (2016), *The "growing method" of eddy identification and tracking in two and three dimensions*. Corvallis, OR: College of Earth, Ocean and Atmospheric Sciences, Oregon State University. Retrieved from http://wombat.coas.oregonstate.edu/eddies/Growing_Method_of_Eddy_Identification_and_Tracking.pdf.

Small, L. F., and F. G. Prahl (2004), A Particle Conveyor Belt Process in the Columbia River Estuary: Evidence from Chlorophyll *a* and Particulate Organic Carbon, *Estuaries*, *27*(6), 999-1003.

Snyder, M. A., L. C. Sloan, N. S. Diffenbaugh, and J. L. Bell (2003), Future climate change and upwelling in the California Current, *Geophysical Research Letters*, *30*(15), 1823, doi:10.1029/2003GL017647.

Stegmann, P. M., and F. Schwing (2007), Demographics of mesoscale eddies in the California Current, *Geophysical Research Letters*, *34*, L14602, doi:10.1029/2007GL029504.

Stramski, D., et al. (2008), Relationships between the surface concentration of particulate organic carbon and optical properties in the eastern South Pacific and eastern Atlantic Oceans, *Biogeosciences*, *5*, 171-201, doi:10.5194/bg-5-171-2008.

Strub, P. T., and C. James (2000), Altimeter-derived variability of surface velocities in the California Current System: 2. Seasonal circulation and eddy statistics, *Deep-Sea Research II*, *47*, 831-870, doi:10.1016/S0967-0645(99)00129-0.

Strub, P. T., P. M. Kosro, and A. Huyer (1991), The Nature of the Cold Filaments in the California Current System, *Journal of Geophysical Research*, *96*, 14,743-714,768.

Sullivan, B. E., F. G. Prahl, L. F. Small, and P. A. Covert (2001), Seasonality of phytoplankton production in the Columbia river: A natural or anthropogenic pattern?, *Geochimica et Cosmochimica Acta*, *65*(7), 1125-1139.

Sydeman, W. J., M. García-Reyes, D. S. Schoeman, R. R. Rykaczewski, S. A. Thompson, B. A. Black, and S. J. Bograd (2014), Climate change and wind

intensification in coastal upwelling ecosystems, *Science*, *345*(6192), 77-80, doi:10.1126/science.1250830.

Wang, Y., R. M. Castelao, and Y. Yuan (2015), Seasonal variability of alongshore winds and sea surface temperature fronts in Eastern Boundary Current Systems, *Journal of Geophysical Research: Oceans*, *120*, 2385-2400, doi:10.1002/2014jc010379.

Xiu, P., F. Chai, E. N. Curchitser, and F. S. Castruccio (2018), Future changes in coastal upwelling ecosystems with global warming: The case of the California Current System, *Scientific Reports*, *8*, 2866, doi:10.1038/s41598-018-21247-7.

Yuan, Y., and R. M. Castelao (2017), Eddy-induced sea surface temperature gradients in Eastern Boundary Current Systems, *Journal of Geophysical Research: Oceans*, *122*, 4791-4801, doi:10.1002/2017JC012735.

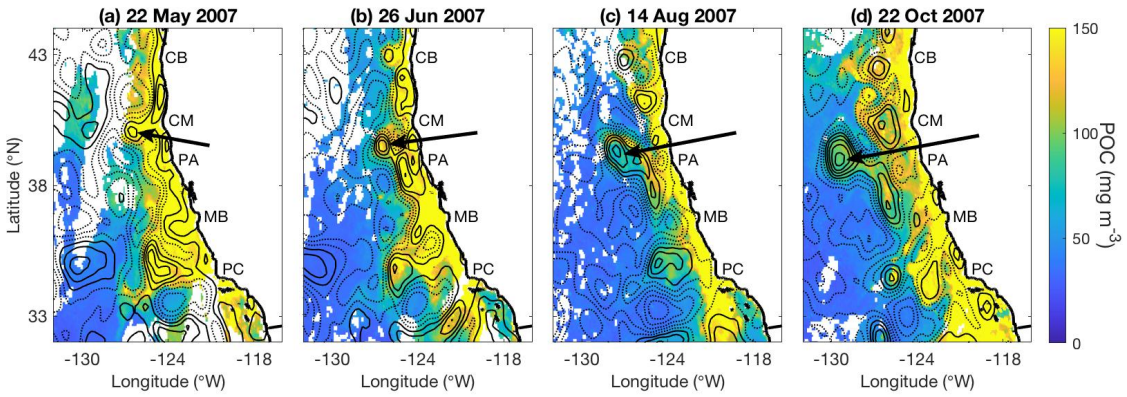

Figure 2.1. Example of offshore transport by an eddy in the California Current System. Particulate organic carbon (mg m^{-3}) derived from satellite observations and mean sea level anomaly contours from altimetry at 4 cm intervals on (a) 22 May 2007, (b) 26 June 2007, (c) 14 August 2007, and (d) 22 October 2007. Solid contours are negative. Arrows mark the location of a cyclonic eddy transporting coastal water rich in carbon offshore. CB: Cape Blanco; CM: Cape Mendocino; PA: Point Arena; MB: Monterey Bay; PC: Point Conception.

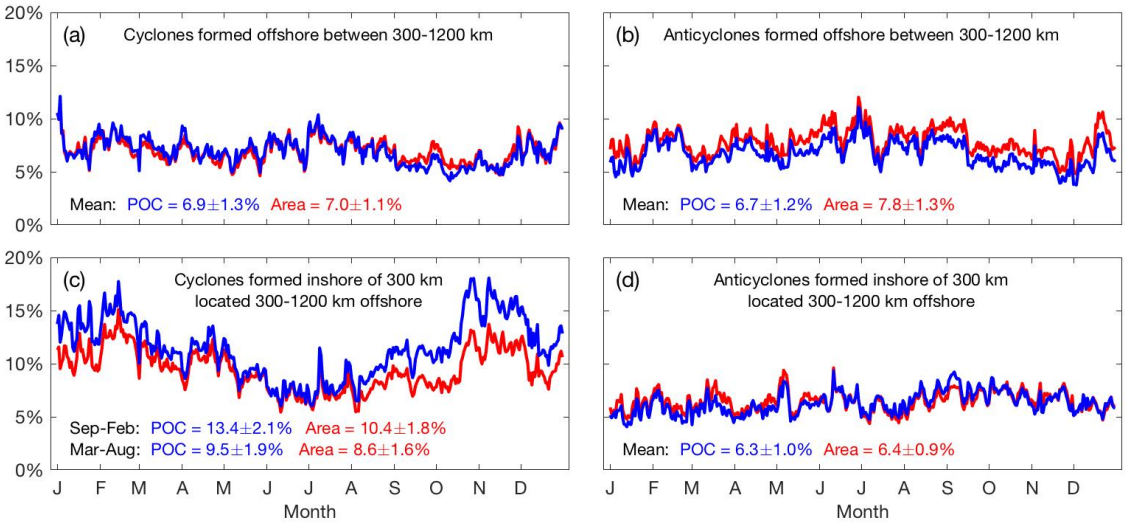

Figure 2.2. Carbon content and spatial area occupied by cyclonic and anticyclonic eddies (1997-2010). Percentage of the total amount of surface particulate organic carbon (blue line) and the total area (red line) between 300-1200 km from the coast that is inside all eddies for (a) cyclones and (b) anticyclones formed offshore between 300-1200 km from the coast and (c) cyclones and (d) anticyclones formed inshore of 300 km and located between 300-1200 km offshore.

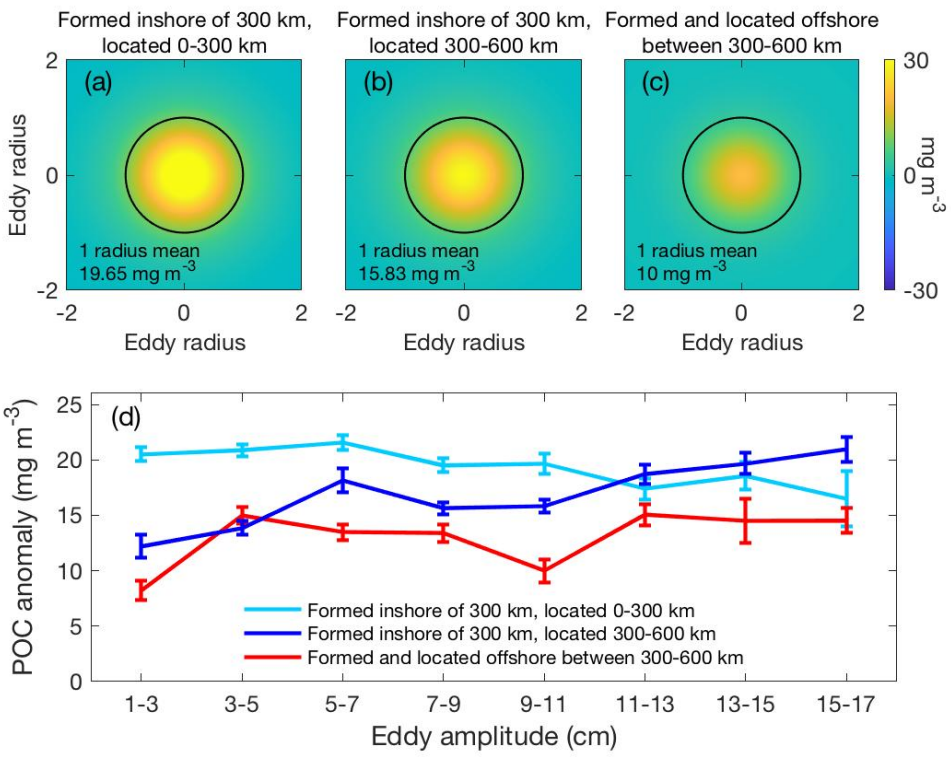

Figure 2.3. Particulate organic carbon composites and anomalies. Cyclonic eddies identified from satellite altimetry were collocated with particulate organic carbon (POC) anomalies that were derived from satellite observations. To isolate the POC signature associated with each eddy, the POC anomaly was extracted within 2 by 2 eddy radii from the eddy center and the distance from the eddy center was normalized by the eddy radius (unitless). A 2-D Gaussian function was fitted to each POC anomaly field and composites were computed by averaging the POC anomalies for eddies of similar amplitude (see Figure A.2). (a-c) Composites of POC anomalies within 2 by 2 eddy radii for cyclonic eddies with amplitudes 9-11 cm. Black circle represents the boundary for one eddy radius. (d) Mean POC anomaly (mg m^{-3}) and standard error within one eddy radius grouped by eddy amplitude.

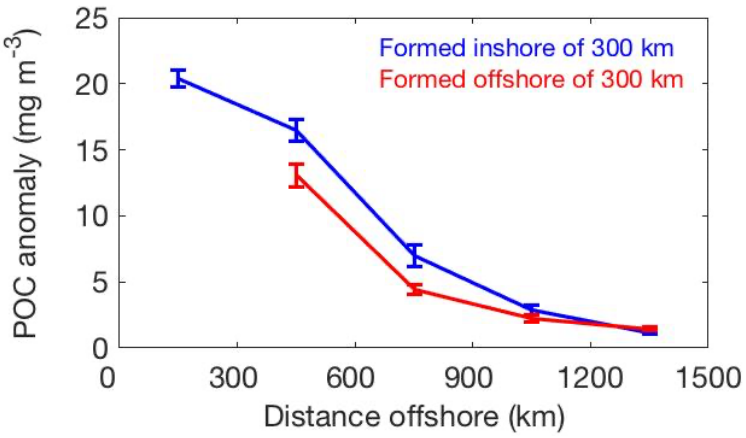

Figure 2.4. Particulate organic carbon anomaly as a function of distance from the coast. Mean particulate organic carbon anomaly (mg m^{-3}) and standard error within one eddy radius for cyclonic eddies formed inshore of 300 km from the coast (blue line) and for those formed offshore of 300 km (red line) as the eddies propagate offshore.

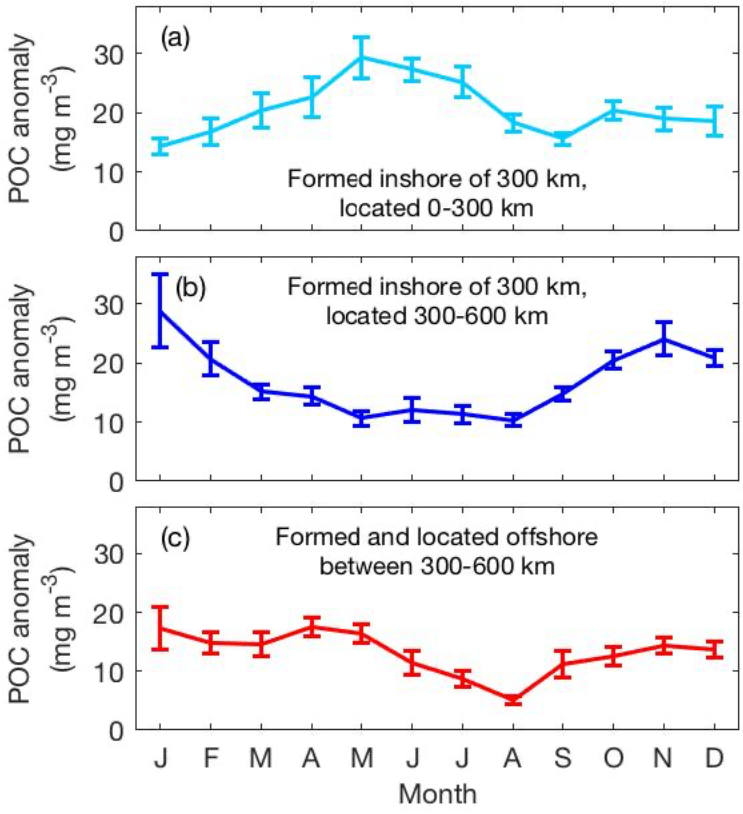

Figure 2.5. Monthly particulate organic carbon anomaly. Mean particulate organic carbon anomaly (mg m^{-3}) and standard error within one eddy radius as a function of the month of the eddy occurrence for cyclonic eddies (a) formed and located inshore of 300 km, (b) formed inshore of 300 km and propagated to 300-600 km offshore, and (c) formed and located offshore between 300-600 km.

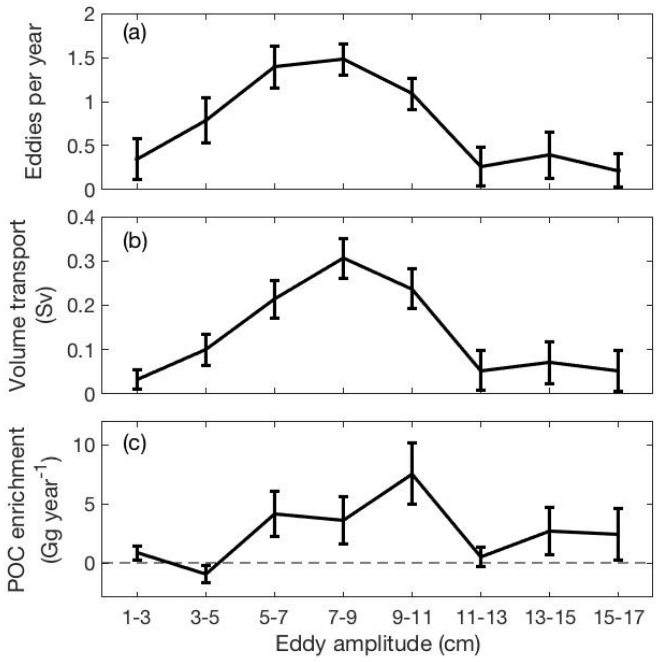

Figure 2.6. Estimates of lateral transport by cyclonic eddies in the California Current System. (a) Average number of cyclones with lifetime longer than 4 weeks in the eddy dataset[1] formed inshore of 300 km from the coast that propagate to at least 300 km offshore per year grouped by average amplitude of the eddies when they are located offshore of 300 km. Total number of cyclonic eddies propagating offshore per year is 6.0 ± 0.6. Error bars represent the standard error. (b) Mean volume transport (Sv) and standard error in the top 400 m by cyclonic eddies calculated assuming 65 ± 7% of the initially trapped volume of water is transported offshore (see Methods and Figure A.3). Total transport summed across the different amplitude bins is 1.06 ± 0.2 Sv. (c) Particulate organic carbon enrichment (Gg $year^{-1}$) and standard error in the offshore region due to cyclonic eddies generated inshore of 300 km from the coast that propagate offshore (see Figure A.5). Total particulate organic carbon enrichment summed across the different amplitude bins is 20.9 ± 11 Gg $year^{-1}$.

CHAPTER 3

OFFSHORE ENRICHMENT OF PARTICULATE ORGANIC CARBON BY MESOSCALE EDDIES IN EASTERN BOUNDARY CURRENT SYSTEMS [2]

[2] Amos, C.M. and R.M. Castelao. To be submitted to *Journal of Geophysical Research: Oceans*.

3.1. Abstract

Eastern Boundary Current Systems (EBCS) are highly productive ecosystems that are characterized by upwelling and rich mesoscale eddy activity. Cyclonic eddies that form near the coast can potentially trap upwelled coastal water and transport it offshore. The offshore transport of coastal water that is rich in carbon and nutrients in the EBCS could have important implications for the marine ecosystem. Here, we use mesoscale eddies detected from sea level anomalies and satellite-derived measurements of particulate organic carbon (POC) as a tracer of coastal water to quantify the eddy-induced offshore enrichment of POC in the four major EBCS. Our results indicate regions within each EBCS where cyclones located offshore that were generated near the coast contain higher carbon concentrations in their interior than cyclones of the same amplitude generated locally offshore. This is consistent with nonlinear cyclonic eddies that are generated near the coast that can trap coastal water rich in POC during formation and transport it offshore, producing offshore POC enrichments of 22.6 ± 5.1 Gg $year^{-1}$ (37-43°N), 16.1 ± 3.1 Gg $year^{-1}$ (34-42°S), 16.8 ± 6.1 Gg $year^{-1}$ (21-28°N), and 3.6 ± 3.1 Gg $year^{-1}$ (29-35°S) in the California, Humboldt, Canary and Benguela Current Systems, respectively. There is large spatial variability in the effectiveness of this transport mechanism, with the analyses indicating that regions downstream of an upwelling jet separation point are often characterized by increased eddy-induced transport. This study provides large-scale observational-based evidence that eddies play a quantitatively important role in the offshore transport of coastal water, substantially widening the area influenced by highly productive upwelled waters in some parts of the EBCS.

3.2. Introduction

Eastern Boundary Current Systems (EBCS) are highly productive ecosystems due to coastal upwelling (Huyer, 1983). The four major EBCS are the California and Humboldt Current Systems in the eastern Pacific Ocean (CCS and HCS, respectively) and the Canary and Benguela Current Systems in the eastern Atlantic Ocean (CanCS and BCS, respectively). Persistent alongshore equatorward winds during the local summer produce offshore surface Ekman transport and upwelling along the coast, bringing cold, nutrient-rich waters to the surface. This results in a band of elevated nutrients and particulate organic carbon (POC) concentrations near the coast (Huyer, 1983; Lynn and Simpson, 1987; Bakun and Nelson, 1991; Chavez and Messié, 2009; García-Reyes and Largier, 2012). Higher latitude regions in the four EBCS are generally characterized by equatorward, upwelling-favorable winds during local spring and summer and poleward, downwelling-favorable winds during winter (Bakun and Nelson, 1991; Carr and Kearns, 2003; Strub et al., 2019). The low- to mid-latitude regions differ from this seasonal cycle and feature year-round upwelling, e.g., to the south of ~39°N in the CCS and to the north of 35°S in the HCS (Chelton et al., 2007; Putrasahan et al., 2013; Strub et al., 2013).

Mesoscale eddies with radius on the order of 100 km are ubiquitous features in the EBCS (Haynes and Barton, 1991; Ramp et al., 1991; Strub et al., 1991; Capet et al., 2008a; Chaigneau et al., 2009; Chelton et al., 2011b) and are known to influence the horizontal and vertical distribution of physical and biogeochemical properties throughout the global ocean (Strub et al., 1991; Chaigneau et al., 2011; Chelton et al., 2011a; Gaube et al., 2013; Chenillat et al., 2015; Amores et al., 2017). As the coastal currents in the EBCS flow equatorward along the coast, meanders in the currents produce filaments that

can pinch off as cyclonic (counterclockwise in the Northern Hemisphere) and anticyclonic (clockwise) eddies which then propagate westward (Strub et al., 1991; Strub and James, 2000; Kurian et al., 2011; Nagai et al., 2015). The majority of these eddies are nonlinear (ratio of rotational speed to translational speed greater than 1), meaning they can theoretically trap water parcels and associated properties during formation (Chelton et al., 2011b) and can potentially transport the trapped properties for hundreds of kilometers throughout the ocean (Early et al., 2011; Lehahn et al., 2011). In the EBCS, eddies generated near the coast can potentially trap nutrients and properties in their interior that is associated with the upwelled coastal water (Gaube et al., 2014).

Modeling studies suggest that eddies can transport the trapped coastal water offshore, contributing to the redistribution of carbon, nutrients, and other properties in the CCS (Liang et al., 2009; Combes et al., 2013; Nagai et al., 2015; Chenillat et al., 2016) and in other upwelling systems (Lovecchio et al., 2018). Several previous observational studies have shown individual examples of eddies transporting materials in various regions of the ocean (Crawford et al., 2007; Lehahn et al., 2011; Gaube et al., 2014; Gaube and McGillicuddy Jr., 2017). Amos et al. (2019) investigated this on a larger scale by utilizing satellite-derived measurements of POC as a tracer of coastal water to show that cyclonic eddies located offshore that were generated near the coast contain higher carbon concentrations in their interior than cyclones of the same amplitude generated offshore in the CCS. Their analyses indicated that coastally-generated nonlinear eddies that propagate offshore can result in an eddy-induced volume transport of 1.06 ± 0.2 Sv and lead to the enhancement of surface POC in the offshore region of 20.9 ± 11 Gg year^{-1} in the CCS (Amos et al., 2019). Castelao et al. (2021) used the methodology in Amos et

al. (2019) to show that this process is also important along the West Antarctica Peninsula, demonstrating that transport by nonlinear eddies can also be significant in other regions in the ocean.

The four major EBCS share many similarities in mesoscale eddy activity and upwelling dynamics, (Figures 3.1-3.2; e.g., Chaigneau et al., 2009; Chavez and Messié, 2009; Pegliasco et al., 2015; Wang et al., 2015; Yuan and Castelao, 2017). Therefore, eddy-induced offshore enrichment of POC may also be important in the other EBCS. There are also many differences among these systems, however, including the degree of spatial variability within each EBCS with regard to upwelling, jet separation, and mesoscale activity (Chaigneau et al., 2009; Chavez and Messié, 2009; Chelton et al., 2011b; Strub et al., 2013; Wang et al., 2015; Yuan and Castelao, 2017). Thus, it is possible that eddy-induced offshore enhancement of POC will also vary spatially within these systems. Here, we apply the procedure developed in Amos et al. (2019) to the other major EBCS to quantify the offshore enrichment of POC by nonlinear cyclonic eddies in subregions within each EBCS and to identify regions where eddy-induced transport is most important. The offshore transport of coastal water that is rich in carbon and nutrients in the four major EBCS could have important implications for the marine ecosystem. Therefore, quantifying eddy-induced transport using observations is important for further understanding the influence of eddies in EBCS.

3.3. Data and Methods

3.3.1. Analyses Domain

The four major EBCS are included in this study. The California and Humboldt Current Systems (CCS and HCS, respectively) are located in the eastern Pacific Ocean and span 22-48°N and 4-56°S, respectively. The Canary and Benguela Current Systems (CanCS and BCS, respectively) are located in the eastern Atlantic Ocean and span 10-44°N and 8-35°N, respectively. Each EBCS is further divided into subregions based on the spatial variability of upwelling, mesoscale eddies, jet separation, etc. (e.g., Chaigneau et al., 2009; Chavez and Messié, 2009; Chelton et al., 2011b; Strub et al., 2013; Wang et al., 2015; Yuan and Castelao, 2017). The latitudinal extent of each subregion is shown in Figures 3.1-3.3 and listed in Table 3.1. Although it would be interesting to divide each EBCS into more subregions, that was not possible because many of the subregions would not include enough eddy occurrences to produce robust results.

3.3.2. Mesoscale Eddies

The location and characteristics of mesoscale eddies in EBCS were obtained from the fourth release of an existing global dataset of mesoscale eddies (Chelton et al., 2011b). To detect mesoscale eddies, daily sea level anomaly (SLA) fields produced by Archiving, Validation, and Interpretation of Satellite Oceanographic data (AVISO) are first spatially-filtered to remove large scale variability. Mesoscale eddies in the fourth release of the dataset are detected using a method that grows eddies from individual SLA extrema (Schlax and Chelton, 2016). The growing method starts with individual SLA extrema (positive for anticyclones and negative for cyclones) and finds all neighboring

pixels whose SLA values lie above a sequence of thresholds. An eddy is defined when the set of connected pixels satisfies a set of criteria used to define compact and coherent structures. Eddies are then tracked by pairing eddy realizations that are within allowable ranges of amplitude, radius and distance of the initial eddy at subsequent time steps. The eddy detection and tracking algorithms are described in detail in Chelton et al. (2011b) and Schlax and Chelton (2016).

Given the resolution of the AVISO satellite fields, only mesoscale eddies with radius larger than ~40 km are resolved, therefore submesoscale and smaller mesoscale variability are not included in the dataset and in the analyses. Complications in the eddy detection and tracking can arise when eddies merge or interact with other eddies or from noisiness in the SLA fields. This can result in imperfections in the detection of the boundaries and characteristics (e.g., radius, amplitude) of the eddies (Chelton et al., 2011b; Amores et al., 2018). Despite these limitations, animations of the eddy tracks on SLA fields indicated that the dataset captures most large mesoscale eddies in the EBCS.

Newer versions of the mesoscale eddy dataset are now being produced by the Data Unification and Altimeter Combination System (DUACS) team and distributed by AVISO+ (https://www.aviso.altimetry.fr/). The DUACS team follows the methodology developed by Chelton et al. (2011b) and Schlax and Chelton (2016), with the addition of upgrades to the algorithm to improve eddy identification and tracking. The newest version of the mesoscale eddy dataset was also used for this project. However, animations of the eddy tracks from both datasets overlayed on SLA fields indicated that as eddies propagate offshore, they often change shape, merge, or interact with other eddies, making the tracking difficult. The fourth release often identifies and tracks one

eddy continuously as it propagates into the offshore region, while this same eddy is often identified as multiple different eddies in the AVISO+ dataset as it interacts with other eddies in the offshore region (Figure B.1). SLA and POC fields show however that in most cases the newly identified eddy in the AVISO+ dataset still contains water of coastal origin, so it is still transporting coastal water offshore. Based on this comparison of the two datasets, we decided to use the fourth release of the dataset that was used in Amos et al. (2019).

Mesoscale eddies located in each EBCS (Figure 3.2) during the time period of the satellite POC data (1997-2010) were identified from the dataset for the analyses. Eddies are considered nonlinear if the ratio $U/c > 1$, where U is the maximum rotational speed and c is the translation speed of the eddy estimated at each point along its trajectory (Figures 3.3; Chelton et al., 2011b). The average nonlinearity parameter and the percentage of cyclonic eddies that are nonlinear in each subregion are listed in Table 3.1. The cumulative percentage of cyclonic eddies whose nonlinearity parameter is greater than a given threshold is shown in Figure B.2. The nonlinearity parameter was only calculated for cyclonic eddies located 0-300 km from the coast since this is where eddies are potentially trapping the coastal water. There were abnormally high nonlinear values associated with the tracking algorithm, e.g., an eddy didn't move based on the algorithm leading to very high U/c values (sometimes > 100). To exclude these values from the average calculations, the data above the 90th percentile were removed. The distance between the coastline and the location of the eddy centers at each point along the eddy trajectories was calculated to distinguish eddies generated or located inshore and offshore of 300 km from the coast. Following Amos et al. (2019), the threshold of 300 km from

the coast was chosen to define inshore and offshore based on the average width of the band of high POC concentrations along the coast. The band of high POC extends about 250 km from the coast on average in most parts of the EBCS (see section 3.3.3). Since POC is used here as a tracer of coastal water, a distance larger than the average width of the band with high POC was chosen to distinguish between upwelled coastal water and offshore water. The offshore region in each EBCS is defined as 300-600 km from the coast. This offshore width was chosen to be the same as the width of the inshore region (0-300 km). In the CanCS and BCS between 10-21°N and 8-23°S, respectively, the band with high POC concentrations along the coast is wider than 300 km (Figure 3.1). As a result, eddies generated offshore in these subregions (based on our distance threshold of 300 km) will be influenced by the coastal water and contain high POC anomalies. Since we are applying the threshold of 300 km to all subregions in the EBCS, we excluded these subregions from the analyses for now.

The volume transport by cyclonic eddies was calculated as

$$\textit{Volume transport}\ (\mathrm{Sv}) = (\textit{eddy area} \times \textit{trapping depth} \times N \times \textit{trapping efficiency}) \,/\, T \quad \text{(Eq. 1)}$$

where N is the number of cyclones per year for each amplitude bin that are generated inshore of 300 km from the coast and propagate offshore of 300 km and T is the number of seconds in 1 year. We use an average trapping depth inside cyclonic eddies of 400 m for all subregions (Kurian et al., 2011; Amos et al., 2019). Trapping efficiency is the percentage of initially trapped water that remains inside eddies after they propagate

offshore and is used to account for water leaking from the eddies. Amos et al. (2019) estimated a trapping efficiency of 65 ± 7% in the CCS using an ocean model. Since we do not have model implementations for the other EBCS, we cannot compute this here and chose to set the trapping efficiency at 1, as in many other studies (Sangrà et al., 2009; Dong et al., 2014; Lovecchio et al., 2018). As a result, the volume transports presented here are likely overestimated. This may be especially true in regions where the nonlinearity parameter (U/c) is larger than but close to 1 (Figure 3.3). The volume transport in each amplitude bin was then summed to compute the total volume transport in each subregion.

3.3.3. Particulate Organic Carbon Measurements

Daily POC data available from September 1997 to December 2010 at 9 km resolution were obtained from NASA's OceanColor Web (https://oceancolor.gsfc.nasa.gov/; Figure 3.1). POC is calculated using an empirical relationship derived from in situ measurements of POC and blue-to-green band ratios of remote sensing reflectances from Sea-Viewing Wide Field-of-View Sensor (SeaWiFS; Stramski et al., 2008). Following the methodology in Amos et al. (2019), the POC data were first averaged at a 7-day interval to reduce the influence of cloud coverage (see Figure A.2a). The mesoscale structures that are of primary interest here are obscured by the large-scale POC background distribution. Spatial high-pass filtering (Chelton et al., 2004; Schlax and Chelton, 2016) the weekly POC fields (6° longitude by 6° latitude window) to remove the large-scale patterns allowed for isolating the POC anomaly associated with mesoscale activity in the region (Gaube et al., 2013; Gaube et al., 2014;

Gaube and McGillicuddy Jr., 2017; Amos et al., 2019; Figure A.2b). Cyclonic eddies, which were identified using altimetry data (Chelton et al., 2011b; black box in Figure A.2b), were generally characterized by positive POC anomalies, while anticyclones were generally associated with negative POC anomalies in the four EBCS.

To further isolate the signature associated with each eddy from other mesoscale features, we extracted the POC anomaly within 2 by 2 eddy radii from the eddy center (Amos et al., 2019; Figure A.2c). To facilitate comparisons among eddies of various radii, the distance from the eddy center was normalized by the eddy radius on each 2 by 2 radii grid (Gaube et al., 2014; Amos et al., 2019; Figure A.2c). Only eddies with at least 90% cloud-free pixel coverage for POC data within one eddy radius and 75% pixel coverage within two eddy radii (black box in Figure A.2b) were used. To remove noisy, small-scale variability not related to the eddy, a 2-D Gaussian function was fitted to the resulting POC anomaly field (Yuan and Castelao, 2017; Amos et al., 2019). The fit is consistent with the average eddy shape which is well represented as Gaussian (Chelton et al., 2011b). Lastly, the center of the Gaussian fitted POC anomaly was shifted to align with the center of the eddy (Figure A.2d). Visual inspections of the POC anomaly fields indicated that large anomalies associated with other mesoscale features (e.g., upwelling front, filaments) are often observed around individual eddies, especially around the edges of the 2 by 2 eddy radii boxes, which influence the composites of the POC anomalies for each eddy amplitude bin. Using the Gaussian fit allowed for the eddy signature to be isolated from the signature of these other mesoscale features. For each subregion, composites were then computed by averaging the POC anomalies for eddies of similar amplitudes for cyclones generated and located inshore of 300 km, cyclones generated

inshore of 300 km and located offshore, and cyclones generated locally offshore (Figure 3.5). A t-test was used to determine the amplitude bins for which the difference in the POC anomalies between the two latter groups of cyclones were statistically significant.

In situ POC concentrations were measured in the southern CCS since 2006 as part of the CCS Long Term Ecological Research monitoring efforts (Aluwihare, 2018). Data availability is larger at the surface, decreasing significantly below 100 m depth. A depth range of 100 m for estimating organic carbon fluxes has been used in previous modeling studies (Lovecchio et al., 2018). Surface concentrations of POC and POC integrated from the surface to 100 m depth were found to be correlated off Antarctica (Allison et al., 2010). Amos et al. (2019) used in situ POC data in the CCS and found these to be correlated there too, suggesting that this relationship holds in multiple systems. This allowed for the integrated POC content in the top 100 m to be estimated from satellite data. Integrated POC anomalies were extracted from each eddy following the procedure described above. Those anomalies were then used to calculate the offshore enrichment of POC (Gg year^{-1}) in the top 100 m by eddies as

$$\textit{POC enrichment}\ (\text{Gg year}^{-1}) = \Delta(POC_{100}) \times \textit{eddy area} \times N \qquad \text{(Eq. 2)}$$

where $\Delta(POC_{100})$ is the difference between the integrated POC content inside cyclones located offshore that were generated near the coast and those generated offshore for each amplitude bin and N is the number of eddies per year for each amplitude bin that are generated inshore of 300 km from coast and propagate offshore. The POC enrichment was then summed for all amplitude bins where the difference between the POC

anomalies for cyclones generated inshore that are located offshore and cyclones generated locally offshore were statistically significant (t-test, $p < 0.1$; see Figure 3.5 for significant amplitude bins) to calculate the total offshore POC enrichment. The offshore POC enrichment in each subregion was also computed using all amplitude bins, not just the ones with differences that were statistically significant. The results were very similar in most subregions, except for subregion 1 in the HCS. The POC enrichment was artificially high and had large errors in this subregion (i.e., although high, the calculated enrichments were not statistically different than zero), despite the small differences in the POC anomalies in each amplitude bin. This is due to the large number of cyclones generated inshore per year and these cyclones having larger radii since they are located at lower latitudes (Chelton et al., 2011b). Some amplitude bins within each subregion had very few eddy occurrences, producing results that are not robust. Amplitude bins with fewer than 10 eddy occurrences were excluded from the analyses.

The relationship between in situ POC at the surface and integrated to 100 m depth in the southern CCS is initially used to compute the integrated POC in all EBCS. This relationship may not hold true in the northern CCS and in the CanCS, HCS, and BCS, however, the lack of long term in situ data makes it difficult to determine this relationship in these regions. Future work will use in situ POC measurements collected in the other EBCS (if available) to determine the relationship between surface POC and POC integrated to 100 m depth. Those relationships will then be used to recalculate the offshore POC enrichment in each respective EBCS.

3.4. Results

Meanders and filaments (Haidvogel et al., 1991) extend westward from the coastal equatorward currents in the EBCS and are often distinguished by elevated POC concentrations as they initiate the offshore transport of coastal water, as shown in the HCS (Figure 3.4a). A filament can pinch off as a cyclonic eddy (Figure 3.4b-c), entraining upwelled coastal water that is rich in carbon and nutrients. The trapped coastal water can then be transported offshore for hundreds of kilometers as indicated by elevated POC concentrations remaining months later in the interior of the eddy compared to the surrounding offshore waters (Figure 3.4d). These regions are often highly energetic, with multiple mesoscale features influencing the redistribution of coastal water in the offshore region (Figure 3.4). Although nonlinear anticyclonic eddies are also capable of trapping and transporting materials, they have less of an impact on the redistribution of recently upwelled coastal water in the EBCS compared to cyclones due to differences in the water that is entrained during formation. Amos et al. (2019) looked at the time evolution of POC content inside eddies generated near the coast that moved offshore compared to eddies generated locally offshore. They found a difference in the amount of POC between the two groups of cyclones but not for anticyclones (see Figure 2 in Amos et al., 2019), which further suggests that anticyclones make a smaller contribution to the offshore transport of coastal water compared to cyclones.

To detect eddies transporting trapped coastal water via satellite observations in each EBCS, the anomalous POC signature associated with each eddy was isolated and compared between cyclones generated inshore and offshore of 300 km from the coast (see Figures A.1 and A.2 for the CCS). In most of the EBCS, cyclonic eddies are

associated with positive POC anomalies (Figure 3.5). In the CCS, cyclonic eddies that are generated inshore and propagate offshore of 300 km from the coast have higher POC anomalies than cyclones of the same amplitude generated offshore between 300 and 600 km for amplitudes greater than 3 cm in subregion 2 (t-test, $p < 0.05$; Figure 3.5), downstream of Cape Blanco. This pattern is also observed in subregion 5 off southern Baja California for cyclones with amplitudes 1-7 cm and 11-13 cm (Figure 3.5). In subregion 3, significant differences in the POC anomalies only occur for amplitudes 1-3 cm and 11-13 cm. This relationship is not observed for most of the amplitudes in subregions 1 (north of Cape Blanco) and 4 (northern Baja California) (Figure 3.5). The larger POC anomalies in the cyclones generated inshore that are located offshore in comparison to those generated offshore could be due to the offshore transport of the POC that was trapped during eddy formation near the coast, to remineralization of the trapped POC and recycling into new carbon, and to local production as the eddy propagates offshore through the utilization of nutrients that were trapped at formation (Amos et al., 2019). All of these sources of POC are influenced by the trapping of POC- and nutrient-rich coastal upwelled water by cyclonic eddies during formation and subsequent offshore lateral transport.

The mean volume transport by cyclones for each subregion is calculated by using the average volume associated with cyclonic eddy occurrences of different amplitudes that are generated near the coast and then propagate offshore and the number of these cyclonic eddies that are generated per year (Equation 1). The nonlinearity parameter ($U/c > 1$) was calculated to determine if these eddies are nonlinear and therefore capable of trapping and transporting coastal water (Figures 3.3 and B.2). Also assumed in the

volume transport calculation is a trapping efficiency of 1, meaning none of the trapped coastal water is leaking from the interior of the eddies as they propagate offshore. We focus on cyclones because of their larger influence on the offshore transport of coastal water that is influenced by upwelling compared with anticyclones (Amos et al., 2019), as mentioned above. Because not all subregions have the same latitudinal extent, we further normalize the volume transport by each subregions' extent. In the CCS, per degree latitude, subregion 5 has the highest number of cyclones that are generated inshore and propagate offshore of 300 km per year and the largest volume transport by these eddies (Table 3.2). The number of cyclones generated per year and the volume transport is only marginally less in subregions 2-4. The total number of cyclones generated per year for subregions 2-5 ranges from 2.2 to 3.6 and 93-94% of the cyclonic eddy occurrences are nonlinear (Table 3.1). The total volume transport in each of these subregions is 0.60-0.96 Sv (1 Sv = 10^6 m^3 s^{-1}). Subregion 1 to the north of Cape Blanco has the fewest cyclones generated inshore per year, the smallest volume transport, and lowest percentage of eddy occurrences that are nonlinear (Tables 3.1-3.2).

The relationship between in situ POC at the surface and integrated from the surface to 100 m depth (see Figure A.4; Allison et al., 2010) is used to estimate the amount of POC that is added to the offshore region by cyclonic eddies generated near the coast that are trapping the upwelled coastal water and transporting it offshore. For that calculation, the differences in the POC content between cyclonic eddies located 300-600 km offshore that were formed inshore of 300 km and those formed offshore between 300-600 km from the coast are used (only the amplitude bins that are statistically different; Equation 2). The offshore enrichment of POC due to the lateral transport by cyclonic

eddies is largest per degree latitude in subregion 2 and second largest in subregion 5 (Table 3.2). Subregions 2 and 5 have total offshore POC enrichments of 22.6 ± 5.1 Gg year^{-1} and 4.4 ± 1.2 Gg year^{-1}, respectively (Table 3.1). Subregion 3 is characterized by a smaller offshore POC enrichment of 1.1 ± 0.9 Gg year^{-1}. There is no significant offshore enrichment of POC in subregion 1 and it was not calculated for subregion 4 because none of the amplitude bins had POC anomalies that were statistically different (Table 3.1; Figure 3.5). The results for the number of eddies generated, volume transport, and offshore POC enrichment in 33-43°N (subregions 2 and 3 combined) are consistent with Amos et al. (2019).

In the HCS, cyclonic eddies that are generated inshore and propagate offshore of have higher POC anomalies than cyclones of the same size generated offshore for all amplitudes in subregion 3, which encompasses the area downstream of Punta Lavapie (Figure 3.5). Outside of subregion 3, this relationship is only observed in subregion 4 for cyclones with amplitudes 1-3 cm. Per degree latitude, subregion 2 has the most cyclones generated inshore per year and subregion 1 has the largest volume transport by cyclones (Table 3.2). The total number of cyclones generated in subregion 1 is 11.9 ± 0.5 per year and the volume transport is 6.25 ± 0.35 Sv, however this is the largest subregion in the HCS (Table 3.1). The nonlinearity parameter in this subregion is also low, so it is possible that using a trapping efficiency of 1 in Equation 1 introduces larger errors in this subregion (Table 3.1; Figure 3.3). In subregions 1-3, 78-88% of the cyclonic eddy occurrences are nonlinear and only 62% in subregion 4. Despite subregion 3 having a lower number of cyclones generated inshore per year and less volume transport per degree latitude compared to the other subregions, it has the highest offshore POC

enrichment per degree latitude (Table 3.2). In subregion 3, 4.1 ± 0.4 cyclones are generated inshore and propagate offshore per year and the total offshore enrichment of POC in subregion 3 is 16.1 ± 3.1 Gg year^{-1} (Table 3.1). Although subregion 1 has a large number of cyclonic eddies generated per year and a large volume transport, no offshore POC enrichment was calculated for this subregion because none of the amplitude bins had POC anomalies that were statistically different (Figure 3.5).

In the CanCS, subregion 3 has higher POC anomalies associated with cyclonic eddies generated inshore that are located offshore compared to cyclones generated offshore for amplitudes 3-7 cm and the difference in the anomalies is larger in this subregion than in subregions 1 and 2 (Figure 3.5). POC anomalies associated with cyclones generated inshore are also slightly higher than those generated offshore in subregion 2 for amplitudes 1-3 cm and 5-7 cm (Figure 3.5). Per degree latitude, subregion 3 has the largest number of cyclones generated inshore per year and the largest volume transport (Table 3.2), with a total of 4.6 ± 0.5 cyclones generated per year and a volume transport of 1.22 ± 0.14 Sv (Table 3.1). This volume transport is consistent with the westward transport by eddies estimated by Sangrà et al. (2009) between 22-29°N in the CanCS (1.3 Sv in the top 300 m). In subregion 3, 77% of the cyclonic eddy occurrences are nonlinear. The highest offshore POC enrichment per degree latitude also occurs in subregion 3, with a total POC enrichment of 16.8 ± 6.1 Gg year^{-1} (Tables 3.1-3.2). Subregion 2 has an offshore POC enrichment of 1.8 ± 0.5 Gg year^{-1}, with 83% of cyclones being nonlinear, and there is no significant offshore enrichment in subregion 1 (Table 3.1).

In the BCS, the POC anomalies inside cyclones generated inshore that are located offshore are statistically different than cyclones generated offshore for amplitudes 9-17 cm in subregion 2 (Figure 3.5). None of the amplitude bins in subregion 1 are statistically different. Per degree latitude, more cyclones are generated inshore per year and the volume transport is higher in subregion 1 compared to subregion 2 (Table 3.2). In total, 4.1 ± 0.5 cyclones are generated per year and the volume transport is 1.16 ± 0.19 Sv, which is comparable to subregions in the other EBCS (Table 3.1). The percentage of cyclones generated inshore that are nonlinear in the BCS is 84% in subregion 1 and 93% in subregion 2, with higher nonlinear values observed in subregion 2 (Table 3.1; Figure 3.3). The offshore POC enrichment in subregion 2 is 3.6 ± 3.1 Gg $year^{-1}$ (Table 3.1). The POC enrichment was not calculated in subregion 1 because none of the amplitude bins had POC anomalies that were statistically different (Figure 3.5).

3.5. Discussion

Amos et al. (2019) used new methodology to present large-scale observational evidence that the process of nonlinear mesoscale eddies trapping coastal water and then propagating offshore is important enough to produce a signature in cyclonic eddies far from the coast in the CCS. This study expands on that research by investigating this process in all major EBCS and identifying subregions within each EBCS where eddy-induced transport is most important. Our results indicate that the enrichment of POC in offshore regions is associated with offshore propagating nonlinear cyclonic eddies that are capable of trapping carbon- and nutrient-rich coastal water during formation. This

cross-shelf transport is important for increasing the area influenced by highly productive upwelled waters in the EBCS.

In the CCS and HCS, the subregions with large offshore enrichment of POC by cyclonic eddies occur in approximately the same latitudinal bands, 37-43°N and 34-42°S, respectively. The mid-latitude subregions in the CCS and HCS with enhanced POC enrichment feature intense upwelling, high eddy activity, and cyclonic eddies that are highly nonlinear (Figures 3.1-3.3). This subregion in the CCS features Cape Blanco (43°N), where the upwelling jet separates from the coast (Barth et al., 2000; Strub and James, 2000). This also occurs in the HCS at Punta Lavapie (37°S; Mesias et al., 2003; Aguirre et al., 2012). Jet separation can result in the development of an intense meandering flow regime that dominates the circulation in coastal regions and strongly influences eddy activity downstream of the separation point (Barth et al., 2000; Strub and James, 2000; Capet et al., 2008b; Chaigneau et al., 2009; Castelao and Luo, 2018). There is also a significant increase in the nonlinearity of cyclonic eddies downstream of the separation point in both the CCS and the HCS. This analysis points to two conditions that are important for eddy-induced transport. First, there need to be nonlinear cyclonic eddies that are generated near the coast, since eddy-induced transport scales with the number of eddies propagating offshore. Second, the band with high POC concentrations needs to be wide enough for the eddies to be able to trap the coastal water that is rich in POC. The eddy data is only available offshore of about 50 km and the radius of most eddies detected by satellite altimetry is on the order of 100 km (Chelton et al., 2011b). Therefore, the band with high POC concentrations needs to be at least 150-200 km wide for this mechanism to be important for the eddies that we can resolve. The jet separation

in these regions contributes to the widening of the high POC band and the formation of eddies, thus it is important for creating favorable conditions for eddy-induced offshore transport.

Enhanced subregions of offshore POC enrichment in the CanCS and BCS occur a slightly farther equatorward, 21-28°N and 29-35°S, respectively compared to the CCS and HCS. This subregion in the CanCS also coincides with jet separation at Cap Blanc (21°N; Meunier et al., 2012). In the BCS, the jet separates from the coast near Cape Columbine (33°S; Veitch et al., 2018). These results for the CanCS and BCS are somewhat surprising. In the BCS, the offshore transport near Cape Columbine is small, even though jet separation occurs there (Penven et al., 2000). Cape Columbine is located very close to the southern tip of Africa and the location of the Agulhas Current separation. This differs from the capes with jet separation in the CCS and HCS which are bounded by longer stretches of coastline on both sides of the capes. Also, in the analysis we focused on cyclonic eddies generated near the coast, so we are not including the large anticyclonic Agulhas Current rings. However, the cyclones in this subregion are highly nonlinear (Figure 3.3), indicating that Agulhas rings may influence the local circulation in this region and possibly the offshore propagation of coastally-generated cyclones. In the CanCS, jet separation and mesoscale activity also occur along the west coast of the Iberian Peninsula (subregion 1; Haynes et al., 1993; Røed and Shi, 1999; Peliz et al., 2002; Relvas and Barton, 2002), however, there is no significant offshore enrichment of POC in this subregion. The cyclonic eddies generated near the coast in this subregion have lower nonlinearity values (Table 3.1; Figure 3.3), so they may not be trapping as much of the coastal water. Also, the coastal band with high POC concentrations is very

narrow. This is important because the band with high POC concentrations needs to be wide enough for eddies to trap this water, as discussed above. If the band is too narrow, then water cannot be trapped by the large eddies that are included in the analyses. For narrower POC bands, submesoscale eddies (radius on the order of 10 km) could play an important role in trapping and transporting the coastal water offshore (Capet et al., 2008c; McWilliams, 2016; Dauhajre et al., 2017). Using current altimetry data, however, only eddies with radii larger than 40-50 km are detectable (Chelton et al., 2011b). Future studies using SWOT (NASA's Surface Water and Ocean Topography mission; Fu et al., 2012), which will provide sea level anomalies at higher resolution, can investigate the role of smaller eddies on offshore transport in the EBCS.

In all EBCS, the process of offshore transport by eddies is important, but there is substantial spatial variability in where this occurs. In most cases the enhanced transport is found in regions where we would expect, e.g., downstream of Cape Blanco and Punta Lavapie where jet separation widens the band with high POC concentrations and increases eddy activity. This supports our interpretation that the difference in the POC anomalies associated with cyclones generated inshore that move offshore and those generated locally offshore is not just noise or uncertainty but rather real and associated with eddy-driven transport. As mentioned above, jet separation is important for contributing to the offshore extension of coastal water, inducing a cross-shelf transport of 1-2 Sv (Mooers and Robinson, 1984; Kosro and Huyer, 1986; Barth et al., 2000; Castelao and Barth, 2005; Aguirre et al., 2012; Veitch et al., 2018). However, this mechanism is generally confined to about 400 km offshore (Lynn and Simpson, 1987; Strub and James, 2000; Barth et al., 2005). Eddies in these regions produce similar volume transports

(Table 3.1), but their influence can extend much farther offshore (Amos et al., 2019). This eddy-induced transport will affect heat and salt fluxes (Dong et al., 2014) and widen the area influenced by upwelling circulation and coastal production. Eddies generated near the coast are likely trapping POC with a different composition compared to the composition of the POC found offshore. As this coastal POC is transported offshore, it can help support a variety of processes in the offshore region, which may have important ecological implications. For example, the coastal waters that are trapped during eddy formation are influenced by recent coastal production, which is known to add labile compounds, such as saccharides and low molecular weight fatty acids, to the carbon pool (Ahlgren et al., 1992; Medeiros et al., 2012; Medeiros et al., 2015). When this material is redistributed offshore, via eddies for example, it provides a pathway for coastal production to help support heterotrophic microorganisms away from the coast. Activity by microorganisms has been shown to vary strongly as a function of POC composition (Satinsky et al., 2014), therefore this transport mechanism may drive changes in microbial community composition (Doherty et al., 2017).

There are several limitations in our estimates of volume transport and offshore POC enrichment. Imperfections in the eddy detection and tracking algorithm can make it difficult to accurately identify eddies (Chelton et al., 2011b; Amores et al., 2018). As a result, there may be errors in the eddy characteristics, such as radius and amplitude, which could affect the transport calculations. Also, as mentioned above, only eddies with radii larger than 40-50 km are detectable with current altimetry data (Chelton et al., 2011b). Submesoscale eddies may also contribute to the redistribution of coastal upwelled water (Capet et al., 2008c; McWilliams, 2016; Dauhajre et al., 2017), but they

are not included here. Our estimates of volume transport and offshore POC enrichment may be higher if these smaller eddies are included. Lastly, the relationship between surface POC concentrations and POC content in the top 100 m was based on in situ POC data in the southern CCS only. This relationship was applied to all EBCS subregions, but this may not hold true in the northern CCS and in the CanCS, HCS and BCS, which leads to uncertainties in our estimates of offshore POC enrichment in these regions. Given these uncertainties and limitations, it is difficult to estimate if the eddy-induced enrichment of POC in the offshore waters is an important component of the carbon budget in this region. The enrichment of POC in the offshore region associated with cyclonic eddies that are generated inshore and move offshore may be an important component driving local POC variability offshore, even if the contribution to the total offshore POC stock is small.

3.6. Acknowledgements and Data

This work was supported by NASA Headquarters under the NASA Earth and Space Science Fellowship Program - Grant 80NSSC18K1342. The fourth release of the global mesoscale eddy dataset is available at http://wombat.coas.oregonstate.edu/eddies/index.html. The new Mesoscale Eddy Trajectory Atlas products are produced by SSALTO/DUACS and distributed by AVISO+ (http://www.aviso.altimetry.fr/) with support from CNES, in collaboration with Oregon State University with support from NASA. The satellite-derived POC data are available at NASA's OceanColor Web (https://oceancolor.gsfc.nasa.gov/).

References

Aguirre, C., Ó. Pizarro, P. T. Strub, R. Garreaud, and J. A. Barth (2012), Seasonal dynamics of the near-surface alongshore flow off central Chile, *Journal of Geophysical Research: Oceans*, *117*(C1), doi:10.1029/2011JC007379.

Ahlgren, G., I. B. Gustafsson, and M. Boberg (1992), Fatty acid content and chemical composition of freshwater microalgae, *Journal of phycology*, *28*(1), 37-50, doi:10.1111/j.0022-3646.1992.00037.x.

Allison, D. B., D. Stramski, and B. G. Mitchell (2010), Seasonal and interannual variability of particulate organic carbon within the Southern Ocean from satellite ocean color observations, *Journal of Geophysical Research*, *115*, C06002, doi:10.1029/2009jc005347.

Aluwihare, L. (2018), Particulate organic carbon and nitrogen measurements at selected depths in the water column in the CCS region since 2006 - 2016 (ongoing), edited by E. D. Initiative, doi:10.6073/pasta/20c05dd205be2225ecb32a5fede1c36c.

Amores, A., G. Jordà, T. Arsouze, and J. Le Sommer (2018), Up to what extent can we characterize ocean eddies using present-day gridded altimetric products?, *Journal of Geophysical Research: Oceans*, *123*, 7220-7236, doi:10.1029/2018JC014140.

Amores, A., O. Melnichenko, and N. Maximenko (2017), Coherent mesoscale eddies in the North Atlantic subtropical gyre: 3-D structure and transport with application to the salinity maximum, *Journal of Geophysical Research: Oceans*, *122*, 23-41, doi:10.1002/2016JC012256.

Amos, C. M., R. M. Castelao, and P. M. Medeiros (2019), Offshore transport of particulate organic carbon in the California Current System by mesoscale eddies, *Nature Communications*, *10*, 4940, doi:10.1038/s41467-019-12783-5.

Bakun, A., and C. S. Nelson (1991), The Seasonal Cycle of Wind-Stress Curl in Subtropical Eastern Boundary Current Regions, *Journal of Physical Oceanography*, *21*(12), 1815-1834, doi:10.1175/1520-0485(1991)021<1815:TSCOWS>2.0.CO;2.

Barth, J. A., S. D. Pierce, and T. J. Cowles (2005), Mesoscale structure and its seasonal evolution in the northern California Current System, *Deep-Sea Research II*, *52*(1-2), 5-28, doi:10.1016/j.dsr2.2004.09.026.

Barth, J. A., S. D. Pierce, and R. L. Smith (2000), A separating coastal upwelling jet at Cape Blanco, Oregon and its connection to the California Current System, *Deep-Sea Research II*, *47*, 783-810, doi:10.1016/S0967-0645(99)00127-7.

Capet, X., F. Colas, J. C. McWilliams, P. Penven, and P. Marchesiello (2008a), Eddies in eastern boundary subtropical upwelling systems, *Ocean Modeling in an Eddying Regime*, *177*, 350, doi:10.1029/177GM10.

Capet, X., J. C. McWilliams, M. J. Molemaker, and A. Shchepetkin (2008b), Mesoscale to submesoscale transition in the California Current System. Part II: Frontal processes, *Journal of Physical Oceanography*, *38*, 44-64, doi:10.1175/2007JPO3672.1.

Capet, X., J. C. McWilliams, M. J. Molemaker, and A. F. Shchepetkin (2008c), Mesoscale to submesoscale transition in the California Current System. Part I:

Flow structure, eddy flux, and observational tests, *Journal of Physical Oceanography*, *38*, 29-43, doi:10.1175/2007JPO3671.1.

Carr, M.-E., and E. J. Kearns (2003), Production regimes in four Eastern Boundary Current systems, Deep Sea Research Part II: Topical Studies in Oceanography, 50(22-26), 3199-3221, doi:0.1016/j.dsr2.2003.07.015.

Castelao, R. M., and J. A. Barth (2005), Coastal ocean response to summer upwelling favorable winds in a region of alongshore bottom topography variations off Oregon, *Journal of Geophysical Research*, *110*, C10S04, doi:10.1029/2004JC002409.

Castelao, R. M., M. S. Dinniman, C. M. Amos, J. M. Klinck, and P. M. Medeiros (2021), Eddy-Driven Transport of Particulate Organic Carbon-Rich Coastal Water Off the West Antarctic Peninsula, *Journal of Geophysical Research: Oceans*, *126*(3), e2020JC016791, doi:10.1029/2020JC016791.

Castelao, R. M., and H. Luo (2018), Upwelling jet separation in the California Current System, *Scientific Reports*, *8*, 16004, doi:10.1038/s41598-018-34401-y.

Chaigneau, A., G. Eldin, and B. Dewitte (2009), Eddy activity in the four major upwelling systems from satellite altimetry (1992–2007), *Progress in Oceanography*, *83*, 117-123, doi:10.1016/j.pocean.2009.07.012.

Chaigneau, A., M. Le Texier, G. Eldin, C. Grados, and O. Pizarro (2011), Vertical structure of mesoscale eddies in the eastern South Pacific Ocean: A composite analysis from altimetry and Argo profiling floats, *Journal of Geophysical Research*, *116*, C11025, doi:10.1029/2011JC007134.

Chavez, F. P., and M. Messié (2009), A comparison of Eastern Boundary Upwelling Ecosystems, *Progress in Oceanography*, *83*, 80-96, doi:10.1016/j.pocean.2009.07.032.

Chelton, D. B., P. Gaube, M. G. Schlax, J. J. Early, and R. M. Samelson (2011a), The Influence of Nonlinear Mesoscale Eddies on Near-Surface Oceanic Chlorophyll, *Science*, *334*, 328-334, doi:10.1126/science.1208897.

Chelton, D. B., M. G. Schlax, M. H. Freilich, and R. F. Milliff (2004), Satellite measurements reveal persistent small-scale features in ocean winds, *Science*, *303*, 978, doi:10.1126/science.1091901.

Chelton, D. B., M. G. Schlax, and R. M. Samelson (2007), Summertime Coupling between Sea Surface Temperature and Wind Stress in the California Current System, Journal of Physical Oceanography, 37, 495-517, doi:10.1175/JPO3025.1.

Chelton, D. B., M. G. Schlax, and R. M. Samelson (2011b), Global observations of nonlinear mesoscale eddies, *Progress in Oceanography*, *91*, 167-216, doi:10.1016/j.pocean.2011.01.002.

Chenillat, F., P. J. S. Franks, and V. Combes (2016), Biogeochemical properties of eddies in the California Current System, *Geophysical Research Letters*, *43*, 5812-5820, doi:10.1002/2016gl068945.

Chenillat, F., P. J. S. Franks, P. Rivière, X. Capet, N. Grima, and B. Blanke (2015), Plankton dynamics in a cyclonic eddy in the Southern California Current System, *Journal of Geophysical Research: Oceans*, *120*, 5566-5588, doi:10.1002/2015JC010826.

Combes, V., F. Chenillat, E. Di Lorenzo, P. Rivière, M. D. Ohman, and S. J. Bograd (2013), Cross-shore transport variability in the California Current: Ekman upwelling vs. eddy dynamics, *Progress in Oceanography*, *109*, 78-89, doi:10.1016/j.pocean.2012.10.001.

Crawford, W. R., P. J. Brickley, and A. C. Thomas (2007), Mesoscale eddies dominate surface phytoplankton in northern Gulf of Alaska, *Progress in Oceanography*, *75*, 287-303, doi:10.1016/j.pocean.2007.08.016.

Dauhajre, D. P., J. C. McWilliams, and Y. Uchiyama (2017), Submesoscale coherent structures on the continental shelf, *Journal of Physical Oceanography*, *47*, 2949-2976, doi:10.1175/JPO-D-16-0270.1.

Doherty, M., P. L. Yager, M. A. Moran, V. J. Coles, C. S. Fortunato, A. V. Krusche, P. M. Medeiros, J. P. Payet, J. E. Richey, and B. M. Satinsky (2017), Bacterial biogeography across the Amazon River-ocean continuum, *Frontiers in Microbiology*, *8*, 882, doi:10.3389/fmicb.2017.00882.

Dong, C., J. C. McWilliams, Y. Liu, and D. Chen (2014), Global heat and salt transports by eddy movement, *Nature communications*, *5*(1), 1-6, doi:10.1038/ncomms4294.

Early, J. J., R. M. Samelson, and D. B. Chelton (2011), The Evolution and Propagation of Quasigeostrophic Ocean Eddies, *American Meteorological Society*, *41*, 1535-1555, doi:10.1175/2011JPO4601.1.

Fu, L.-L., D. Alsdorf, R. Morrow, E. Rodriguez, and N. Mognard (2012), *SWOT: the surface water and ocean topography mission: wide-swath altimetric elevation on Earth*. NASA. Retrieved from http://hdl.handle.net/2014/41996.

García-Reyes, M., and J. L. Largier (2012), Seasonality of coastal upwelling off central and northern California: New insights, including temporal and spatial variability, *Journal of Geophysical Research: Oceans*, *117*, C03028, doi:10.1029/2011jc007629.

Gaube, P., D. B. Chelton, P. G. Strutton, and M. J. Behrenfeld (2013), Satellite observations of chlorophyll, phytoplankton biomass, and Ekman pumping in nonlinear mesoscale eddies, *Journal of Geophysical Research: Oceans*, *118*, 6349-6370, doi:10.1002/2013jc009027.

Gaube, P., and D. J. McGillicuddy Jr. (2017), The influence of Gulf Stream eddies and meanders on near-surface chlorophyll, *Deep-Sea Research I*, *122*, 1-16, doi:10.1016/j.dsr.2017.02.006.

Gaube, P., D. J. McGillicuddy Jr., D. B. Chelton, M. J. Behrenfeld, and P. G. Strutton (2014), Regional variations in the influence of mesoscale eddies on near-surface chlorophyll, *Journal of Geophysical Research: Oceans*, *119*, 8195-8220, doi:10.1002/ 2014JC010111.

Haidvogel, D. B., A. Beckmann, and K. S. Hedström (1991), Dynamical simulations of filament formation and evolution in the coastal transition zone, *Journal of Geophysical Research*, *96*(C8), 15,017-015,040.

Haynes, R., and E. D. Barton (1991), Lagrangian observations in the Iberian coastal transition zone, *Journal of Geophysical Research: Oceans*, *96*(C8), 14731-14741, doi:10.1029/91JC00907.

Haynes, R., E. D. Barton, and I. Pilling (1993), Development, persistence and variability of upwelling filaments off the Atlantic coast of the Iberian Peninsula, edited, pp. 22681-22692, doi:10.1029/93JC02016.

Huyer, A. (1983), Coastal upwelling in the California Current System, *Progress in Oceanography*, *12*, 259-284, doi:10.1016/0079-6611(83)90010-1.

Kosro, P. M., and A. Huyer (1986), CTD and velocity surveys of seaward jets off northern California, July 1981 and 1982, *Journal of Geophysical Research*, *91*(C6), 7680-7690, doi:10.1029/JC091iC06p07680.

Kurian, J., F. Colas, X. Capet, J. C. McWilliams, and D. B. Chelton (2011), Eddy properties in the California Current System, *Journal of Geophysical Research*, *116*, C08027, doi:10.1029/2010jc006895.

Lehahn, Y., F. d'Ovidio, M. Lévy, Y. Amitai, and E. Heifet (2011), Long range transport of a quasi isolated chlorophyll patch by an Agulhas ring, *Geophysical Research Letters*, *38*, L16610, doi:10.1029/2011GL048588.

Liang, J. H., J. C. McWilliams, and N. Gruber (2009), High-frequency response of the ocean to mountain gap winds in the northeastern tropical Pacific, *Journal of Geophysical Research: Oceans*, *114*(C12), doi:10.1029/2009JC005370.

Lovecchio, E., N. Gruber, and M. Münnich (2018), Mesoscale contribution to the long-range offshore transport of organic carbon from the Canary Upwelling System to the open North Atlantic, *Biogeosciences*, *15*, 5061-5091, doi:10.5194/bg-15-5061-2018.

Lynn, R. J., and J. J. Simpson (1987), The California Current System: The Seasonal Variability of its Physical Characteristics, *Journal of Geophysical Research*, *92*(C12), 12947-12966, doi:10.1029/JC092iC12p12947.

McWilliams, J. C. (2016), Submesoscale currents in the ocean, *Proceedings of the Royal Society A*, *472*, 20160117, doi:10.1098/rspa.2016.0117.

Medeiros, P. M., M. Seidel, N. D. Ward, E. J. Carpenter, H. R. Gomes, J. Niggemann, A. V. Krusche, J. E. Richey, P. L. Yager, and T. Dittmar (2015), Fate of the Amazon River dissolved organic matter in the tropical Atlantic Ocean, *Global Biogeochemical Cycles*, *29*(5), 677-690, doi:10.1002/2015GB005115.

Medeiros, P. M., E. L. Sikes, B. Thomas, and K. H. Freeman (2012), Flow discharge influences on input and transport of particulate and sedimentary organic carbon along a small temperate river, *Geochimica et Cosmochimica Acta*, *77*, 317-334, doi:10.1016/j.gca.2011.11.020.

Mesias, J. M., R. P. Matano, and P. T. Strub (2003), Dynamical analysis of the upwelling circulation off central Chile, *Journal of Geophysical Research: Oceans*, *108*(C3), doi:10.1029/2001JC001135.

Meunier, T., E. D. Barton, B. Barreiro, and R. Torres (2012), Upwelling filaments off Cap Blanc: Interaction of the NW African upwelling current and the Cape Verde frontal zone eddy field?, *Journal of Geophysical Research: Oceans*, *117*(C8), doi:10.1029/2012JC007905.

Mooers, C. N. K., and A. R. Robinson (1984), Turbulent jets and eddies in the California Current and inferred cross-shore transports, *Science*, *223*(4631), 51-53, doi:10.1126/science.223.4631.51.

Nagai, T., N. Gruber, H. Frenzel, Z. Lachkar, J. C. McWilliams, and G.-K. Plattner (2015), Dominant role of eddies and filaments in the offshore transport of carbon and nutrients in the California Current System, *Journal of Geophysical Research: Oceans*, *120*, 5318-5341, doi:10.1002/2015jc010889.

Pegliasco, C., A. Chaigneau, and R. Morrow (2015), Main eddy vertical structures observed in the four major Eastern Boundary Upwelling Systems, *Journal of Geophysical Research: Oceans*, *120*, 6008-6033, doi:10.1002/2015jc010950.

Peliz, Á., T. L. Rosa, A. M. P. Santos, and J. L. Pissarra (2002), Fronts, jets, and counter-flows in the Western Iberian upwelling system, *Journal of marine systems*, *35*(1-2), 61-77, doi:10.1016/S0924-7963(02)00076-3.

Penven, P., C. Roy, A. Colin de Verdière, and J. Largier (2000), Simulation of a coastal jet retention process using a barotropic model, edited, pp. 615-634, doi:10.1016/S0399-1784(00)01106-3.

Putrasahan, D. A., A. J. Miller, and H. Seo (2013), Regional coupled ocean–atmosphere downscaling in the Southeast Pacific: impacts on upwelling, mesoscale air–sea fluxes, and ocean eddies, Ocean Dynamics, 63(5), 463-488, doi:10.1007/s10236-013-0608-2.

Ramp, S. R., P. F. Jessen, K. H. Brink, P. P. Niiler, F. L. Daggett, and J. S. Best (1991), The physical structure of cold filaments near Point Arena, California, during June 1987, *Journal of Geophysical Research: Oceans*, *96*(C8), 14859-14883, doi:10.1029/91JC01141.

Relvas, P., and E. D. Barton (2002), Mesoscale patterns in the Cape Sao Vicente (Iberian peninsula) upwelling region, *Journal of Geophysical Research: Oceans*, *107*(C10), 28-21-28-23, doi:10.1029/2000JC000456.

Røed, L. P., and X. B. Shi (1999), A numerical study of the dynamics and energetics of cool filaments, jets, and eddies off the Iberian Peninsula, *Journal of Geophysical Research: Oceans*, *104*(C12), 29817-29841, doi:10.1029/1999JC900175.

Sangrà, P., et al. (2009), The Canary Eddy Corridor: A major pathway for long-lived eddies in the subtropical North Atlantic, *Deep-Sea Research I*, *56*(12), 2100-2114, doi:10.1016/j.dsr.2009.08.008.

Satinsky, B. M., B. C. Crump, C. B. Smith, S. Sharma, B. L. Zielinski, M. Doherty, J. Meng, S. Sun, P. M. Medeiros, and J. H. Paul (2014), Microspatial gene expression patterns in the Amazon River Plume, *Proceedings of the National Academy of Sciences*, *111*(30), 11085-11090, doi:10.1073/pnas.1402782111.

Schlax, M. G., and D. B. Chelton (2016), *The "growing method" of eddy identification and tracking in two and three dimensions*. Corvallis, OR: College of Earth, Ocean and Atmospheric Sciences, Oregon State University. Retrieved from http://wombat.coas.oregonstate.edu/eddies/Growing_Method_of_Eddy_Identification_and_Tracking.pdf.

Stramski, D., et al. (2008), Relationships between the surface concentration of particulate organic carbon and optical properties in the eastern South Pacific and eastern Atlantic Oceans, *Biogeosciences*, *5*, 171-201, doi:10.5194/bg-5-171-2008.

Strub, P. T., V. Combes, F. A. Shillington, and O. Pizarro (2013), Currents and Processes along the Eastern Boundaries, in *Ocean Circulation and Climate: A 21st Century*

Perspective, edited by G. Siedler, S. M. Griffies, J. Gould and J. A. Church, pp. 339-384, Academic Press, doi:10.1016/b978-0-12-391851-2.00014-3.

Strub, P. T., and C. James (2000), Altimeter-derived variability of surface velocities in the California Current System: 2. Seasonal circulation and eddy statistics, *Deep-Sea Research II*, *47*, 831-870, doi:10.1016/S0967-0645(99)00129-0.

Strub, P. T., C. James, V. Montecino, J. A. Rutllant, and J. L. Blanco (2019), Ocean circulation along the southern Chile transition region (38–46 S): Mean, seasonal and interannual variability, with a focus on 2014–2016, Progress in oceanography, 172, 159-198, doi:10.1016/j.pocean.2019.01.004.

Strub, P. T., P. M. Kosro, and A. Huyer (1991), The Nature of the Cold Filaments in the California Current System, *Journal of Geophysical Research*, *96*, 14,743-714,768.

Veitch, J., J. Hermes, T. Lamont, P. Penven, and F. Dufois (2018), Shelf-edge jet currents in the southern Benguela: A modelling approach, *Journal of Marine Systems*, *188*, 27-38, doi:10.1016/j.jmarsys.2017.09.003.

Wang, Y., R. M. Castelao, and Y. Yuan (2015), Seasonal variability of alongshore winds and sea surface temperature fronts in Eastern Boundary Current Systems, *Journal of Geophysical Research: Oceans*, *120*, 2385-2400, doi:10.1002/2014jc010379.

Yuan, Y., and R. M. Castelao (2017), Eddy-induced sea surface temperature gradients in Eastern Boundary Current Systems, *Journal of Geophysical Research: Oceans*, *122*, 4791-4801, doi:10.1002/2017JC012735.

Table 3.1. Eddies characteristics and transport estimates in each EBCS subregion. The number of eddies per year, annual volume transport, and offshore POC enrichment were only calculated for cyclonic eddies generated 0-300 km from the coast that propagated offshore of 300 km. The calculation for offshore POC enrichment only includes amplitudes bins with POC anomalies that are statistically different (t-test, $p < 0.1$; see Figure 3.5 for significant bins). Subregions without a POC enrichment means that none of the amplitude bins were statistically different. The nonlinearity parameter was only calculated for cyclonic eddies located 0-300 km from the coast. Abnormally high nonlinear values associated with the tracking algorithm were excluded from the calculations by removing data above the 90th percentile.

	Subregions (number and latitude range)		Number of cyclonic eddies per year (mean ± one standard error)	Annual volume transport by cyclonic eddies ± one standard error (Sv)	Offshore POC enrichment by cyclonic eddies ± one standard error (Gg year^{-1})	Nonlinearity parameter for cyclonic eddies (mean ± one standard deviation)	Percentage of cyclonic eddies that are nonlinear (U/c>1)
California Current System	1	43-47°N	1.4 ± 0.4	0.27 ± 0.12	-	3.0 ± 2.4	80.0%
	2	37-43°N	3.6 ± 0.6	0.96 ± 0.17	22.6 ± 5.1	6.3 ± 4.8	93.0%
	3	33-37°N	2.2 ± 0.6	0.60 ± 0.14	1.1 ± 0.9	5.3 ± 4.2	91.9%
	4	28-33°N	3.2 ± 0.5	0.77 ± 0.14	-1.2 ± 2.6	5.7 ± 4.4	92.0%
	5	23-28°N	3.6 ± 0.6	0.89 ± 0.17	4.4 ± 1.2	5.4 ± 3.6	94.0%
Humboldt Current System	1	4-24°S	11.9 ± 0.5	6.25 ± 0.35	-	2.3 ± 1.5	77.8%
	2	24-34°S	7.3 ± 0.6	1.96 ± 0.16	3.8 ± 1.8	3.5 ± 2.4	88.0%
	3	34-42°S	4.1 ± 0.4	0.79 ± 0.09	16.1 ± 3.1	2.8 ± 2.4	75.3%
	4	42-56°S	5.8 ± 0.5	0.72 ± 0.06	5.7 ± 1.3	1.9 ± 1.6	61.9%
Canary Current System	1	36-44°N	3.6 ± 0.4	0.63 ± 0.08	-2.5 ± 0.7	1.9 ± 1.5	66.7%
	2	28-36°N	3.3 ± 0.5	0.77 ± 0.13	1.8 ± 0.5	3.2 ± 2.4	82.5%
	3	21-28°N	4.6 ± 0.5	1.22 ± 0.14	16.8 ± 6.1	2.3 ± 1.7	77.0%
Benguela Current System	1	23-29°S	4.1 ± 0.5	1.16 ± 0.19	-	3.1 ± 2.3	84.0%
	2	29-35°S	2.5 ± 0.6	0.56 ± 0.13	3.6 ± 3.1	7.2 ± 5.9	92.5%

Table 3.2. Results in Table 3.1 calculated per degree latitude. The number of eddies per year, annual volume transport, and offshore POC enrichment were only calculated for cyclonic eddies generated 0-300 km from the coast that propagated offshore of 300 km. The calculation for offshore POC enrichment only includes amplitudes bins with POC anomalies that are statistically different (t-test, $p < 0.1$; see Figure 3.5 for significant bins). Subregions without a POC enrichment means that none of the amplitude bins were statistically different.

	Subregions (number and latitude range)		Number of cyclonic eddies per year (mean) per degree latitude	Annual volume transport by cyclonic eddies (Sv) per degree latitude	Offshore POC enrichment by cyclonic eddies (Gg $year^{-1}$) per degree latitude
California Current System	1	43-47°N	0.35	0.07	-
	2	37-43°N	0.60	0.16	3.77
	3	33-37°N	0.55	0.15	0.28
	4	28-33°N	0.64	0.15	-0.24
	5	23-28°N	0.72	0.18	0.88
Humboldt Current System	1	4-24°S	0.60	0.31	-
	2	24-34°S	0.73	0.20	0.38
	3	34-42°S	0.51	0.10	2.01
	4	42-56°S	0.45	0.06	0.44
Canary Current System	1	36-44°N	0.45	0.08	-0.31
	2	28-36°N	0.41	0.10	0.23
	3	21-28°N	0.66	0.17	2.40
Benguela Current System	1	23-29°S	0.68	0.19	-
	2	29-35°S	0.42	0.09	0.60

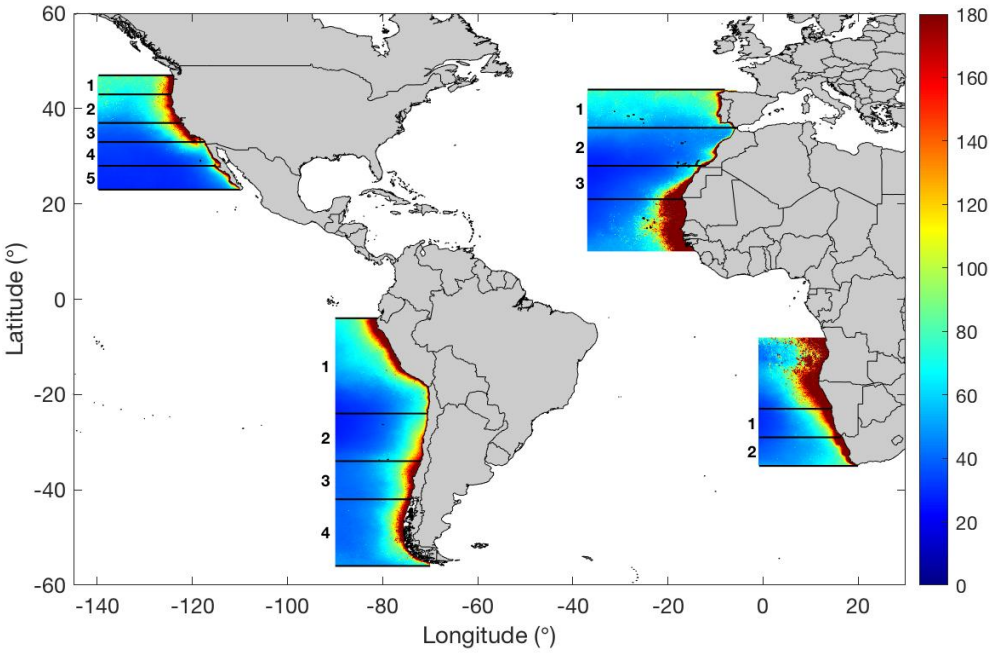

Figure 3.1. Long-term mean of POC (mg m^{-3}) for 1998-2009. POC was calculated using a relationship between blue-to-green band ratios of remote sensing reflectances from SeaWiFS (Stramski et al., 2008). Numbered subregions correspond to the subregions listed in Table 3.1.

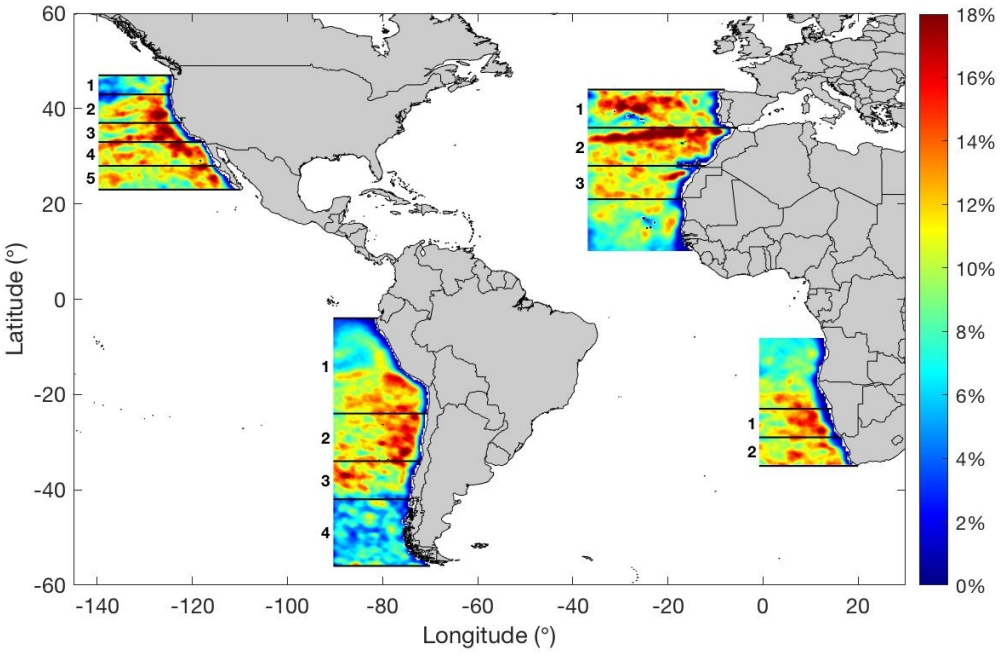

Figure 3.2. Frequency of occurrence (percentage of time that eddies are observed at a given location) for cyclonic eddies that passed through each 0.35° x 0.35° region. Numbered subregions correspond to the subregions listed in Table 3.1.

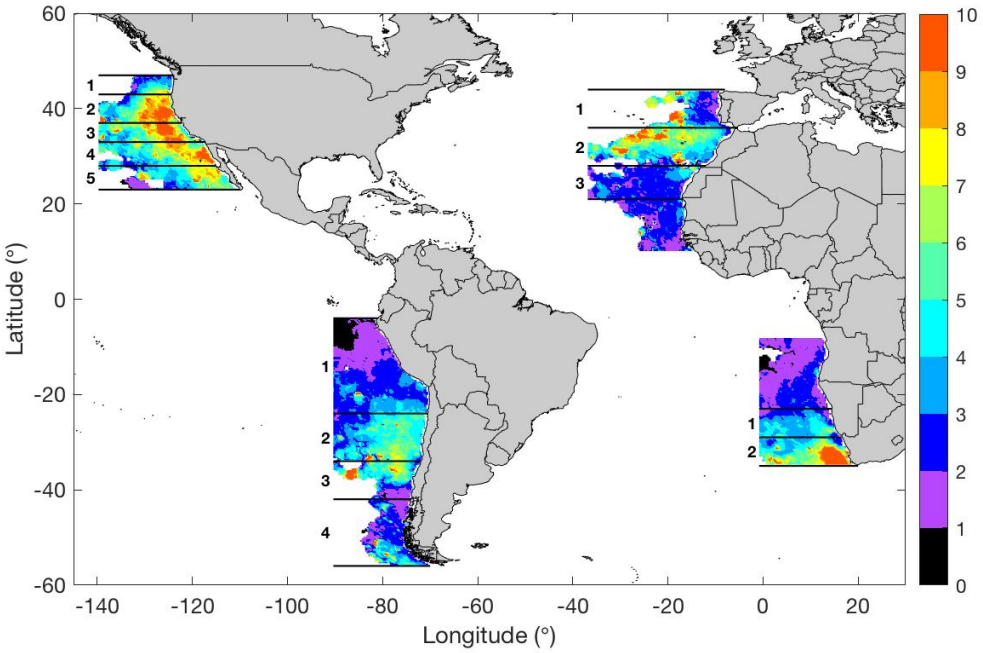

Figure 3.3. Mean nonlinearity parameter (U/c; unitless) for cyclonic eddies generated inshore of 300 km that passed through each 0.35° x 0.35° region. Numbered subregions correspond to the subregions listed in Table 3.1. No nonlinear eddies generated near the coast propagated to the areas shown in white in each of the four EBCS.

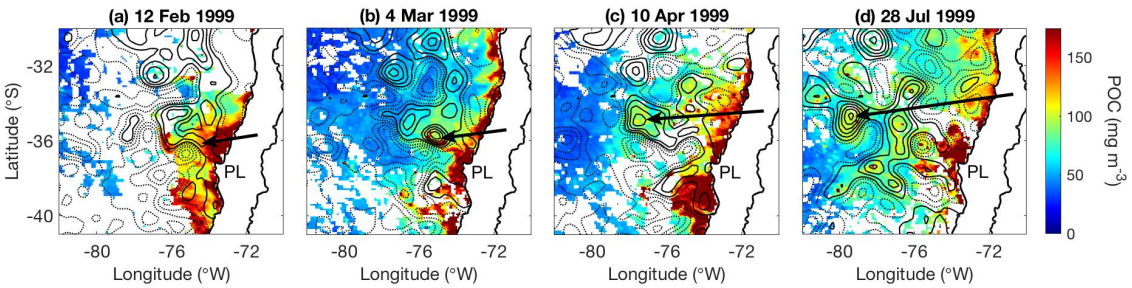

Figure 3.4. Example of offshore transport by an eddy in the Humboldt Current System. POC (mg m^{-3}) derived from satellite observations and mean sea level anomaly contours from altimetry at 3 cm intervals on (a) 12 February 1999, (b) 4 March 1999, (c) 10 April 1999, and (d) 28 July 1999. Solid contours are negative. Arrows mark the location of a cyclonic eddy transporting upwelled coastal water that is rich in POC offshore. PL: Punta Lavapie.

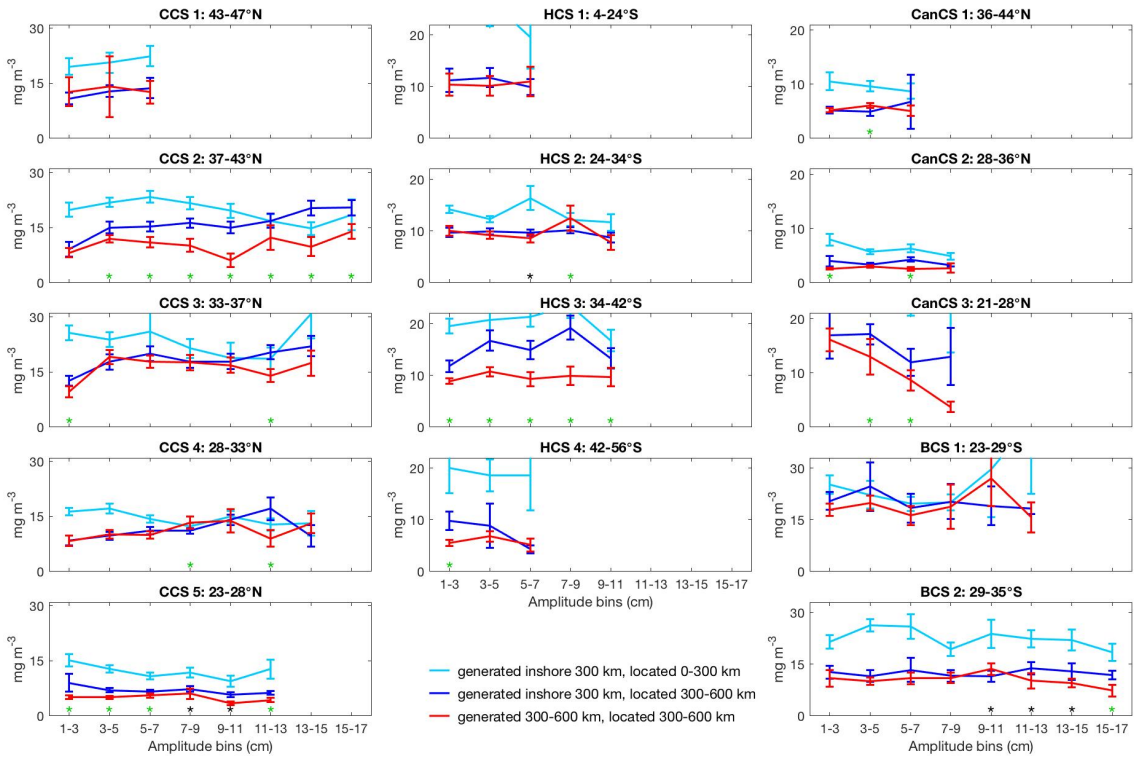

Figure 3.5. Mean POC anomaly (mg m^{-3}) within one eddy radius grouped by eddy amplitude for cyclonic eddies in each subregion in the CCS (left), HCS (middle), CanCS (top right), and BCS (bottom right). Error bars show the 95% confidence intervals. The cyan line is for cyclones generated and located 0-300 km from the coast. The dark blue line is for cyclones generated 0-300 km from the coast that propagated to 300-600 km offshore. The red line is for cyclones generated and located offshore between 300-600 km. The asterisks at the bottom of each plot indicate the amplitude bins where the dark blue and red lines are statistically different (t-test, green is for $p < 0.05$ and black is for $p < 0.1$). Only amplitude bins with more than 10 eddy occurrences for each group of eddies are included in the analyses and shown in the plots. The y-axis is cropped on all plots so that the same limit is used for each EBCS and to make it easier to compare the various subregions within an EBCS.

CHAPTER 4

INFLUENCE OF THE EL NIÑO-SOUTHERN OSCILLATION ON SST FRONTS ALONG THE WEST COASTS OF NORTH AND SOUTH AMERICA [3]

[3] Amos, C.M. and R.M. Castelao. Submitted to *Journal of Geophysical Research: Oceans.*

4.1. Abstract

Along the west coasts of North and South America, sea surface temperature (SST) fronts are important for circulation dynamics and promoting biological activity. Prevailing equatorward winds during local summer results in offshore Ekman transport and upwelling along the coast, where fronts often form between the cold, upwelled water and the warmer offshore waters. Although the interannual variability in winds, coastal upwelling, sea level anomalies, and SST in these regions have been linked to the El Niño-Southern Oscillation (ENSO), SST fronts have received less attention. Here, we use satellite SST data spanning 1982-2018 to show that frontal activity within 0-300 km offshore decreases during El Niño events and increases during La Niña events along most of the west coasts of North and South America. After removing the seasonal cycle, the variability in frontal activity is dominated by ENSO. The decrease in frontal activity off South America during El Niño coincides with the seasonal peak in frontal activity, while off North America the decrease occurs when frontal activity is at a seasonal minimum. We utilized satellite measurements of wind stress and sea level anomaly to investigate how oceanic and atmospheric forcing mechanisms associated with ENSO affect frontal activity. Off Central and South America, oceanic forcing (i.e., coastal Kelvin waves) is likely the main contributor to the decrease in frontal activity during El Niño events. Along the west coast of the United States, the decrease in frontal activity is likely due to both oceanic forcing and atmospheric teleconnections associated with ENSO.

4.2. Introduction

The physical, chemical, and biological processes in Eastern Boundary Current Systems (EBCS) have been widely studied over the past several decades. EBCS are associated with large-scale anticyclonic flow, and with coastlines generally aligned in the meridional direction, these regions are favorable for coastal upwelling (Bakun and Nelson, 1991). Prevailing equatorward winds during the summer result in offshore Ekman transport and upwelling along the coast, bringing cold, nutrient-rich waters to the surface (Huyer, 1983). The circulation often establishes sea surface temperature (SST) fronts that separate the cold, upwelled water along the coast from warmer offshore waters (Kostianoy and Lutjeharms, 1999). A strong alongshore coastal upwelling jet also forms in geostrophic balance with the upwelled isopycnals (Huyer, 1983), making the locations of SST fronts good proxies for the location of flow intensifications in these regions (Strub and James, 2000). Fronts are also characterized by convergent flow at the surface, making them hotspots for biological activity. As free-floating biota accumulate in the frontal zone, higher trophic levels are attracted to these regions, establishing productive food webs (Walsh, 1977; Bowman, 1978; Chavez and Messié, 2009; Woodson and Litvin, 2015).

SST fronts in EBCS have received a great deal of attention over the past two decades (e.g., Castelao et al., 2006; Meunier et al., 2012; Nieto et al., 2012; Santos et al., 2012; Vazquez-Cuervo et al., 2013; Wang et al., 2015; Veitch and Penven, 2017; Oerder et al., 2018; Mauzole et al., 2020). In the two EBCS in the Pacific Ocean, located along the west coasts of the United States and Mexico and along Peru and Chile, fronts have been shown to exhibit latitudinal and seasonal variability, largely due to the seasonality

of upwelling (Strub et al., 1998; Kahru et al., 2012; Vazquez-Cuervo et al., 2013; Castelao and Wang, 2014; Wang et al., 2015) and mesoscale dynamics (Kahru et al., 2012; Vazquez-Cuervo et al., 2013; Yuan and Castelao, 2017) in these regions. Interactions of the flow with bottom topography have also been shown to influence the distribution of SST fronts in many regions, such as in the California Current System (CCS; Castelao et al., 2005).

Along the west coasts of North and South America, variability in wind patterns, upwelling, sea level anomaly (SLA), and SST anomalies have been linked to climatic indices, such as the El Niño-Southern Oscillation (ENSO) and the Pacific Decadal Oscillation (e.g., Enfield and Allen, 1980; Huyer et al., 1987; Meyers et al., 1998; Strub et al., 1998; Ulloa et al., 2001; Carr et al., 2002; Huyer et al., 2002; Schwing et al., 2002; Strub and James, 2002a; Macias et al., 2012; Jacox et al., 2014; Jacox et al., 2015; Stramma et al., 2016; Espinoza-Morriberón et al., 2017). The El Niño and La Niña phases of ENSO have widespread impacts on the ocean and atmosphere, influencing the physical processes off the coasts of North and South America. Studies have identified oceanic and atmospheric mechanisms that drive changes in these regions during El Niño events. Coastally trapped waves, originating from equatorial Kelvin waves, propagate poleward along the west coasts of North and South America, depressing the thermocline and altering oceanic processes (Enfield and Allen, 1980; Chelton and Davis, 1982; Spillane et al., 1987; Shaffer et al., 1997; Meyers et al., 1998; Strub and James, 2002a). In the CCS (30°-50°N), atmospheric teleconnections cause a decrease in the equatorward winds due to the expansion and displacement of the Aleutian Low to the southeast, affecting upwelling in this region (Alexander et al., 2002; Schwing et al., 2002). Off the

coasts of Peru and Chile, alongshore winds are affected through different atmospheric teleconnections, which have been shown to maintain or increase upwelling favorable winds during El Niño events (Huyer et al., 1991; Blanco et al., 2002; Carr et al., 2002; Kessler, 2006).

Although a clear link has been identified between ENSO events and winds, coastal upwelling, thermocline depth, and SST anomalies along the west coasts of North and South America, the role that ENSO plays in the interannual variability of SST fronts has received less attention (Kahru et al., 2018; Wang et al., 2021). Here, we use 37 years of satellite SST data to detect fronts using an edge-detection algorithm to investigate the interannual variability of SST fronts off the west coasts of North and South America. We use satellite measurements of SLA and wind stress to investigate the oceanic and atmospheric forcing mechanisms associated with ENSO and their effects on frontal variability.

4.3. Data and Methods

4.3.1. SST Fronts

Daily sea surface temperature (SST) measurements from January 1982 to December 2018 were obtained from the Group for High Resolution Sea Surface Temperature (GHRSST). The global level 4 SST product provided by GHRSST is produced on a 0.25 degree grid by optimally interpolating SST observations from satellite (AVHRR only) and in situ platforms (i.e. ships and buoys). SST fronts are identified off the west coasts of North and South America using an edge-detection algorithm (Canny, 1986) following Castelao et al. (2006) and Wang et al. (2015) (Figure 4.1). Briefly, we

first compute the SST gradient vector for each daily SST map. The thresholding in the edge-detection algorithm is done with hysteresis. The algorithm first looks for pixels with gradient magnitude larger than a threshold T_1. These pixels are flagged as frontal pixels. The algorithm then tracks along a front crest flagging individual pixels as fronts until the gradient magnitude falls below a smaller threshold T_2. This helps to ensure that noisy edges are not broken up into multiple edge fragments. The thresholds employed for T_1 and T_2 are 0.017°C km^{-1} and 0.0085°C km^{-1}, respectively. Comparisons of fronts detected with gradient magnitude maps show that the chosen threshold values allow for capturing most of the main fronts in the domain (Figure 4.1). Additional details about the front detection method can be found in Castelao et al. (2006). Monthly frontal probabilities are calculated from the daily maps of fronts by taking the number of times each pixel qualifies as a front during one month and dividing by the number of times the pixel was valid (e.g., cloud free) during that month (Ullman and Cornillon, 1999; Mavor and Bisagni, 2001). GHRSST AVHRR-only SST is cloud free due to the optimal interpolation of SST from different sources, however computing frontal probabilities allows for comparisons with other studies and with analyses using MODIS SST, which are described below.

One potential concern with using the GHRSST AVHRR-only SST product is that it is characterized by a lower feature resolution compared to other SST products, such as MODIS. We repeated the analyses using daily MODIS SST measurements that are available at 4 km resolution from July 2002 to December 2018. Despite the higher spatial resolution of MODIS SST, its shorter temporal coverage is a disadvantage for studying the interannual variability of SST fronts in relation to ENSO. Analyses of fronts using

GHRSST AVHRR-only SST were consistent with the spatial and temporal patterns of fronts detected using MODIS. A regression analysis comparing SST gradient magnitudes (which are used to detect fronts) between the two products in the Northern Hemisphere at monthly time scales indicates that the magnitude of gradients computed using GHRSST are on average 30% less than the magnitude of MODIS gradients, with the intercept centered around zero. Gradient magnitudes computed using the two products are significantly correlated to each other, with an average correlation along the coastline of 0.75.

4.3.2. Wind Stress

The Cross-Calibrated Multi-Platform (CCMP) version 2.0 gridded surface vector winds from July 1987 to December 2018 are used to compute wind stress. Four daily maps of CCMP vector winds are produced on a 0.25 degree grid using a combination of Version-7 RRS radiometer wind speeds, QuikSCAT and ASCAT scatterometer wind vectors, moored buoy wind data, and ERA-Interim model wind fields using a Variational Analysis Method (Atlas et al., 2010). We computed wind stress for each of the four daily maps, then averaged the four maps to produce a daily map of wind stress. The alongshore component of the wind stress was computed by rotating the coordinate system to be parallel with the local coastline. Although this product is somewhat smoothed compared to satellite wind fields (e.g., QuikSCAT, ASCAT), it has the advantage of covering a substantially longer period of time, allowing for comparisons with the GHRSST AVHRR-only SST record.

4.3.3. Sea Level Anomaly

Sea level anomaly (SLA) data are obtained from the Copernicus Climate Service. SLA is available daily from January 1993 to December 2018 on a 0.25 degree grid.

4.3.4. El Niño and La Niña Events

We use the Oceanic Niño Index (ONI) produced by NOAA to define El Niño and La Niña events (Figure 4.2). The ONI is defined as the three-month running mean of SST anomalies in the Niño 3.4 region. El Niño (La Niña) events occur when the ONI reaches $\geq 0.5°C$ ($\leq -0.5°C$) for a minimum of five consecutive months (NOAA Climate Prediction Center). Other indices are also used to define ENSO events using different parameters and/or regions of the equatorial Pacific. We repeated the analyses using the Multivariate ENSO Index, Niño 3.4, Niño 3, Niño 4, and the Southern Oscillation Index to see if the results hold true when ENSO events are defined differently.

4.3.5. Analysis Methods

Our analysis covers the west coasts of North and South America, spanning 7°-50°N and 0°-43°S, respectively. We divided both domains into 1° latitude boxes, extending from the coast to 300 km offshore. This offshore distance was determined based on the average offshore extent of the intensity of fronts, wind stress, and SLA in the domain. The results presented here are consistent with the results obtained when using a narrower region extending for 0-100 km and 0-200 km offshore. For each data set, monthly time series were computed by averaging the data within each box. Climatological monthly means were computed for the period 2003-2013 and subtracted

from the monthly time series within each box to compute monthly anomalies. We used 2003-2013 as the climatological mean period to exclude the major El Niño events in 1982-1983, 1997-1998, and 2015-2016. This time period is also captured by MODIS SST, allowing us to compare the anomalies of gradients and frontal probabilities from GHRSST AVHRR-only SST and MODIS SST that were computed using the same climatological mean period. To reduce noise, a 3-month running mean was applied to the monthly anomaly time series. Lagged correlations were calculated between the smoothed anomaly time series of SST frontal probability, alongshore wind stress, and SLA in each box and the ONI. To determine significant correlations, we quantified the effective number of degrees of freedom for each data set to account for autocorrelation within the time series. We computed the number of the degrees of freedom for each data set by dividing n (the number of months in the time series) by the autocorrelation time scale (5 months for frontal probability and alongshore wind stress, 6 months for SLA; Lentz, 1993). Only correlations that are significant at the 95% level are presented.

Empirical orthogonal function (EOF) decompositions are utilized to isolate the dominant modes of variability (with the seasonal cycle removed) for SST frontal probability, alongshore wind stress, and SLA. EOFs are computed using the 3-month running mean anomaly time series in the 1° latitude boxes. To determine the statistically significant EOF modes for each data set, we used the N-rule approach outlined by Overland and Preisendorfer (1982) to estimate those eigenvalues for which the geophysical signal exceeds the level of noise within the data. In both the Northern and Southern Hemisphere domains, the first 7 modes of SST frontal probability and the first 2 modes of SLA were significant. For alongshore wind stress, the first 3 modes were

significant in the Northern Hemisphere and the first 5 modes were significant in the Southern Hemisphere.

To capture the progression of SST frontal probability, alongshore wind stress, and SLA during ENSO events, monthly mean data for the 24 months covering each event (e.g., January 1997 to December 1998 to capture the 1997-1998 El Niño) were extracted from the datasets. The extracted data was averaged to compute composites for El Niño, La Niña, and neutral conditions. The composite for neutral conditions was subtracted from the El Niño and La Niña composites to capture the differences in frontal probability, alongshore wind stress, and SLA that occur during El Niño and La Niña events compared to neutral years. The composite differences were computed for weak events (defined as ONI between 0.5 and 0.99°C for El Niño and between -0.99 and -0.5°C for La Niña for at least 3 consecutive months) and moderate to strong events (defined as ONI ≥ 1°C for El Niño and ONI ≤ -1°C for La Niña for at least 3 consecutive months) to compare the response of frontal probability, alongshore wind stress, and SLA to ENSO events of different strength. A two-sample t-test was used to determine the statistically significant composite differences at the 90% and 95% levels.

4.4. Results

4.4.1. Distribution and Interannual Variability of SST Fronts

Thirty-seven years of SST data are used to detect SST fronts off the west coasts of North and South America. Consistent with Wang et al. (2015) and Wang et al. (2021), SST fronts along the west coast of North America within 0-300 km offshore are most frequently observed around 11°N and 15°N, along Baja California (21°-30°N), and in the

CCS (33°-50°N) (Figure 4.3a). Frontal activity peaks during May-October around 33°-34°N and during July-October between 37°-45°N (Figure 4.3a). The highest frontal probabilities in the CCS correspond to the locations of the strongest SST gradients, which occur near irregularities in the coastline geometry (Castelao et al., 2006; Castelao and Wang, 2014; Wang et al., 2015; Wang et al., 2021). Along Baja California, the occurrence of fronts peaks during April-June. To the south of Baja California, fronts occur in the Gulfs of Tehuantepec (15°N) and Papagayo (11°N) in boreal winter (November-March) (Figure 4.3a; referred to hereafter as "gap wind regions"). These regions are strongly influenced by intense wind jets that blow through gaps in the Sierra Madre mountain range and into the Pacific Ocean (Steenburgh et al., 1998; Chelton et al., 2000). The strong wind jets induce vertical mixing that cools the surface waters during boreal winter (Barton et al., 1993; Sun and Yu, 2006; Liang et al., 2009). SST fronts are then generated between the cold water near the coast and the surrounding warm water (Legeckis, 1988; Barton et al., 1993; Trasviña et al., 1995; Martinez-Diaz-De-Leon et al., 1999).

SST fronts occur along the entire west coast of South America within 0-300 km offshore (Figure 4.3d). Off the coast of Ecuador (0°-4°S), increased frontal activity occurs during June-November, peaking around August-September (Figure 4.3d). Along the coast of Peru between 5°-15°S, fronts occur during February-May (Figure 4.3d). To the south of 15°S, the highest frontal probabilities occur off the coast of Chile around 21°-23°S and 34°-39°S during February-May (Figure 4.3d). These spatial and temporal patterns of fronts off the west coast of South America are consistent with Wang et al. (2015) and Wang et al. (2021).

The variability in SST frontal activity that is potentially due to ENSO events is investigated using the monthly anomalies of frontal probabilities computed in 1° latitude boxes. Although the monthly anomalies still include variability on seasonal time scales, removing the seasonal cycle allows for interannual variability to be detected more easily. Along the west coast of North America, frontal activity generally decreases in boreal winter between 10°-25°N and 33°-40°N during El Niño events (Figures 4.2, 4.3b). To the north of 41°N, frontal probability decreases in boreal autumn, then increases slightly during boreal winter during El Niño events. The clearest signal in the anomalies is in the gap wind regions (11°N-15°N), where there is a reduction in frontal activity during boreal winter associated with El Niño events (Figures 4.3b, 4.4). The magnitude of the reduction in frontal probability throughout the domain appears to be related to the strength of El Niño events. The largest reductions in frontal activity occurred during 1982-1983 and 1997-1998 (Figure 4.3b), coinciding with two of the strongest El Niño events during the time period covered in this study (Figure 4.2). Another strong El Niño occurred in 2015-2016 and frontal activity was reduced to the south of 25°N, however in the CCS (33°-50°N) there was not a clear reduction in frontal activity during boreal winter (Figure 4.3b). During La Niña events, frontal activity increases in the gap wind regions (Figure 4.4), between 17°-25°N, and in the southern CCS (33°-40°N; Figure 4.3b).

Along the west coast of South America, anomalies of frontal probability are more apparent compared to those in the Northern Hemisphere (Figure 4.3e). The strongest reduction in frontal activity during El Niño events occurs between the equator and ~18°S during austral summer (Figure 4.3e). To the south of 18°S, frontal activity is also often

reduced during El Niño events, except around 23°-27°S. Consistent with the Northern Hemisphere, the magnitude of the frontal probability anomalies appears to be related to the strength of the El Niño event. An exception, however, is the 1991-1992 El Niño event. This event was weaker than the El Niño events in 1982-1983 and 1997-1998 (Figure 4.2), however the decrease in frontal probability in austral summer during 1991-1992 is comparable to the reductions in 1982-1983 and 1997-1998 (Figure 4.3e). During the 2015-2016 El Niño, frontal activity decreased less than during the events in 1982-1983 and 1997-1998, despite all three events being similar in strength based on the ONI (Figure 4.2). During La Niña events, frontal probability generally increased, however the signal was noisier compared to the anomalies observed during El Niño events (Figure 4.3e).

The monthly anomalies of SST frontal probability within 0-300 km offshore in each 1° latitude box were correlated with the ONI (Figure 4.2) at multiple lags (Figure 4.3c, f). Along the west coast of North America, anomalies are significantly negatively correlated with the ONI between 10°-25°N and between 32°-40°N (Figure 4.3c). The correlation occurs at a larger lag in the northern part of the domain compared to the southern part. The negative correlations imply a reduction in frontal activity during El Niño events (negative frontal probability anomalies and positive ONI during El Niño). The strongest correlations occur in the gap wind regions (11°-15°N) at 0 to +2 months lag (positive lag is defined as changes in frontal probability occurring after the peak in the ONI) (Figure 4.3c; see also Figure 4.4). Off the coast of South America, frontal probability anomalies are significantly negatively correlated with the ONI between the equator and 19°S and between 32°-43°S (Figure 4.3f). The strongest correlations occur

around 1°-4°S at lags of -3 to -1 months, then the correlation decreases poleward and occurs at slightly larger lags. Anomalies of SST frontal probability along both coasts were also correlated with other ENSO indices (Multivariate ENSO Index, Niño 3.4, Niño 3, Niño 4, Southern Oscillation Index) and the results were consistent with those shown here.

EOF decompositions of monthly SST frontal probability anomalies indicate that ENSO is the dominant mode of variability along the west coasts of both North and South America when the seasonal cycle is removed from the data (Figure 4.5). Notable decreases in the amplitude time series of EOF 1 in both hemispheres (Figure 4.5e) occur during El Niño events (e.g., boreal winter in 1982-1983 and 1997-1998). In the Northern Hemisphere, the amplitude time series for EOF 1 is significantly correlated with the ONI at lags of -4 to +8 months, with the peak correlation ($r = -0.65$ to -0.67) occurring at 0-2 months, which is consistent with the results in Figure 4.3. We note that although a propagating signal cannot be entirely represented by one EOF mode, frontal probability anomalies associated with ENSO last for several months (especially given that a 3-month running mean was used), allowing for the signal to be captured by the analysis. The spatial pattern and amplitude time series of EOF 1 indicate a reduction in frontal probability during El Niño events between 10°-25°N and between 30°-40°N (Figure 4.5a,e). EOF 1 accounts for a relatively small percentage of the total variance (17.8%), however it explains a larger fraction of the local variance (Chelton and Davis, 1982) in many regions (e.g., ~41% at 10°-16°N, ~30% at 17°-24°N, and ~19% at 32°-40°N; Figure 4.5b). To the north of 43°N, EOF 1 reverses sign, indicating positive anomalies of

frontal probability in boreal winter during El Niño events, as shown in Figure 4.3b. However, mode 1 only explains ~9% of the local variance in this region (Figure 4.5b).

Along the west coast of South America, EOF 1 indicates a decrease in frontal probability in austral summer during El Niño events along the entire coastline (Figure 4.5c,e). The amplitude time series for EOF 1 is significantly correlated with the ONI at lags of -4 to +4 months, with the peak correlation (r = -0.45 to -0.46) occurring at -1 to +1 months. EOF 1 explains 30.4% of the total variance in frontal probability, with the largest response occurring between 5°-17°S, where the local variance explained by EOF 1 is ~46% (Figure 4.5d). The amplitude time series of EOF 1 for frontal probability along the coast of South America captures a larger response in the reduction of frontal probability to weak El Niño events, e.g., 1987-1988 and 1991-1992, compared to North America where the time series has a smaller amplitude during those events (Figure 4.5e). Overall, EOF 1 explains more of the total variance in frontal probability and more of the local variance at 25°-35° along the west coast of South America compared to North America.

4.4.2. Alongshore Wind Stress and SLA Variability

Oceanic (e.g., poleward propagating Kelvin Wave) and atmospheric (e.g., shifts in the Aleutian Low) forcing mechanisms associated with ENSO have been shown to affect winds, upwelling, thermocline depth, and SST along the west coasts of North and South America (e.g., Enfield and Allen, 1980; Huyer et al., 1987; Strub et al., 1998; Ulloa et al., 2001; Carr et al., 2002; Huyer et al., 2002; Schwing et al., 2002; Strub and James, 2002a; Macias et al., 2012; Jacox et al., 2014; Jacox et al., 2015; Stramma et al., 2016; Espinoza-

Morriberón et al., 2017). Therefore, it is useful to investigate the variability in alongshore wind stress and SLA to understand how these forcing mechanisms may affect SST frontal activity.

Along the west coast of North America, negative alongshore wind stress (upwelling favorable in the Northern Hemisphere) within 0-300 km offshore is dominant to the north of 20°N (Figure 4.6a). Alongshore wind stress off California (34°-39°N) is upwelling favorable on a monthly time scale, with peak intensity during April to June (Figure 4.6a). To the north of 39°N, wind stress is upwelling favorable during May-September and downwelling favorable during October-March (Figure 4.6a). These patterns in the alongshore wind stress in the CCS are consistent with Huyer (1983), Strub et al. (1987), Chelton et al. (2007) and García-Reyes and Largier (2012). To the south of 20°N, cross-shore wind stress becomes more important (not shown) due to the gap wind regions where intense wind jets blow through gaps in the Sierra Madre mountain range into the Pacific Ocean around 11°N and 15°N during boreal winter (Steenburgh et al., 1998; Chelton et al., 2000). Along the west coast of South America, positive alongshore wind stress (upwelling favorable in the Southern Hemisphere) persists year-round between 0°-35°S (Figure 4.6e). Upwelling favorable winds peak during June-October to the north of 16°S along the coast of Ecuador and Peru and are continuously strong almost year-round between 28°-35°S, consistent with Putrasahan et al. (2013). To the south of ~35°S, positive wind stress occurs during October-April and switches to negative (downwelling favorable in the Southern Hemisphere) during May-September (Figure 4.6e), consistent with Strub et al. (2019).

Monthly anomalies of the alongshore wind stress within 0-300 km of the coast off of North America are most pronounced to the north of 34°N. The anomalies are generally positive in the CCS (34°-48°N) in boreal winter during El Niño events (e.g., 1997-1998 and 2002-2003; Figure 4.2, 6b), indicating more downwelling favorable or less upwelling favorable wind stress, consistent with previous studies (Schwing et al., 2002; Strub and James, 2002b). The anomalies are weaker in magnitude to the south of 34°N (Figure 4.6b), which is consistent with the spatial pattern of alongshore wind stress discussed above in which alongshore wind stress is most pronounced to the north of 34°N (Figure 4.6a). During La Niña events, anomalies in alongshore wind stress in the CCS are often weakly positive during boreal winter (Figure 4.6b). Along the west coast of South America, alongshore wind stress anomalies are weakly positive during October-May between 5°-20°S during El Niño events, with the anomalies extending farther south during some events (e.g., 1997-1998 and 2009-2010; Figure 4.2, 6d). This indicates maintained or increased upwelling favorable wind stress during El Niño events, which is consistent with previous studies (Huyer et al., 1991; Blanco et al., 2002; Carr et al., 2002). During La Niña events, anomalies in this region are quite small (Figure 4.6d). To the south of ~27°S, anomalies of alongshore wind stress are stronger in magnitude, but do not show a clear pattern associated with El Niño or La Niña events.

EOF 1 of monthly alongshore wind stress anomalies (with the seasonal cycle removed) captures the dominant mode of variability along the west coast of North America, which is likely associated with ENSO, as indicated by signals in the amplitude time series that coincide with El Niño events (Figure 4.7e). EOF 1 accounts for 61.6% of the total variance and specifically captures variability in alongshore wind stress in the

CCS (34°-50°N), where the local variance explained by EOF 1 ranges from 35% to 95% (Figure 4.7b). The amplitude time series and spatial function for EOF 1 indicate positive alongshore wind stress anomalies (more downwelling favorable or less upwelling favorable) in the CCS that peak during December-February during El Niño events (Figure 4.7a,e), which is consistent with the results in Figure 4.6b. The amplitude time series is significantly correlated with the ONI at lags of -1 to +2 months (positive lag is defined as changes in alongshore wind stress occurring after the peak in the ONI). To the south of 34°N, EOF 1 captures only ~1% of the local variance of alongshore wind stress (Figure 4.7b). EOF modes 2 and 3 explain more of the local variance in this region (not shown), however both of the amplitude time series are only significantly correlated with the ONI at large negative lags (-4 to -5 months).

Along the west coast of South America, EOF 1 captures variability in the anomalies of alongshore wind stress between 0°-17°S and between 24°-43°S (Figure 4.7c). Although EOF 1 accounts for 47.8% of the total variance and explains ~15% (0°-17°S) and 23-84% (24°-43°S) of the local variance, the amplitude time series does not show a clear pattern coinciding with El Niño and La Niña events and it is not significantly correlated with the ONI (Figure 4.7f). ENSO variability in the alongshore wind stress off the coast of South America is likely captured by EOF 2. The amplitude time series for EOF 2 is significantly correlated with the ONI at lags of -4 to +2 months, with the peak correlation ($r = -0.30$) occurring at -2 and -1 months. The spatial pattern and amplitude time series for EOF 2 indicate positive alongshore wind stress anomalies (more upwelling favorable in the Southern Hemisphere) between 0°-17°S and 23°-34°S during El Niño events, spanning austral spring and summer (Figure 4.7c,f). To the south

of 34°S, the spatial function reverses sign (Figure 4.7c), indicating negative alongshore wind stress anomalies (less upwelling favorable) during El Niño events. EOF 2 captures 24.1% of the total variance and ~22% (0°-17°S), 27-48% (23°-33°S), and ~39% (37°-43°S) of the local variance of alongshore wind stress anomalies (Figure 4.7d). The results from EOF 1 for the Northern Hemisphere and EOF 2 for the Southern Hemisphere are consistent with the Hovmöller plots of alongshore wind stress anomalies (Figure 4.6), showing that upwelling favorable wind stress generally decreases along the west coast of the United States and increases off the coast of Peru in boreal winter (austral summer) during El Niño events.

Consistent with previous studies (e.g., Enfield and Allen, 1980; Chelton and Davis, 1982; Carr et al., 2002; Strub and James, 2002a), SLA anomalies are positive within 0-300 km offshore along the west coasts of North and South America during El Niño events (Figure C.1). The positive SLA signal decreases in magnitude moving poleward along both coastlines, persisting to at least 50°N and 43°S (Figure C.1a,c). The timing of the SLA anomalies indicates poleward propagation speeds of ~80 km day^{-1} and ~200 km day^{-1} along the west coasts of North and South America, respectively, as in previous studies (Enfield and Allen, 1980; Chelton and Davis, 1982; Spillane et al., 1987; Clarke and Van Gorder, 1994; Shaffer et al., 1997). SLA anomalies were generally negative during La Niña events, however the magnitude of the anomalies was reduced compared to El Niño events (Figure C.1).

4.4.3. 2-year Progression of El Niño and La Niña events

To further capture the changes in SST frontal probability, alongshore wind stress, and SLA associated with El Niño and La Niña events compared to neutral periods, composite differences were computed using monthly mean data for the 24 months covering ENSO events (Jacox et al., 2015). Significance levels for all variables were determined using a t-test and p-value < 0.1 (Figure 4.8 and Figure 4.9). Results for all composite differences are similar using p-value < 0.05 (Figure C.2 and Figure C.3), but the spatial-temporal extent of the significant values is slightly reduced.

Significant reductions in SST frontal probability occur during moderate to strong El Niño events (defined as ONI ≥ 1°C for at least 3 consecutive months) along most of the coast between 9°-42°N (Figure 4.8a; see also Figure C.2a). In the gap wind regions (11°-15°N), frontal activity is significantly reduced during November to April, consistent with Figure 4.4. Moving poleward, the peak reduction in frontal activity occurs a bit later in the year and persists through the southern and central CCS (30°-42°N) at a slightly lower magnitude compared to the gap wind regions (Figure 4.8a). This suggests a poleward propagating signal with a speed of 75 km day^{-1} (Figure 4.8a). For weak El Niño events (defined as ONI = 0.5-0.99°C for at least 3 consecutive months), there is also a reduction in frontal probability, but the results are noisier and the signal is less defined along the coastline compared to moderate to strong events (results not shown). During moderate to strong La Niña events, significant increases in frontal probability mostly occur around 17°-25°N and 33°-38°N during boreal winter (Figure 4.9a; see also Figure C.3a). To the north of 43°N, frontal probability significantly decreases during November-December.

Along the west coast of South America, the reduction in frontal probability during moderate to strong El Niño events is largest off the coast of Ecuador and Peru, with significant reductions occurring between 0°-14°S during November-February (Figure 4.8d), consistent with Figure 4.3e. To the south of 18°S, a slight reduction in frontal activity persists to 43°S at a lower magnitude, however there are very few locations where the reduction is significant. During moderate to strong La Niña events, there is an increase in frontal activity along most of South America in austral summer and autumn, however there are few locations where the increase is significant (Figure 4.9d).

Consistent with the results presented above (Figure 4.6b), differences in alongshore wind stress during moderate to strong El Niño events compared to neutral periods are most pronounced to the north of 35°N in the CCS (Figure 4.8b). Positive differences in alongshore wind stress, indicating more downwelling favorable in the Northern Hemisphere (or less upwelling favorable), occur to the north of 35°N during November-April, with significant differences occurring in January (Figure 4.8b). Differences are weak and not significant to the south of 35°N. For moderate to strong La Niña events, differences in alongshore wind stress are also slightly positive to the north of 35°N during September-April, but weaker in magnitude compared to the El Niño events (Figure 4.9b). Along the west coast of South America, the changes in alongshore wind stress are lower in magnitude for moderate to strong El Niño events compared to North America (Figure 4.8e). During El Niño events, significant alongshore wind stress differences are weakly positive (more upwelling favorable in the Southern Hemisphere) primarily between 0°-24°S during November-March (Figure 4.8e). For moderate to

strong La Niña events, differences are low in magnitude and most values are not significant (Figure 4.9e).

There is a clear increase in SLA along the west coasts of North and South America during moderate to strong El Niño events compared to neutral periods (Figure 4.8c,f). In the Northern Hemisphere, the increase in SLA associated with El Niño events is significant along most of the coastline, with the largest increase occurring to the south of ~22°N, peaking in magnitude during November-December (Figure 4.8c). The SLA signal persists to 50°N but gradually loses strength and slightly lags behind the signal to the south. This indicates a poleward propagating signal with a speed of 74 km day^{-1} that is consistent with previous studies (Enfield and Allen, 1980; Chelton and Davis, 1982; Clarke and Van Gorder, 1994). Note that this propagation speed is almost identical to the propagation speed identified previously based on the SST frontal probability data (Figure 4.8a). To the south of the equator, the increase in SLA is also significant along most of the coastline (Figure 4.8f). The largest increase occurs between 0°-10°S during November-December and quickly decreases in magnitude to the south of 10°S. The SLA signal along the west coast of South America travels much faster than the signal along the coast of North America, at a speed of ~205 km day^{-1} (Spillane et al., 1987; Shaffer et al., 1997). During moderate to strong La Niña events, SLA decreases along the west coast of North America during boreal autumn and winter (Figure 4.9c). Along the west coast of South America, SLA also decreases during La Niña events, primarily to the north of ~20°S in austral summer (Figure 4.9f). Along the coast in both hemispheres, the magnitude of the SLA differences are smaller than the increases observed during El Niño events and there are fewer significant values.

4.5. Discussion and Conclusions

The El Niño-Southern Oscillation can have widespread impacts on the ocean and atmosphere, influencing physical and biological processes. Over the past several decades, studies have identified oceanic and atmospheric forcing mechanisms associated with ENSO that drive changes in winds, coastal upwelling, thermocline depth, and SST along the west coasts of North and South America (e.g., Enfield and Allen, 1980; Huyer et al., 1987; Meyers et al., 1998; Strub et al., 1998; Ulloa et al., 2001; Carr et al., 2002; Huyer et al., 2002; Schwing et al., 2002; Strub and James, 2002a; Macias et al., 2012; Jacox et al., 2014; Jacox et al., 2015; Stramma et al., 2016; Espinoza-Morriberón et al., 2017). Here, we investigated the influence of ENSO specifically on SST fronts in these regions. After removing the seasonal cycle, the variability in frontal activity is dominated by ENSO in both hemispheres as shown by the EOF decompositions (Figure 4.5). SST frontal activity generally decreases during boreal winter and early spring (austral summer and early autumn) during El Niño events and increases during La Niña events, with the magnitude of the anomalies generally following the strength of the events (Figures 4.3, 4.5, 4.8, 4.9).

Recent studies investigated the variability of SST fronts along the coast of Baja California to the southern CCS (Kahru et al., 2018) and along the entire west coasts of North and South America (Wang et al., 2021). Kahru et al. (2018) used MODIS and VIIRS satellite data spanning 2000-2017 to detect SST fronts between ~22°-38°N. They were primarily focused on the response of fronts to the marine heatwave event in the northeast Pacific Ocean during 2014-2015 (Gentemann et al., 2017) and to the 2015-2016 El Niño. Our results are generally consistent with Kahru et al. (2018) for the 2015-2016

El Niño, showing a slight reduction in SST frontal probability in part of the region between 22°-38°N (see Figure 4.6 in Kahru et al., 2018). Wang et al. (2021) used MODIS SST spanning 2002-2017 to detect SST fronts along the west coasts of North and South America, similar to this study, but they largely focused on frontal variability associated with ENSO in the tropical Pacific, rather than at higher latitudes as done here. Our results are consistent with Wang et al. (2021) in the gap wind regions (11°-15°N; regions 3-4 in Wang et al., 2021), showing a decrease in frontal probability during El Niño events and an increase during La Niña events. Both of these studies use satellite SST datasets that only captured variability in SST fronts since the early 2000s, which misses the strong El Niño events in 1982-1983 and 1997-1998. Our analysis expands on both of these studies by using a longer time period of satellite SST data (1982-2018) to include more ENSO events, allowing us to capture the variability of fronts in response to numerous El Niño events of varying strength.

As discussed, frontal activity generally decreases during El Niño events along most of the west coasts of North and South America. An exception to this is in the middle of both domains, between 25°-32°N and 19°-32°S, where frontal activity is not significantly correlated with the ONI. Another difference is observed during the 2015-2016 El Niño. This event became the strongest El Niño since the 1997-1998 event based on SST anomalies in the equatorial Pacific (Figure 4.2), however the reduction in frontal probability was smaller than expected given the strength of the event and the response of fronts observed during the strong events in 1982-1983 and 1997-1998 (Figures 4.3-4.5). Monthly anomalies of SLA indicated that the maximum anomalous SLA values at lower latitudes were reduced by about 19% off Central America and southern Mexico (7°-

18°N), by 41% off Ecuador and northern Peru (0-10°S), and by 19% between 11°-20°S during the 2015-2016 El Niño compared to the 1997-1998 event. Strub et al. (2019) also calculated a reduction in maximum SLA anomalies at lower latitudes along South America by approximately half in 2015 compared to 1997. In the lower latitude regions, where atmospheric forcing is weak compared to higher latitudes, the smaller response of frontal probability to the 2015-2016 El Niño may be due to weaker oceanic forcing (e.g., less depression of the thermocline) that occurred during this event. In the CCS, the thermocline was shallower than what was observed during the 1982-1983 and 1997-1998 El Niño events and there was less weakening of upwelling favorable winds (Figure 4.6; Jacox et al., 2016). There was also a marine heatwave in the northeast Pacific Ocean during 2014-2016 that caused unusually warm SST anomalies and other impacts in the CCS (Gentemann et al., 2017). The lack of a clear signal in the reduction in frontal probability off the west coast of the United States during the 2015-2016 El Niño may be due to a combination of changes in both oceanic and atmospheric conditions that differed from the other strong El Niño events.

The ENSO-related forcing mechanisms likely affect frontal activity along the west coasts of North and South America through atmospheric and oceanic pathways. Off the west coast of the United States, alongshore wind stress becomes more downwelling favorable during boreal winter to the north of 35°N during El Niño events (Figure 4.8). These anomalies are consistent with atmospheric teleconnections during El Niño events that strengthen and extend the Aleutian low to the southeast, causing equatorward winds (upwelling favorable) to weaken and shift to poleward winds in the CCS (Alexander et al., 2002; Schwing et al., 2002). More downwelling favorable (or less upwelling

favorable) wind stress can reduce upwelling, decreasing the surface temperature gradient and inhibiting the formation of SST fronts. SST frontal probability decreased in the CCS in boreal winter during El Niño events, coinciding with the increase in downwelling favorable wind stress. Alongshore winds along the coast of South America to the north of 33°S remained upwelling favorable in austral summer during El Niño events. This is consistent with previous studies showing that ENSO-related atmospheric forcing often causes alongshore winds to remain upwelling favorable during El Niño events along the coasts of Peru and Chile (Huyer et al., 1991; Blanco et al., 2002; Carr et al., 2002; Kessler, 2006). Despite persistent upwelling favorable winds in austral summer during El Niño events, frontal probability decreased during this time. This suggests that other ENSO forcing mechanisms are responsible for the reduction in frontal activity off South America (see discussion below).

Frontal activity may also be influenced by ENSO-related oceanic forcing. During El Niño events, coastal Kelvin waves that propagate poleward along the west coasts of North and South America are generated (Enfield and Allen, 1980; Chelton and Davis, 1982; Spillane et al., 1987; Shaffer et al., 1997; Meyers et al., 1998; Strub and James, 2002a). As these waves propagate poleward, the thermocline deepens along the coast (Huyer et al., 1987; Blanco et al., 2002; Chavez et al., 2002; Frischknecht et al., 2015) and SLA becomes positive (Enfield and Allen, 1980; Chelton and Davis, 1982; Spillane et al., 1987; Shaffer et al., 1997; Meyers et al., 1998; Strub and James, 2002a). This is accompanied by a decrease in frontal probability, suggesting a possible connection to ENSO-related oceanic forcing along both coastlines.

Given the spatial patterns of wind stress and SLA anomalies that occur along the west coasts of North and South America during El Niño events, the ENSO-related atmospheric and oceanic forcing mechanisms likely contribute differently to the observed decrease in frontal activity in different regions along the coasts. The largest SLA signals during El Niño events occurs at lower latitudes in both hemispheres, suggesting oceanic forcing (i.e., coastal Kelvin waves) likely has a larger influence on frontal activity in these regions compared to higher latitudes. In the gap wind regions (11°N-15°N; Figure 4.4), where winds blowing offshore dominate in boreal winter, Romero-Centeno et al. (2003) and Karnauskas et al. (2008) showed that these winds increase during El Niño events. Presumably, this increase in the offshore-directed wind stress would increase the vertical mixing that causes the localized cooling of the surface waters (Barton et al., 1993; Sun and Yu, 2006; Liang et al., 2009) and the formation of fronts (Legeckis, 1988; Barton et al., 1993; Trasviña et al., 1995; Martinez-Diaz-De-Leon et al., 1999), resulting in an increase in frontal activity. However, frontal activity actually decreased in these regions during El Niño events (Figure 4.4), at a time when SLA anomalies were positive. Alexander et al. (2012) showed that ENSO-driven warming in the gap wind regions was associated with deepening of the thermocline due to coastal Kelvin waves, rather than atmospheric anomalies. Farther south along the west coast of South America between 5°-33°S, alongshore wind stress remains upwelling favorable during El Niño events, yet frontal probability decreases. The decrease in frontal probability coincides with positive SLA anomalies along the coast of South America. Therefore, the influence of ENSO-related oceanic forcing likely outweighs the effects of atmospheric forcing on frontal activity in the gap wind regions and at low- to mid-latitudes regions off South America.

In the CCS (35°-50°N), where alongshore wind stress anomalies are strong but the coastal Kelvin wave signal persists, it is difficult to identify which forcing mechanism (atmospheric or oceanic) has a larger influence on the reduction in front activity based on observations alone. Future studies using idealized model simulations where forcing is systematically varied could help disentangle the contribution of different forcing mechanisms associated with ENSO on frontal variability in the region.

It is important to note the timing of the reduction in frontal activity during El Niño events in relation to the timing of peak frontal activity. Along the west coast of South America to the south of 5°S and along the coast of Central America and southern Mexico (7°-20°N), the decrease in frontal probability in austral summer (boreal winter) during El Niño events occurs when frontal activity is highest in these regions. This also aligns with the timing of peak El Niño conditions in the equatorial Pacific. Along the west coast of the United States, frontal probability also decreases in boreal winter during El Niño events, but frontal activity is lowest during this time of year. This out of phase response at higher latitudes in the Northern Hemisphere between the reduction in frontal probability during El Niño events and the timing of peak frontal activity, compared to the in-phase response along South America, may contribute to EOF 1 of frontal probability anomalies explaining more of the total variance in the Southern Hemisphere than in the Northern Hemisphere.

The west coasts of North and South America feature very productive ecosystems during local summer when upwelling intensifies and frontal activity peaks (Carr, 2001; Carr and Kearns, 2003; Chavez and Messié, 2009). Fronts become hotspots for biological activity due to flow convergence that causes free-floating biota to accumulate, which

attracts higher trophic levels and establishes productive food webs (Walsh, 1977; Bowman, 1978; Chavez and Messié, 2009; Woodson and Litvin, 2015). ENSO may impact biological activity due to the reduction in fronts observed during El Niño events. This impact may be felt more along the coast of South and Central America since the largest reduction in frontal activity during El Niño occurs in austral summer when fronts are most frequently observed in those regions. Our results also suggest that ENSO may affect the strength of ocean-atmosphere interactions along the west coasts of North and South America. Air-sea heat fluxes affect stability and mixing in the lower atmosphere, causing wind stress to increase over warm water and decrease over cold water (Chelton et al., 2001; Chelton et al., 2007). In the vicinity of SST fronts, the change in wind stress as winds blow over the warm and cold sides of the fronts generates wind stress curl and divergence that are linearly related to the crosswind and downwind components of the SST gradient, respectively (Chelton et al., 2001; Chelton et al., 2007). The coupling between SST gradients and wind stress curl and divergence peaks during boreal summer off the west coast of the United States (Chelton et al., 2007; Wang and Castelao, 2016) and during boreal winter (austral summer) off Central America, Peru and Chile (Wang and Castelao, 2016). The changes in frontal activity during ENSO events may affect this coupling differently in these regions. Specifically, ENSO will presumably have a larger influence modulating air-sea coupling along the coast of Central and South America since the reduction in frontal activity during El Niño events coincides with peak frontal activity and stronger air-sea coupling. Along the west coast of the United States, on the other hand, ENSO may have less impact on air-sea coupling associated with fronts due to the

out of phase response between the reduction in frontal activity during El Niño events and the timing of peak frontal activity and stronger air-sea coupling.

Although this study advances our understanding of low-frequency variability in SST frontal activity, the use of a 37 year-long time series of satellite SST only allows for capturing a few El Niño events, and even fewer strong events. The relatively short time series also makes it difficult to identify the influence of other modes of variability, such as the Pacific Decadal Oscillation. As more data are collected and satellite time series are expanded, so will our ability to understand the relationships between SST frontal activity and climate variability.

4.6. Acknowledgements and Data

This work was supported by NASA Headquarters under the NASA Earth and Space Science Fellowship Program - Grant 80NSSC18K1342. The data used in this study are publicly available at: GHRSST AVHRR-only SST (https://podaac.jpl.nasa.gov/dataset/AVHRR_OI-NCEI-L4-GLOB-v2.0?ids=ProcessingLevel:Measurement:Collections:SpatialCoverage&values=*4*:Ocean%20Temperature:GHRSST:Global&search=GHRSST%20AVHRR), MODIS SST (https://podaac.jpl.nasa.gov/dataset/MODIS_AQUA_L3_SST_THERMAL_DAILY_4KM_DAYTIME_V2014.0?ids=ProcessingLevel:TemporalResolution:Collections:Platform&values=*3*:Daily:MODIS_L3_SST:AQUA), CCMP v2.0 surface vector winds (http://www.remss.com/measurements/ccmp/), Sea level anomaly (https://resources.marine.copernicus.eu/?option=com_csw&view=details&product_id=S

EALEVEL_GLO_PHY_CLIMATE_L4_REP_OBSERVATIONS_008_057), and the Oceanic Niño Index (https://psl.noaa.gov/data/correlation/oni.data)

References

Alexander, M. A., I. Bladé, M. Newman, J. R. Lanzante, N.-C. Lau, and J. D. Scott (2002), The atmospheric bridge: The influence of ENSO teleconnections on air-sea interaction over the global oceans, *Journal of Climate*, *15*(16), 2205-2231, doi:10.1175/1520-0442(2002)015<2205:TABTIO>2.0.CO;2.

Alexander, M. A., H. Seo, S. P. Xie, and J. D. Scott (2012), ENSO's impact on the gap wind regions of the Eastern Tropical Pacific Ocean, *Journal of Climate*, *25*, 3549-3565, doi:10.1175/JCLI-D-11-00320.1.

Atlas, R., R. N. Hoffman, J. Ardizzone, S. M. Leidner, J. C. Jusem, D. K. Smith, and D. Gombos (2010), A cross-calibrated, multiplatform ocean surface wind velocity product for meteorological and oceanographic applications, *Bulletin of the American Meteorological Society*, *92*, 157-174, doi:10.1175/2010BAMS2946.1.

Bakun, A., and C. S. Nelson (1991), The Seasonal Cycle of Wind-Stress Curl in Subtropical Eastern Boundary Current Regions, *Journal of Physical Oceanography*, *21*(12), 1815-1834, doi:10.1175/1520-0485(1991)021<1815:TSCOWS>2.0.CO;2.

Barton, E. D., M. L. Argote, J. Brown, P. M. Kosro, M. Lavin, J. M. Robles, R. L. Smith, A. Trasviña, and H. S. Velez (1993), Supersquirt: Dynamics of the Gulf of Tehuantepec, Mexico, *Oceanography*, *6*, 23-30, doi:10.5670/oceanog.1993.19.

Blanco, J. L., M. E. Carr, A. C. Thomas, and P. T. Strub (2002), Hydrographic conditions off northern Chile during the 1996–1998 La Nina and El Nino events, *Journal of Geophysical Research: Oceans*, *107*(C3), 3-1-3-19, doi:10.1029/2001JC001002.

Bowman, M. J. (1978), Oceanic fronts in coastal processes, in *Oceanic Fronts in Coastal Processes*, edited by M. Bowman and W. Esias, pp. 2-5, Springer, NY.

Canny, J. (1986), A Computational Approach to Edge Detection, *IEEE Transactions on Pattern Analysis and Machine Intelligence*, *PAMI-8*(6), 679-698, doi:10.1109/TPAMI.1986.4767851.

Carr, M.-E. (2001), Estimation of potential productivity in Eastern Boundary Currents using remote sensing, *Deep Sea Research Part II: Topical Studies in Oceanography*, *49*(1-3), 59-80, doi:10.1016/S0967-0645(01)00094-7.

Carr, M.-E., and E. J. Kearns (2003), Production regimes in four Eastern Boundary Current systems, *Deep Sea Research Part II: Topical Studies in Oceanography*, *50*(22-26), 3199-3221, doi:0.1016/j.dsr2.2003.07.015.

Carr, M. E., P. T. Strub, A. C. Thomas, and J. L. Blanco (2002), Evolution of 1996–1999 La Niña and El Niño conditions off the western coast of South America: a remote sensing perspective, *Journal of Geophysical Research: Oceans*, *107*(C12), 29-21-29-16, doi:10.1029/2001JC001183.

Castelao, R. M., J. A. Barth, and T. P. Mavor (2005), Flow-topography interactions in the northern California Current System observed from geostationary satallite data, *Geophysical Research Letters*, *32*, L24612, doi:10.1029/2005GL024401.

Castelao, R. M., T. P. Mavor, J. A. Barth, and L. C. Breaker (2006), Sea surface temperature fronts in the California Current System from geostationary satellite observations, *Journal of Geophysical Research*, *111*, C09026, doi:10.1029/2006jc003541.

Castelao, R. M., and Y. Wang (2014), Wind-driven variability in sea surface temperature front distribution in the California Current System, *Journal of Geophysical Research: Oceans*, *119*, 1861-1875, doi:10.1002/2013jc009531.

Chavez, F. P., and M. Messié (2009), A comparison of Eastern Boundary Upwelling Ecosystems, *Progress in Oceanography*, *83*, 80-96, doi:10.1016/j.pocean.2009.07.032.

Chavez, F. P., J. T. Pennington, C. G. Castro, J. P. Ryan, R. P. Michisaki, B. Schlining, P. Walz, K. R. Buck, A. McFadyen, and C. A. Collins (2002), Biological and chemical consequences of the 1997-1998 El Niño in central California waters, *Progress in Oceanography*, *54*, 205-232, doi:10.1016/S0079-6611(02)00050-2.

Chelton, D. B., and R. E. Davis (1982), Monthly Mean Sea-Level Variability Along the West Coast of North America, *Journal of Physical Oceanography*, *12*, 757-784, doi:10.1175/1520-0485(1982)012<0757:MMSLVA>2.0.CO;2.

Chelton, D. B., S. K. Esbensen, M. G. Schlax, N. Thum, and M. H. Freilich (2001), Observations of coupling between surface wind stress and sea surface temperature in the Eastern Tropical Pacific, *Journal of Climate*, *14*, 1479-1498, doi:10.1175/1520-0442(2001)014<1479:OOCBSW>2.0.CO;2.

Chelton, D. B., M. H. Freilich, and S. K. Esbensen (2000), Satellite observations of the wind jets off the Pacific coast of Central America. Part I: Case studies and statistical characteristics, *Monthly Weather Review*, *128*, 1993-2018, doi:10.1175/1520-0493(2000)128<2019:SOOTWJ>2.0.CO;2.

Chelton, D. B., M. G. Schlax, and R. M. Samelson (2007), Summertime Coupling between Sea Surface Temperature and Wind Stress in the California Current

System, *Journal of Physical Oceanography*, *37*, 495-517, doi:10.1175/JPO3025.1.

Clarke, A. J., and S. Van Gorder (1994), On ENSO Coastal Currents and Sea Levels, *Journal of Physical Oceanography*, *24*, 661-680, doi:10.1175/1520-0485(1994)024<0661:OECCAS>2.0.CO;2.

Enfield, D. B., and J. S. Allen (1980), On the Structure and Dynamics of Monthly Mean Sea Level Anomalies along the Pacific Coast of North and South America, *Journal of Physical Oceanography*, *10*, 557-578, doi:10.1175/1520-0485(1980)010<0557:OTSADO>2.0.CO;2.

Espinoza-Morriberón, D., V. Echevin, F. Colas, J. Tam, J. Ledesma, L. Vásquez, and M. Graco (2017), Impacts of El Niño events on the Peruvian upwelling system productivity, *Journal of Geophysical Research: Oceans*, *122*(7), 5423-5444, doi:10.1002/2016JC012439.

Frischknecht, M., M. Münnich, and N. Gruber (2015), Remote versus local influence of ENSO on the California Current System, *Journal of Geophysical Research: Oceans*, *120*, 1353-1374, doi:10.1002/2014JC010531.

García-Reyes, M., and J. L. Largier (2012), Seasonality of coastal upwelling off central and northern California: New insights, including temporal and spatial variability, *Journal of Geophysical Research: Oceans*, *117*, C03028, doi:10.1029/2011jc007629.

Gentemann, C. L., M. R. Fewings, and M. García-Reyes (2017), Satellite sea surface temperatures along the West Coast of the United States during the 2014-2016

northeast Pacific marine heat wave, *Geophysical Research Letters*, *44*, 312-319, doi:10.1002/2016gl071039.

Huyer, A. (1983), Coastal upwelling in the California Current System, *Progress in Oceanography*, *12*, 259-284, doi:10.1016/0079-6611(83)90010-1.

Huyer, A., M. Knoll, T. Paluszkiewicz, and R. L. Smith (1991), The Peru Undercurrent: a study in variability, *Deep Sea Research Part A. Oceanographic Research Papers*, *38*, S247-S271, doi:10.1016/S0198-0149(12)80012-4.

Huyer, A., R. L. Smith, and J. Fleischbein (2002), The coastal ocean off Oregon and northern California during the 1997-9 El Niño, *Progress in Oceanography*, *54*, 311-341, doi:10.1016/S0079-6611(02)00056-3.

Huyer, A., R. L. Smith, and T. Paluszkiewicz (1987), Coastal upwelling off Peru during normal and El Niño times, 1981–1984, *Journal of Geophysical Research: Oceans*, *92*(C13), 14297-14307, doi:10.1029/JC092iC13p14297.

Jacox, M. G., J. Fiechter, A. M. Moore, and C. A. Edwards (2015), ENSO and the California Current coastal upwelling response, *Journal of Geophysical Research: Oceans*, *120*, 1691-1702, doi:10.1002/ 2014JC010650.

Jacox, M. G., E. L. Hazen, K. D. Zaba, D. L. Rudnick, C. A. Edwards, A. M. Moore, and S. J. Bograd (2016), Impacts of the 2015–2016 El Niño on the California Current System: Early assessment and comparison to past events, *Geophysical Research Letters*, *43*, 7072-7080, doi:10.1002/ 2016GL069716.

Jacox, M. G., A. M. Moore, C. A. Edwards, and J. Fiechter (2014), Spatially resolved upwelling in the California Current System and its connections to climate

variability, *Geophysical Research Letters*, *41*, 3189-3196, doi:10.1002/2014gl059589.

Kahru, M., E. Di Lorenzo, M. Manzano-Sarabia, and B. G. Mitchell (2012), Spatial and temporal statistics of sea surface temperature and chlorophyll fronts in the California Current, *Journal of Plankton Research*, *34*(9), 749-760, doi:10.1093/plankt/fbs010.

Kahru, M., M. G. Jacox, and M. D. Ohman (2018), GCE1: Decrease in the frequency of oceanic fronts and surface chlorophyll concentration in the California Current System during the 2014-2016 northeast Pacific warm anoamlies, *Deep-Sea Research I*, *140*, 4-13, doi:10.1016/j.dsr.2018.04.007.

Karnauskas, K. B., A. J. Busalacchi, and R. Murtugudde (2008), Low-frequency variability and remote forcing of gap winds over the east Pacific warm pool, *Journal of climate*, *21*(19), 4901-4918, doi:10.1175/2008JCLI1771.1.

Kessler, W. S. (2006), The circulation of the eastern tropical Pacific: A review, *Progress in Oceanography*, *69*, 181-217, doi:10.1016/j.pocean.2006.03.009.

Kostianoy, A. G., and J. R. E. Lutjeharms (1999), Atmospheric effects in the Angola-Benguela frontal zone, *Journal of Geophysical Research: Oceans*, *104*(C9), 20963-20970, doi:10.1029/1999jc900017.

Legeckis, R. (1988), Upwelling off the Gulfs of Panama and Papagayo in the tropical Pacific during March 1985, *Journal of Geophysical Research: Oceans*, *93*(C12), 15485-15489, doi:10.1029/JC093iC12p15485.

Lentz, S. J. (1993), The accuracy of tide-gauge measurements at subtidal frequencies, *Journal of atmospheric and oceanic technology*, *10*(2), 238-245, doi:10.1175/1520-0426(1993)010<0238:TAOTGM>2.0.CO;2.

Liang, J. H., J. C. McWilliams, and N. Gruber (2009), High-frequency response of the ocean to mountain gap winds in the northeastern tropical Pacific, *Journal of Geophysical Research: Oceans*, *114*(C12), doi:10.1029/2009JC005370.

Macias, D., M. Landry, R., A. Gershunov, A. J. Miller, and P. J. S. Franks (2012), Climatic control of upwelling variability along the western North-American coast, *PloS one*, *7*(1), e30436, doi:10.1371/journal.pone.0030436.

Martinez-Diaz-De-Leon, A., I. Robinson, D. Ballestero, and E. Coen (1999), Wind driven ocean circulation features in the Gulf of Tehuantepec, Mexico, revealed by combined SAR and SST satellite sensor data, *International Journal of Remote Sensing*, *20*(8), 1661-1668, doi:10.1080/014311699212669.

Mauzole, Y., H. Torres, and L. L. Fu (2020), Patterns and Dynamics of SST Fronts in the California Current System, *Journal of Geophysical Research: Oceans*, *125*(2), e2019JC015499, doi:10.1029/2019JC015499.

Mavor, T. P., and J. J. Bisagni (2001), Seasonal variability of sea-surface temperature fronts on Georges Bank, *Deep-Sea Research II*, *48*, 215-243, doi:10.1016/S0967-0645(00)00120-X.

Meunier, T., E. D. Barton, B. Barreiro, and R. Torres (2012), Upwelling filaments off Cap Blanc: Interaction of the NW African upwelling current and the Cape Verde frontal zone eddy field?, *Journal of Geophysical Research: Oceans*, *117*(C8), doi:10.1029/2012JC007905.

Meyers, S. D., A. Melsom, G. T. Mitchum, and J. J. O'Brien (1998), Detection of the fast Kelvin wave teleconnection due to El Niño-Southern Oscillation, *Journal of Geophysical Research: Oceans*, *103*(C12), 27655-27663, doi:10.1029/98jc02402.

Nieto, K., H. Demarcq, and S. McClatchie (2012), Mesoscale frontal structures in the Canary Upwelling System: New front and filament detection algorithms applied to spatial and temporal patterns, *Remote Sensing of Environment*, *123*, 339-346, doi:10.1016/j.rse.2012.03.028.

Oerder, V., J. P. Bento, C. E. Morales, S. Hormazabal, and O. Pizarro (2018), Coastal upwelling front detection off central Chile (36.5–37 S) and spatio-temporal variability of frontal characteristics, *Remote sensing*, *10*(5), 690, doi:10.3390/rs10050690.

Overland, J. E., and R. Preisendorfer (1982), A significance test for principal components applied to a cyclone climatology, *Monthly Weather Review*, *110*(1), 1-4, doi:10.1175/1520-0493(1982)110<0001:ASTFPC>2.0.CO;2.

Putrasahan, D. A., A. J. Miller, and H. Seo (2013), Regional coupled ocean–atmosphere downscaling in the Southeast Pacific: impacts on upwelling, mesoscale air–sea fluxes, and ocean eddies, *Ocean Dynamics*, *63*(5), 463-488, doi:10.1007/s10236-013-0608-2.

Romero-Centeno, R., J. Zavala-Hidalgo, A. Gallegos, and J. J. O'Brien (2003), Isthmus of Tehuantepec wind climatology and ENSO signal, *Journal of Climate*, *16*, 2628-2639, doi:10.1175/1520-0442(2003)016<2628:IOTWCA>2.0.CO;2.

Santos, F., M. Gomez-Gesteira, M. DeCastro, and I. Alvarez (2012), Differences in coastal and oceanic SST trends due to the strengthening of coastal upwelling

along the Benguela current system, *Continental Shelf Research*, *34*, 79-86, doi:10.1016/j.csr.2011.12.004.

Schwing, F. B., T. Murphree, L. deWitt, and P. M. Green (2002), The evolution of oceanic and atmospheric anomalies in the northeast Pacific during the El Niño and La Niña events of 1995-2001, *Progress in Oceanography*, *54*, 459-491, doi:10.1016/S0079-6611(02)00064-2.

Shaffer, G., O. Pizarro, L. Djurfeldt, S. Salinas, and J. Rutllant (1997), Circulation and low-frequency variability near the Chilean coast: Remotely forced fluctuations during the 1991–92 El Nino, *Journal of Physical Oceanography*, *27*(2), 217-235, doi:10.1175/1520-0485(1997)027<0217:CALFVN>2.0.CO;2.

Spillane, M., D. Enfield, and J. Allen (1987), Intraseasonal oscillations in sea level along the west coast of the Americas, *Journal of Physical Oceanography*, *17*(3), 313-325, doi:10.1175/1520-0485(1987)017<0313:IOISLA>2.0.CO;2.

Steenburgh, W. J., D. M. Schultz, and B. A. Colle (1998), The structure and evolution of gap outflow over the Gulf of Tehuantepec, Mexico, *Monthly Weather Review*, *126*, 2673-2691, doi:10.1175/1520-0493(1998)126<2673:TSAEOG>2.0.CO;2.

Stramma, L., T. Fischer, D. S. Grundle, G. Krahmann, H. W. Bange, and C. A. Marandino (2016), Observed El Niño conditions in the eastern tropical Pacific in October 2015, *Ocean Science*, *12*, 861-873, doi:10.5194/os-12-861-2016.

Strub, P. T., J. S. Allen, A. Huyer, R. L. Smith, and R. Beardsley (1987), Seasonal cycles of currents, temperatures, winds, and sea level over the northeast Pacific continental shelf: 35 N to 48 N, *Journal of Geophysical Research: Oceans*, *92*(C2), 1507-1526, doi:10.1029/JC092iC02p01507.

Strub, P. T., and C. James (2000), Altimeter-derived variability of surface velocities in the California Current System: 2. Seasonal circulation and eddy statistics, *Deep-Sea Research II*, *47*, 831-870, doi:10.1016/S0967-0645(99)00129-0.

Strub, P. T., and C. James (2002a), The 1997–1998 oceanic El Niño signal along the southeast and northeast Pacific boundaries—an altimetric view, *Progress in Oceanography*, *54*, 439-458, doi:10.1016/S0079-6611(02)00063-0.

Strub, P. T., and C. James (2002b), Altimeter-derived surface circulation in the large-scale NE Pacific Gyres. Part 2: 1997-1998 El Niño anomalies, *Progress in Oceanography*, *53*, 185-214, doi:10.1016/S0079-6611(02)00030-7.

Strub, P. T., C. James, V. Montecino, J. A. Rutllant, and J. L. Blanco (2019), Ocean circulation along the southern Chile transition region (38–46 S): Mean, seasonal and interannual variability, with a focus on 2014–2016, *Progress in oceanography*, *172*, 159-198, doi:10.1016/j.pocean.2019.01.004.

Strub, P. T., J. M. Mesias, V. Montecino, J. Rutllant, and S. Salinas (1998), Coastal ocean circulation off western South America, in *The Sea*, edited by A. R. Robinson and K. H. Brink, pp. 273-313, John Wiley & Sons.

Sun, F., and J. Y. Yu (2006), Impacts of Central America gap winds on the SST annual cycle in the eastern Pacific warm pool, *Geophysical research letters*, *33*(6), doi:10.1029/2005GL024700.

Trasviña, A., E. Barton, J. Brown, H. Velez, P. M. Kosro, and R. L. Smith (1995), Offshore wind forcing in the Gulf of Tehuantepec, Mexico: The asymmetric circulation, *Journal of Geophysical Research: Oceans*, *100*(C10), 20649-20663, doi:10.1029/95JC01283.

Ullman, D. S., and P. C. Cornillon (1999), Satellite-derived sea surface temperature fronts on the continental shelf off the northeast U.S. coast, *Journal of Geophysical Research: Oceans*, *104*(C10), 23459-23478, doi:10.1029/1999jc900133.

Ulloa, O., R. Escribano, S. Hormazabal, R. A. Quiñones, R. R. González, and M. Ramos (2001), Evolution and biological effects of the 1997-98 El Niño in the upwelling ecosystem off northern Chile, *Geophysical Research Letters*, *28*(8), 1591-1594, doi:10.1029/2000gl011548.

Vazquez-Cuervo, J., B. Dewitte, T. M. Chin, E. M. Armstrong, S. Purca, and E. Alburqueque (2013), An analysis of SST gradients off the Peruvian Coast: The impact of going to higher resolution, *Remote Sensing of Environment*, *131*, 76-84, doi:10.1016/j.rse.2012.12.010.

Veitch, J. A., and P. Penven (2017), The role of the Agulhas in the Benguela Current system: A numerical modeling approach, *Journal of Geophysical Research: Oceans*, *122*(4), 3375-3393, doi:10.1002/2016JC012247.

Walsh, J. J. (1977), A biological sketchbook for an eastern boundary current, in *The Sea*, edited by E. D. Goldbert, I. N. McCave, J. J. O'Brien and J. H. Steele, pp. 923-968, Wiley-Interscience, Hoboken, N. J.

Wang, Y., and R. M. Castelao (2016), Variability in the coupling between sea surface temperature and wind stress in the global coastal ocean, *Continental Shelf Research*, *125*, 88-96, doi:10.1016/j.csr.2016.07.011.

Wang, Y., R. M. Castelao, and Y. Yuan (2015), Seasonal variability of alongshore winds and sea surface temperature fronts in Eastern Boundary Current Systems, *Journal of Geophysical Research: Oceans*, *120*, 2385-2400, doi:10.1002/2014jc010379.

Wang, Y., J. Liu, H. Liu, P. Lin, Y. Yuan, and F. Chai (2021), Seasonal and interannual variability in the sea surface temperature front in the eastern Pacific Ocean, *Journal of Geophysical Research: Oceans*, e2020JC016356, doi:10.1029/2020JC016356.

Woodson, C. B., and S. Y. Litvin (2015), Ocean fronts drive marine fishery production and biogeochemical cycling, *Proceedings of the National Academy of Sciences of the United States of America*, *112*(6), 1710-1715, doi:10.1073/pnas.1417143112.

Yuan, Y., and R. M. Castelao (2017), Eddy-induced sea surface temperature gradients in Eastern Boundary Current Systems, *Journal of Geophysical Research: Oceans*, *122*, 4791-4801, doi:10.1002/2017JC012735.

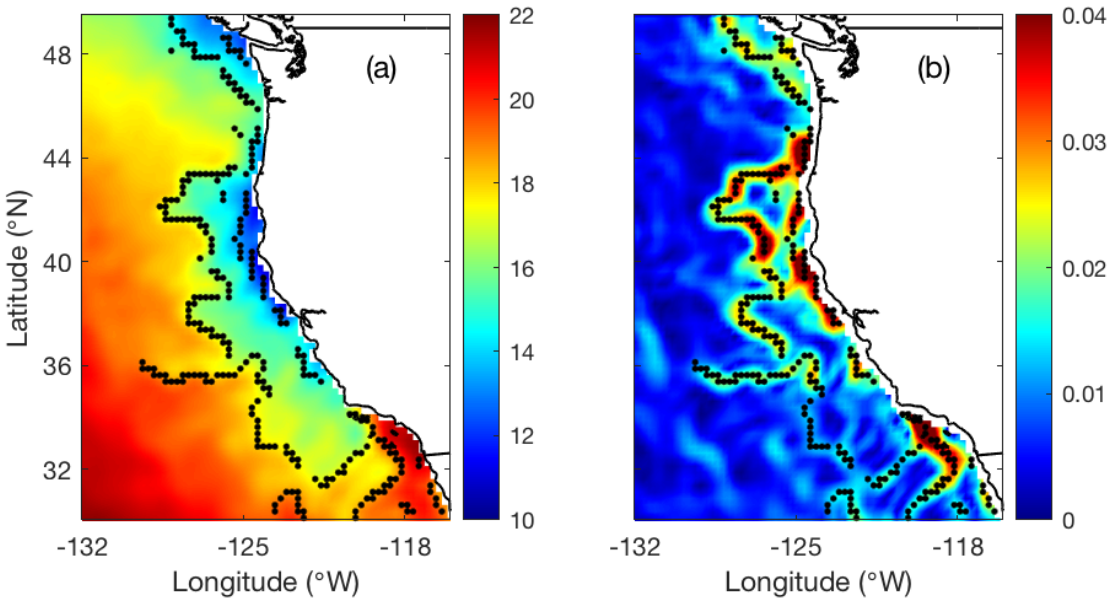

Figure 4.1. Example of using GHRSST AVHRR-only SST to calculate the SST gradient magnitude and to detect fronts on September 4, 2016. (a) SST (°C) and (b) SST gradient magnitude (°C km^{-1}) overlayed with the locations of fronts (black dots).

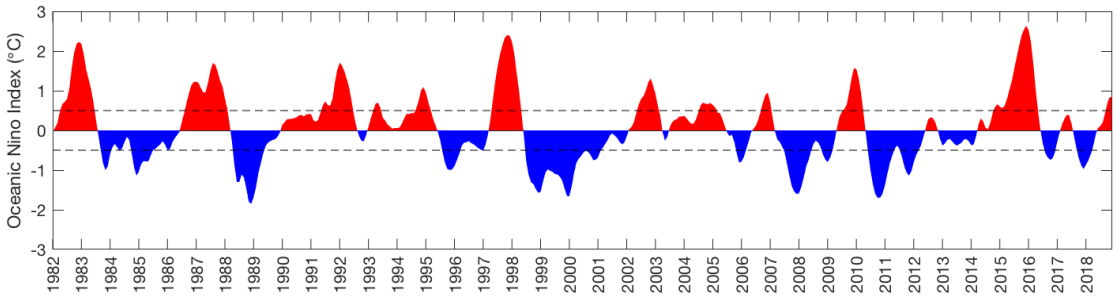

Figure 4.2. Oceanic Niño Index (ONI), defined as the three-month running mean of SST anomalies in the Niño 3.4 region. El Niño (La Niña) events occur when the ONI reaches ≥ 0.5°C (≤ -0.5°C) (dashed lines) for a minimum of five consecutive months (NOAA Climate Prediction Center).

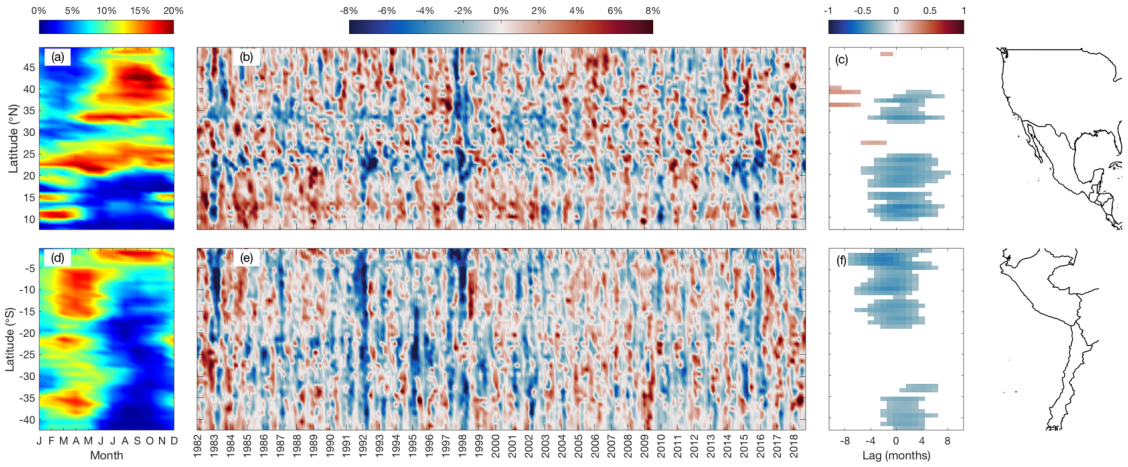

Figure 4.3. (a, d) Climatological mean (2003-2013) of SST frontal probability (%) within 0-300 km from the coast in 1° latitude boxes, computed from fronts detected using GHRSST AVHRR-only SST. (b, e) The three-month running mean of SST frontal probability anomalies (%) computed by subtracting the climatological monthly mean (shown in panels a and d) from each individual month. (c, f) Lagged correlation between SST frontal probability anomalies in panels b and e and the ONI (Figure 4.2) at each latitude. The x-axis represents the months by which frontal probability lags the ONI (positive lag is defined as the changes in frontal probability occurring after the peak in the ONI). Only significant correlations are shown.

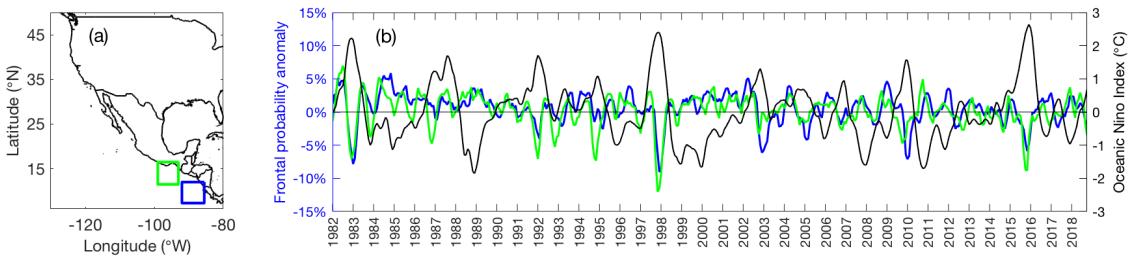

Figure 4.4. (a) The locations of the Gulfs of Tehuantepec (green box) and Papagayo (blue box). (b) The running three-month mean of SST frontal probability anomalies (%) computed by subtracting the climatological monthly mean (2003-2013) from each individual month in the Gulfs of Tehuantepec (green line) and Papagayo (blue line). The Oceanic Niño Index (°C) is shown by the black line.

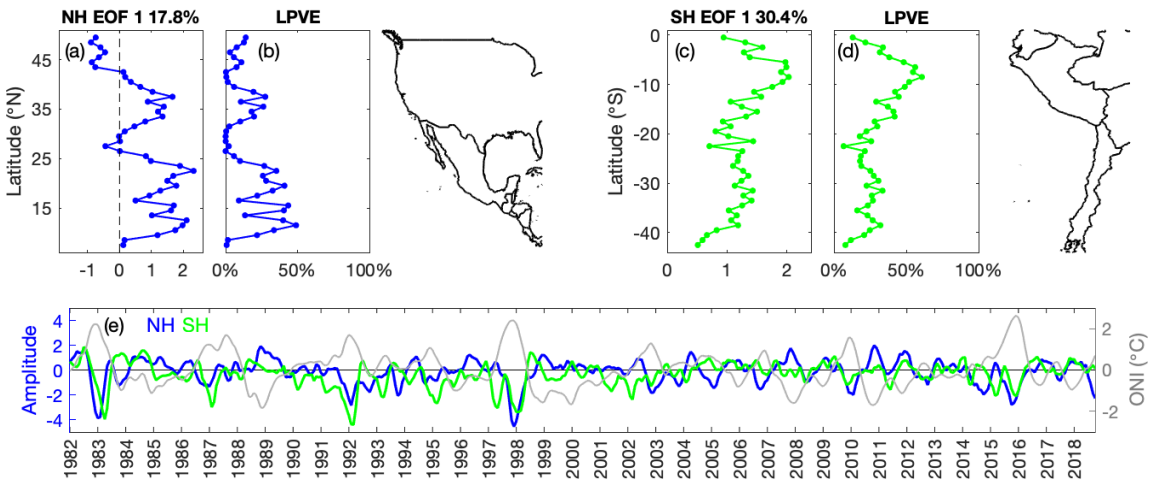

Figure 4.5. (a, c) Spatial functions, (b, d) local percentage of variance explained (LPVE), and (e) amplitude time series for EOF 1 of SST frontal probability anomalies along the west coasts of North (a, b) and South (c, d) America. The grey line in panel e is the timeseries of the Oceanic Niño Index (ONI; °C).

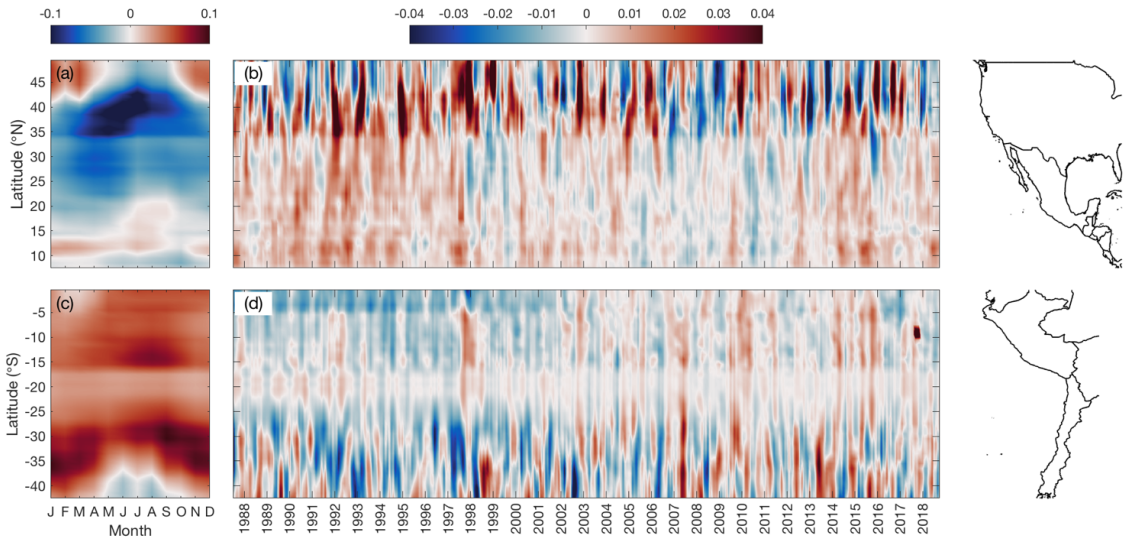

Figure 4.6. (a, c) Climatological mean (2003-2013) of alongshore winds stress (N m^{-2}) averaged within 0-300 km from the coast in 1° latitude boxes, computed using CCMP v2.0 surface vector winds. (b, d) The three-month running mean of alongshore wind stress anomalies (N m^{-2}) computed by subtracting the monthly climatological mean (shown in panels a and c) from each individual month.

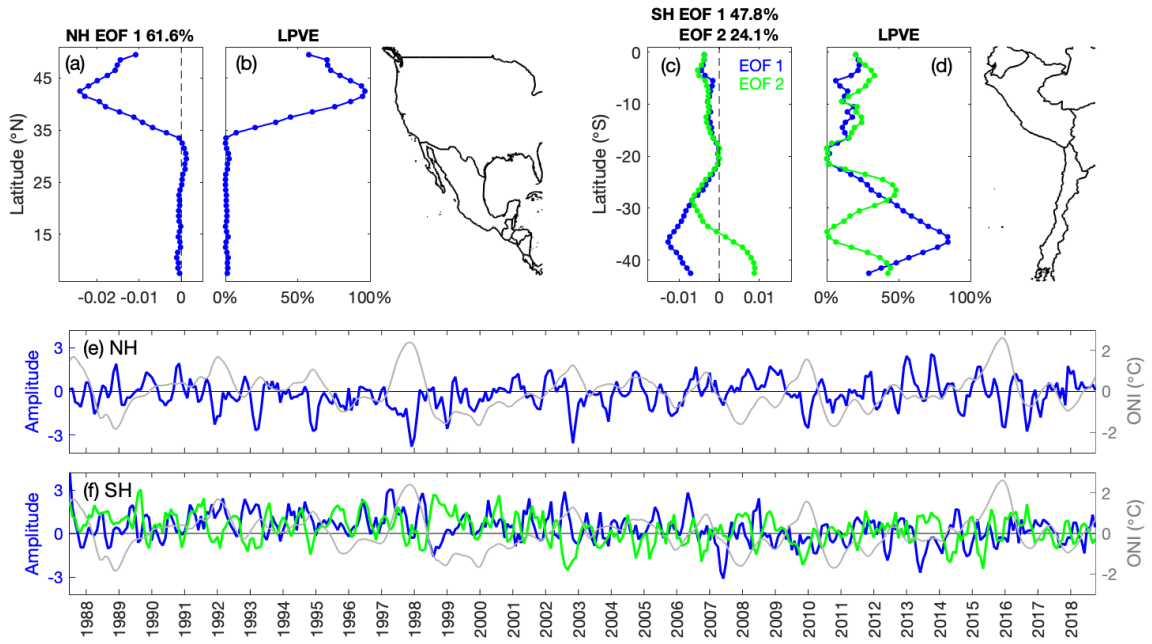

Figure 4.7. (a, c) Spatial functions, (b, d) local percentage of variance explained (LPVE), and (e, f) amplitude time series for EOF 1 of alongshore wind stress anomalies along the west coasts of North (a, b, e) and South (c, d, f) America. EOF 2 for alongshore wind stress off South America is shown in green in panels c, d, and f. The grey line in panels e-f is the timeseries of the Oceanic Niño Index (ONI; °C).

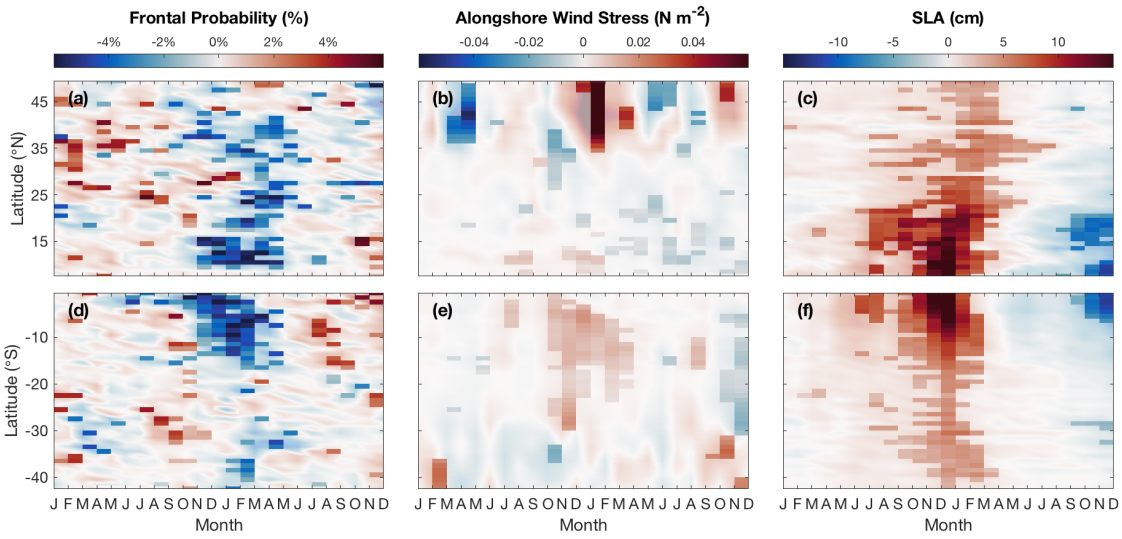

Figure 4.8. 2-year composite differences computed by subtracting the neutral composite from the composite for moderate to strong El Niño events (defined as ONI ≥ 1°C for at least 3 consecutive months) in each 1° latitude box within 0-300 km offshore for (a, d) mean SST frontal probability (%), (b, e) mean alongshore wind stress (N m^{-2}), and (c, f) mean SLA (cm) along the west coasts of North (a, b, d) and South (d, e, f) America. Light shading (transparency of 60%) indicates values that are not significant (p-value > 0.1). The El Niño (neutral) composites for frontal probability, alongshore wind stress, and SLA included 8 (10), 6 (9), and 5 (6) events, respectively. The same data are shown in Figure C.2, but with significance levels determined using a p-value of 0.05.

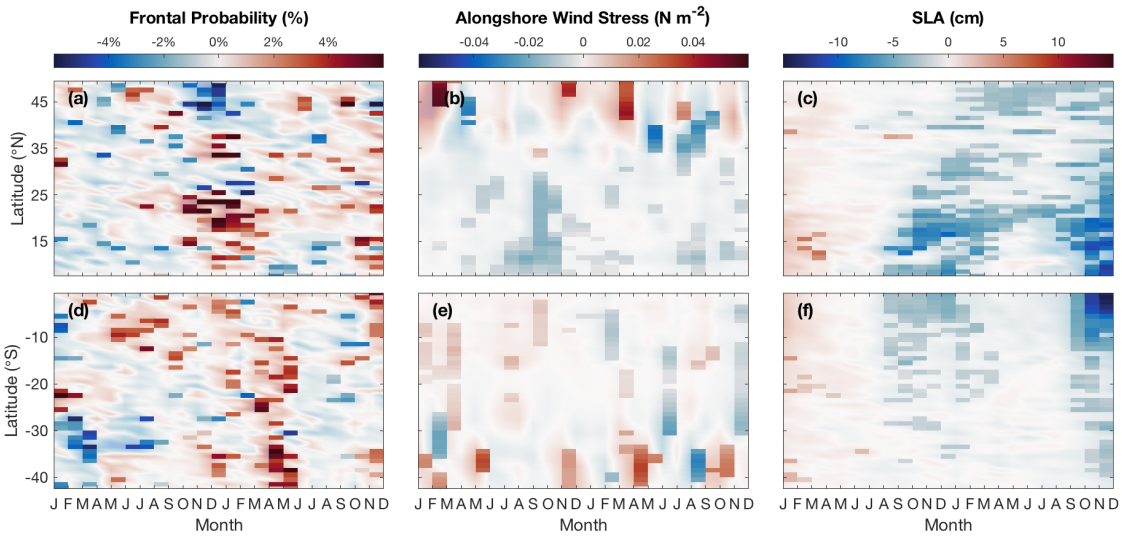

Figure 4.9. 2-year composite differences computed by subtracting the neutral composite from the composite for moderate to strong La Niña events (defined as ONI ≤ -1°C for at least 3 consecutive months) in each 1° latitude box within 0-300 km offshore for (a, d) mean SST frontal probability (%), (b, e) mean alongshore wind stress (N m^{-2}), and (c, f) mean SLA (cm) along the west coasts of North (a, b, d) and South (d, e, f) America. Light shading (transparency of 60%) indicates values that are not significant (p-value > 0.1). The La Niña (neutral) composites for frontal probability, alongshore wind stress, and SLA included 7 (10), 7 (9), and 6 (6) events, respectively. The same data are shown in Figure C.3, but with significance levels determined using a p-value of 0.05.

CHAPTER 5

CONCLUSIONS

Eastern Boundary Current Systems (EBCS) are highly productive marine ecosystems due to coastal upwelling (Huyer, 1983). The coastal zones in EBCS are very energetic, featuring upwelling jets, eddies, and sea surface temperature fronts (e.g., Barth et al., 2000; Chelton et al., 2011; Wang et al., 2015). These physical processes can contribute to the horizontal and vertical distribution of physical and biogeochemical properties, influencing biological activity in these systems (Liang et al., 2009; Combes et al., 2013; Nagai et al., 2015; Chenillat et al., 2016; Lovecchio et al., 2018). The physical dynamics associated with upwelling in EBCS have received a great deal of attention over the past few decades, especially with advancements in satellite observations which have made it possible to study large regions of the surface ocean. The research presented in this dissertation utilized several satellite products to expand our understanding of upwelling dynamics and the implications for the marine ecosystems in EBCS.

The offshore transport of upwelled coastal water by mesoscale eddies in EBCS was investigated in chapters 2 and 3. In chapter 2, satellite-derived measurements of particulate organic carbon (POC) were used as a tracer of coastal water to quantify the offshore transport of coastal water by eddies in the California Current System (CCS), one of the four major EBCS. A procedure was developed to isolate the satellite-derived POC anomalies associated with nonlinear mesoscale eddies in the CCS. The analyses indicate

that cyclonic eddies generated near the coast can trap coastal water that is rich in POC due to upwelling and transport this water offshore for hundreds of kilometers. This transport mechanism results in an eddy-induced volume transport of ~1 Sv and an offshore enrichment of POC of 20.9 ± 11 Gg year^{-1}. This research provides large-scale observational-based evidence that mesoscale eddies play an important role in the redistribution of coastal water in the CCS.

Chapter 3 expanded on the analyses in chapter 2 by investigating offshore transport by nonlinear mesoscale eddies in the other major EBCS, the Humboldt, Canary, and Benguela Current Systems (HCS, CanCS, and BCS, respectively). Eddy-induced offshore transport of coastal water was shown to be important in all EBCS, with cyclonic eddies producing offshore POC enrichments of 22.6 ± 5.1 Gg year^{-1} (37-43°N), 16.1 ± 3.1 Gg year^{-1} (34-42°S), 16.8 ± 6.1 Gg year^{-1} (21-28°N), and 3.6 ± 3.1 Gg year^{-1} (29-35°S) in the California, Humboldt, Canary and Benguela Current Systems, respectively. There was large spatial variability in the effectiveness of this eddy-induced transport, with the analysis indicating regions within each EBCS where this mechanism is most important. The regions with the most offshore transport are often associated with upwelling jet separation, which helps produce favorable conditions for the trapping and offshore transport of coastal water by nonlinear eddies. Eddies produce offshore volume transports that are similar to the cross-shore transport by jet separation (~1 Sv), however, eddies can transport the coastal water farther offshore. The research in chapters 2 and 3 has shown that eddies can be an important transport mechanism for substantially widening the area influenced by highly productive upwelled waters in the EBCS. This can affect heat and salt fluxes (Dong et al., 2014) and redistribute coastal water that is

rich in carbon and nutrients, which can have important implications for the marine ecosystems in the EBCS.

Future work can address several limitations and expand on the analyses presented in chapters 2 and 3. Current satellite altimetry can only detect eddies with radii larger than 40-50 km, therefore only these eddies are included in this research. Smaller, submesoscale eddies likely also contribute to the redistribution of upwelled water but they cannot be resolved with current altimetry. The estimates of volume transport and offshore POC enrichment may be higher if these submesoscale eddies are included. Future studies using SWOT (NASA's Surface Water and Ocean Topography mission; Fu et al., 2012), which will provide sea level anomalies at higher resolution, can investigate the role of smaller eddies on offshore transport in the EBCS. Additionally, the volume transport is calculated using a trapping efficiency of 1, meaning that none of the initially trapped coastal water is leaking from an eddy as it propagates offshore. It's possible however, that some of the trapped water is leaking from the eddies, so assuming a trapping efficiency of 1 would overestimate the volume transports. The estimates of offshore POC enrichment were calculated using anomalies of POC content in the top 100 m. In situ data in the CCS was used to find a relationship between surface POC concentrations and POC integrated from the surface to 100 m depth. This allowed for the POC content in the top 100 m to be estimated from satellite-derived POC data. This relationship was applied to all EBCS; however, this may not hold true in the CanCS, HCS and BCS, which leads to uncertainties in our estimates of offshore POC enrichment in these regions. Future work can improve the estimates of offshore volume transport and POC enrichment by using more representative trapping efficiencies and using in situ POC

measurements collected in the other EBCS (if available) to determine the relationship between POC at the surface and POC content in the top 100 m. This research can also be expanded by investigating the eddy-induced transport mechanism in other regions, such as downwelling-favorable systems and those with buoyancy-driven currents. The redistribution of coastal water by eddies may be different in these regions compared to EBCS. For example, anticyclones may play a more important role in redistributing coastal water, as opposed to cyclones which are important in the EBCS. Future studies can apply the procedure developed in chapter 2 to the coastal ocean near Cape Horn in the southern HCS and the eastern Gulf of Alaska, for example, to investigate this.

EBCS also feature sea surface temperature (SST) fronts that form at the boundary between cold, upwelled water along the coast and warmer offshore waters. Chapter 4 investigated the interannual variability of SST fronts in the CCS and HCS, with particular interest in the El Niño-Southern Oscillation (ENSO) because it is known to affect upwelling dynamics in the eastern Pacific Ocean. Thirty-seven years of satellite SST measurements were used to detect fronts along the west coasts of North and South America using an edge-detection algorithm. Frontal activity generally decreased during El Niño events and increased during La Niña events along most of the coastline in these regions. The decrease in frontal activity off South America during El Niño coincided with the seasonal peak in frontal activity, while off North America the decrease occurred when frontal activity was at a seasonal minimum. Since fronts can influence biological activity and air-sea coupling (Chelton et al., 2001; Chelton et al., 2007; Wang and Castelao, 2016), then the affects of reduced frontal activity will presumably be larger along the coast of Central and South America.

Satellite measurements of wind stress and sea level anomaly were also utilized in chapter 4 to investigate how oceanic and atmospheric forcing mechanisms associated with ENSO affect frontal activity. Analyses indicated that off Central and South America, oceanic forcing (i.e., coastal Kelvin waves) is likely the main contributor to the decrease in frontal activity during El Niño events. In the CCS, the decrease in frontal activity is likely due to both oceanic forcing and atmospheric teleconnections associated with ENSO. It is difficult in this region to identify which of these forcing mechanisms has a larger influence on the reduction in frontal activity based on observations alone. Future studies using idealized model simulations where forcing is systematically varied could help disentangle the contribution of these forcing on frontal variability in the CCS. Additionally, the use of a 37 year-long time series of satellite SST only allows for capturing a few El Niño events, and even fewer strong events, since these events occur every 3-7 years. The relatively short time series also makes it difficult to identify the influence of other modes of variability, such as the Pacific Decadal Oscillation. As more data are collected and satellite time series are expanded, future studies will be able to expand on our understanding of the relationships between SST frontal activity and climate variability in EBCS.

References

Barth, J. A., S. D. Pierce, and R. L. Smith (2000), A separating coastal upwelling jet at Cape Blanco, Oregon and its connection to the California Current System, *Deep-Sea Research II*, *47*, 783-810, doi:10.1016/S0967-0645(99)00127-7.

Chelton, D. B., S. K. Esbensen, M. G. Schlax, N. Thum, and M. H. Freilich (2001), Observations of coupling between surface wind stress and sea surface temperature in the Eastern Tropical Pacific, *Journal of Climate*, *14*, 1479-1498, doi:10.1175/1520-0442(2001)014<1479:OOCBSW>2.0.CO;2.

Chelton, D. B., M. G. Schlax, and R. M. Samelson (2007), Summertime Coupling between Sea Surface Temperature and Wind Stress in the California Current System, *Journal of Physical Oceanography*, *37*, 495-517, doi:10.1175/JPO3025.1.

Chelton, D. B., M. G. Schlax, and R. M. Samelson (2011), Global observations of nonlinear mesoscale eddies, *Progress in Oceanography*, *91*, 167-216, doi:10.1016/j.pocean.2011.01.002.

Chenillat, F., P. J. S. Franks, and V. Combes (2016), Biogeochemical properties of eddies in the California Current System, *Geophysical Research Letters*, *43*, 5812-5820, doi:10.1002/2016gl068945.

Combes, V., F. Chenillat, E. Di Lorenzo, P. Rivière, M. D. Ohman, and S. J. Bograd (2013), Cross-shore transport variability in the California Current: Ekman upwelling vs. eddy dynamics, *Progress in Oceanography*, *109*, 78-89, doi:10.1016/j.pocean.2012.10.001.

Dong, C., J. C. McWilliams, Y. Liu, and D. Chen (2014), Global heat and salt transports by eddy movement, *Nature communications*, *5*(1), 1-6, doi:10.1038/ncomms4294.

Fu, L.-L., D. Alsdorf, R. Morrow, E. Rodriguez, and N. Mognard (2012), *SWOT: the surface water and ocean topography mission: wide-swath altimetric elevation on Earth*. NASA. Retrieved from http://hdl.handle.net/2014/41996.

Huyer, A. (1983), Coastal upwelling in the California Current System, *Progress in Oceanography*, *12*, 259-284, doi:10.1016/0079-6611(83)90010-1.

Liang, J. H., J. C. McWilliams, and N. Gruber (2009), High-frequency response of the ocean to mountain gap winds in the northeastern tropical Pacific, *Journal of Geophysical Research: Oceans*, *114*(C12), doi:10.1029/2009JC005370.

Lovecchio, E., N. Gruber, and M. Münnich (2018), Mesoscale contribution to the long-range offshore transport of organic carbon from the Canary Upwelling System to the open North Atlantic, *Biogeosciences*, *15*, 5061-5091, doi:10.5194/bg-15-5061-2018.

Nagai, T., N. Gruber, H. Frenzel, Z. Lachkar, J. C. McWilliams, and G.-K. Plattner (2015), Dominant role of eddies and filaments in the offshore transport of carbon and nutrients in the California Current System, *Journal of Geophysical Research: Oceans*, *120*, 5318-5341, doi:10.1002/2015jc010889.

Wang, Y., R. M. Castelao, and Y. Yuan (2015), Seasonal variability of alongshore winds and sea surface temperature fronts in Eastern Boundary Current Systems, *Journal of Geophysical Research: Oceans*, *120*, 2385-2400, doi:10.1002/2014jc010379.

REFERENCES

Aguirre, C., Ó. Pizarro, P. T. Strub, R. Garreaud, and J. A. Barth (2012), Seasonal dynamics of the near-surface alongshore flow off central Chile, *Journal of Geophysical Research: Oceans*, *117*(C1), doi:10.1029/2011JC007379.

Ahlgren, G., I. B. Gustafsson, and M. Boberg (1992), Fatty acid content and chemical composition of freshwater microalgae, *Journal of phycology*, *28*(1), 37-50, doi:10.1111/j.0022-3646.1992.00037.x.

Alexander, M. A., I. Bladé, M. Newman, J. R. Lanzante, N.-C. Lau, and J. D. Scott (2002), The atmospheric bridge: The influence of ENSO teleconnections on air-sea interaction over the global oceans, *Journal of Climate*, *15*(16), 2205-2231, doi:10.1175/1520-0442(2002)015<2205:TABTIO>2.0.CO;2.

Alexander, M. A., H. Seo, S. P. Xie, and J. D. Scott (2012), ENSO's impact on the gap wind regions of the Eastern Tropical Pacific Ocean, *Journal of Climate*, *25*, 3549-3565, doi:10.1175/JCLI-D-11-00320.1.

Allen, J. (1980), Models of wind-driven currents on the continental shelf, *Annual Review of Fluid Mechanics*, *12*(1), 389-433, doi:10.1146/annurev.fl.12.010180.002133.

Allen, J., P. Newberger, and J. Federiuk (1995), Upwelling circulation on the Oregon continental shelf. Part I: Response to idealized forcing, *Journal of Physical Oceanography*, *25*(8), 1843-1866, doi:10.1175/1520-0485(1995)025<1843:UCOTOC>2.0.CO;2.

Allison, D. B., D. Stramski, and B. G. Mitchell (2010), Seasonal and interannual variability of particulate organic carbon within the Southern Ocean from satellite ocean color observations, *Journal of Geophysical Research*, *115*, C06002, doi:10.1029/2009jc005347.

Aluwihare, L. (2018), Particulate organic carbon and nitrogen measurements at selected depths in the water column in the CCS region since 2006 - 2016 (ongoing), edited by E. D. Initiative, doi:10.6073/pasta/20c05dd205be2225ecb32a5fede1c36c.

Amores, A., G. Jordà, T. Arsouze, and J. Le Sommer (2018), Up to what extent can we characterize ocean eddies using present-day gridded altimetric products?, *Journal of Geophysical Research: Oceans*, *123*, 7220-7236, doi:10.1029/2018JC014140.

Amores, A., O. Melnichenko, and N. Maximenko (2017), Coherent mesoscale eddies in the North Atlantic subtropical gyre: 3-D structure and transport with application to the salinity maximum, *Journal of Geophysical Research: Oceans*, *122*, 23-41, doi:10.1002/2016JC012256.

Amos, C. M., R. M. Castelao, and P. M. Medeiros (2019), Offshore transport of particulate organic carbon in the California Current System by mesoscale eddies, *Nature Communications*, *10*, 4940, doi:10.1038/s41467-019-12783-5.

Atlas, R., R. N. Hoffman, J. Ardizzone, S. M. Leidner, J. C. Jusem, D. K. Smith, and D. Gombos (2010), A cross-calibrated, multiplatform ocean surface wind velocity product for meteorological and oceanographic applications, *Bulletin of the American Meteorological Society*, *92*, 157-174, doi:10.1175/2010BAMS2946.1.

Bakun, A. (1990), Global climate change and intensitifcation of coastal ocean upwelling, *Science*, *247*(4939), 198-201, doi:10.1126/science.247.4939.198.

Bakun, A., and C. S. Nelson (1991), The Seasonal Cycle of Wind-Stress Curl in Subtropical Eastern Boundary Current Regions, *Journal of Physical Oceanography*, *21*(12), 1815-1834, doi:10.1175/1520-0485(1991)021<1815:TSCOWS>2.0.CO;2.

Barth, J. A., S. D. Pierce, and T. J. Cowles (2005), Mesoscale structure and its seasonal evolution in the northern California Current System, *Deep-Sea Research II*, *52*(1-2), 5-28, doi:10.1016/j.dsr2.2004.09.026.

Barth, J. A., S. D. Pierce, and R. L. Smith (2000), A separating coastal upwelling jet at Cape Blanco, Oregon and its connection to the California Current System, *Deep-Sea Research II*, *47*, 783-810, doi:10.1016/S0967-0645(99)00127-7.

Barton, E. D., M. L. Argote, J. Brown, P. M. Kosro, M. Lavin, J. M. Robles, R. L. Smith, A. Trasviña, and H. S. Velez (1993), Supersquirt: Dynamics of the Gulf of Tehuantepec, Mexico, *Oceanography*, *6*, 23-30, doi:10.5670/oceanog.1993.19.

Barton, E. D., A. Huyer, and R. L. Smith (1977), Temporal variation observed in the hydrographic regime near Cabo Corveiro in the northwest African upwelling region, February to April 1974, *Deep Sea Research*, *24*(1), 7-23, doi:10.1016/0146-6291(77)90537-9.

Batteen, M. L., C.-P. Hu, J. L. Bacon, and C. S. Nelson (1995), A numerical study of the effects of wind forcing on the Chile Current System, *Journal of Oceanography*, *51*(5), 585-614, doi:10.1007/BF02270526.

Batteen, M. L., J. R. Martinez, D. W. Bryan, and E. J. Buch (2000), A modeling study of the coastal eastern boundary current system off Iberia and Morocco, *Journal of*

Geophysical Research: Oceans, *105*(C6), 14173-14195, doi:10.1029/2000JC900026.

Bauer, J. E., E. R. M. Druffel, P. M. Williams, D. M. Wolgast, and S. Griffin (1998), Temporal variability in dissolved organic carbon and radiocarbon in the eastern North Pacific Ocean, *Journal of Geophysical Research*, *103*(C2), 2867-2881.

Blanco, J. L., M. E. Carr, A. C. Thomas, and P. T. Strub (2002), Hydrographic conditions off northern Chile during the 1996–1998 La Nina and El Nino events, *Journal of Geophysical Research: Oceans*, *107*(C3), 3-1-3-19, doi:10.1029/2001JC001002.

Bowman, M. J. (1978), Oceanic fronts in coastal processes, in *Oceanic Fronts in Coastal Processes*, edited by M. Bowman and W. Esias, pp. 2-5, Springer, NY.

Brink, K., D. Halpern, A. Huyer, and R. Smith (1983), The physical environment of the Peruvian upwelling system, *Progress in Oceanography*, *12*(3), 285-305, doi:10.1016/0079-6611(83)90011-3.

Canny, J. (1986), A Computational Approach to Edge Detection, *IEEE Transactions on Pattern Analysis and Machine Intelligence*, *PAMI-8*(6), 679-698, doi:10.1109/TPAMI.1986.4767851.

Capet, X., F. Colas, J. C. McWilliams, P. Penven, and P. Marchesiello (2008), Eddies in eastern boundary subtropical upwelling systems, *Ocean Modeling in an Eddying Regime*, *177*, 350, doi:10.1029/177GM10.

Capet, X., J. C. McWilliams, M. J. Molemaker, and A. Shchepetkin (2008), Mesoscale to submesoscale transition in the California Current System. Part II: Frontal processes, *Journal of Physical Oceanography*, *38*, 44-64, doi:10.1175/2007JPO3672.1.

Capet, X., J. C. McWilliams, M. J. Molemaker, and A. F. Shchepetkin (2008), Mesoscale to submesoscale transition in the California Current System. Part I: Flow structure, eddy flux, and observational tests, *Journal of Physical Oceanography*, *38*, 29-43, doi:10.1175/2007JPO3671.1.

Carr, M.-E. (2001), Estimation of potential productivity in Eastern Boundary Currents using remote sensing, *Deep Sea Research Part II: Topical Studies in Oceanography*, *49*(1-3), 59-80, doi:10.1016/S0967-0645(01)00094-7.

Carr, M.-E., and E. J. Kearns (2003), Production regimes in four Eastern Boundary Current systems, *Deep Sea Research Part II: Topical Studies in Oceanography*, *50*(22-26), 3199-3221, doi:0.1016/j.dsr2.2003.07.015.

Carr, M. E., P. T. Strub, A. C. Thomas, and J. L. Blanco (2002), Evolution of 1996–1999 La Niña and El Niño conditions off the western coast of South America: a remote sensing perspective, *Journal of Geophysical Research: Oceans*, *107*(C12), 29-21-29-16, doi:10.1029/2001JC001183.

Castelao, R. M., and J. A. Barth (2005), Coastal ocean response to summer upwelling favorable winds in a region of alongshore bottom topography variations off Oregon, *Journal of Geophysical Research*, *110*, C10S04, doi:10.1029/2004JC002409.

Castelao, R. M., J. A. Barth, and T. P. Mavor (2005), Flow-topography interactions in the northern California Current System observed from geostationary satallite data, *Geophysical Research Letters*, *32*, L24612, doi:10.1029/2005GL024401.

Castelao, R. M., M. S. Dinniman, C. M. Amos, J. M. Klinck, and P. M. Medeiros (2021), Eddy-Driven Transport of Particulate Organic Carbon-Rich Coastal Water Off the

West Antarctic Peninsula, *Journal of Geophysical Research: Oceans*, *126*(3), e2020JC016791, doi:10.1029/2020JC016791.

Castelao, R. M., and H. Luo (2018), Upwelling jet separation in the California Current System, *Scientific Reports*, *8*, 16004, doi:10.1038/s41598-018-34401-y.

Castelao, R. M., T. P. Mavor, J. A. Barth, and L. C. Breaker (2006), Sea surface temperature fronts in the California Current System from geostationary satellite observations, *Journal of Geophysical Research*, *111*, C09026, doi:10.1029/2006jc003541.

Castelao, R. M., and Y. Wang (2014), Wind-driven variability in sea surface temperature front distribution in the California Current System, *Journal of Geophysical Research: Oceans*, *119*, 1861-1875, doi:10.1002/2013jc009531.

Chaigneau, A., G. Eldin, and B. Dewitte (2009), Eddy activity in the four major upwelling systems from satellite altimetry (1992–2007), *Progress in Oceanography*, *83*, 117-123, doi:10.1016/j.pocean.2009.07.012.

Chaigneau, A., M. Le Texier, G. Eldin, C. Grados, and O. Pizarro (2011), Vertical structure of mesoscale eddies in the eastern South Pacific Ocean: A composite analysis from altimetry and Argo profiling floats, *Journal of Geophysical Research*, *116*, C11025, doi:10.1029/2011JC007134.

Chavez, F. P., and M. Messié (2009), A comparison of Eastern Boundary Upwelling Ecosystems, *Progress in Oceanography*, *83*, 80-96, doi:10.1016/j.pocean.2009.07.032.

Chavez, F. P., J. T. Pennington, C. G. Castro, J. P. Ryan, R. P. Michisaki, B. Schlining, P. Walz, K. R. Buck, A. McFadyen, and C. A. Collins (2002), Biological and

chemical consequences of the 1997-1998 El Niño in central California waters, *Progress in Oceanography*, *54*, 205-232, doi:10.1016/S0079-6611(02)00050-2.

Chelton, D. B., and R. E. Davis (1982), Monthly Mean Sea-Level Variability Along the West Coast of North America, *Journal of Physical Oceanography*, *12*, 757-784, doi:10.1175/1520-0485(1982)012<0757:MMSLVA>2.0.CO;2.

Chelton, D. B., S. K. Esbensen, M. G. Schlax, N. Thum, and M. H. Freilich (2001), Observations of coupling between surface wind stress and sea surface temperature in the Eastern Tropical Pacific, *Journal of Climate*, *14*, 1479-1498, doi:10.1175/1520-0442(2001)014<1479:OOCBSW>2.0.CO;2.

Chelton, D. B., M. H. Freilich, and S. K. Esbensen (2000), Satellite observations of the wind jets off the Pacific coast of Central America. Part I: Case studies and statistical characteristics, *Monthly Weather Review*, *128*, 1993-2018, doi:10.1175/1520-0493(2000)128<2019:SOOTWJ>2.0.CO;2.

Chelton, D. B., P. Gaube, M. G. Schlax, J. J. Early, and R. M. Samelson (2011), The Influence of Nonlinear Mesoscale Eddies on Near-Surface Oceanic Chlorophyll, *Science*, *334*, 328-334, doi:10.1126/science.1208897.

Chelton, D. B., M. G. Schlax, M. H. Freilich, and R. F. Milliff (2004), Satellite measurements reveal persistent small-scale features in ocean winds, *Science*, *303*, 978, doi:10.1126/science.1091901.

Chelton, D. B., M. G. Schlax, and R. M. Samelson (2007), Summertime Coupling between Sea Surface Temperature and Wind Stress in the California Current System, *Journal of Physical Oceanography*, *37*, 495-517, doi:10.1175/JPO3025.1.

Chelton, D. B., M. G. Schlax, and R. M. Samelson (2011), Global observations of nonlinear mesoscale eddies, *Progress in Oceanography*, *91*, 167-216, doi:10.1016/j.pocean.2011.01.002.

Chenillat, F., P. J. S. Franks, and V. Combes (2016), Biogeochemical properties of eddies in the California Current System, *Geophysical Research Letters*, *43*, 5812-5820, doi:10.1002/2016gl068945.

Chenillat, F., P. J. S. Franks, P. Rivière, X. Capet, N. Grima, and B. Blanke (2015), Plankton dynamics in a cyclonic eddy in the Southern California Current System, *Journal of Geophysical Research: Oceans*, *120*, 5566-5588, doi:10.1002/2015JC010826.

Clarke, A. J., and S. Van Gorder (1994), On ENSO Coastal Currents and Sea Levels, *Journal of Physical Oceanography*, *24*, 661-680, doi:10.1175/1520-0485(1994)024<0661:OECCAS>2.0.CO;2.

Combes, V., F. Chenillat, E. Di Lorenzo, P. Rivière, M. D. Ohman, and S. J. Bograd (2013), Cross-shore transport variability in the California Current: Ekman upwelling vs. eddy dynamics, *Progress in Oceanography*, *109*, 78-89, doi:10.1016/j.pocean.2012.10.001.

Crawford, W. R., P. J. Brickley, and A. C. Thomas (2007), Mesoscale eddies dominate surface phytoplankton in northern Gulf of Alaska, *Progress in Oceanography*, *75*, 287-303, doi:10.1016/j.pocean.2007.08.016.

Dahm, C. N., S. V. Gregory, and P. K. Park (1981), Organic Carbon Transport in the Columbia River, *Estuarine, Coastal and Shelf Science*, *13*, 645-658.

Dauhajre, D. P., J. C. McWilliams, and Y. Uchiyama (2017), Submesoscale coherent structures on the continental shelf, *Journal of Physical Oceanography*, *47*, 2949-2976, doi:10.1175/JPO-D-16-0270.1.

Doherty, M., P. L. Yager, M. A. Moran, V. J. Coles, C. S. Fortunato, A. V. Krusche, P. M. Medeiros, J. P. Payet, J. E. Richey, and B. M. Satinsky (2017), Bacterial biogeography across the Amazon River-ocean continuum, *Frontiers in Microbiology*, *8*, 882, doi:10.3389/fmicb.2017.00882.

Dong, C., J. C. McWilliams, Y. Liu, and D. Chen (2014), Global heat and salt transports by eddy movement, *Nature communications*, *5*(1), 1-6, doi:10.1038/ncomms4294.

Druffel, E. R. M., J. E. Bauer, P. M. Williams, S. Griffin, and D. Wolgast (1996), Seasonal variability of particulate organic radiocarbon in the northeast Pacific Ocean, *Journal of Geophysical Research*, *101*(C9), 20,542-520,552.

Early, J. J., R. M. Samelson, and D. B. Chelton (2011), The Evolution and Propagation of Quasigeostrophic Ocean Eddies, *American Meteorological Society*, *41*, 1535-1555, doi:10.1175/2011JPO4601.1.

Enfield, D. B., and J. S. Allen (1980), On the Structure and Dynamics of Monthly Mean Sea Level Anomalies along the Pacific Coast of North and South America, *Journal of Physical Oceanography*, *10*, 557-578, doi:10.1175/1520-0485(1980)010<0557:OTSADO>2.0.CO;2.

Espinoza-Morriberón, D., V. Echevin, F. Colas, J. Tam, J. Ledesma, L. Vásquez, and M. Graco (2017), Impacts of El Niño events on the Peruvian upwelling system productivity, *Journal of Geophysical Research: Oceans*, *122*(7), 5423-5444, doi:10.1002/2016JC012439.

Frischknecht, M., M. Münnich, and N. Gruber (2015), Remote versus local influence of ENSO on the California Current System, *Journal of Geophysical Research: Oceans*, *120*, 1353-1374, doi:10.1002/2014JC010531.

Fu, L.-L., D. Alsdorf, R. Morrow, E. Rodriguez, and N. Mognard (2012), *SWOT: the surface water and ocean topography mission: wide-swath altimetric elevation on Earth*, NASA. Retrieved from http://hdl.handle.net/2014/41996.

García-Reyes, M., and J. L. Largier (2012), Seasonality of coastal upwelling off central and northern California: New insights, including temporal and spatial variability, *Journal of Geophysical Research: Oceans*, *117*, C03028, doi:10.1029/2011jc007629.

Gaube, P., D. B. Chelton, P. G. Strutton, and M. J. Behrenfeld (2013), Satellite observations of chlorophyll, phytoplankton biomass, and Ekman pumping in nonlinear mesoscale eddies, *Journal of Geophysical Research: Oceans*, *118*, 6349-6370, doi:10.1002/2013jc009027.

Gaube, P., and D. J. McGillicuddy Jr. (2017), The influence of Gulf Stream eddies and meanders on near-surface chlorophyll, *Deep-Sea Research I*, *122*, 1-16, doi:10.1016/j.dsr.2017.02.006.

Gaube, P., D. J. McGillicuddy Jr., D. B. Chelton, M. J. Behrenfeld, and P. G. Strutton (2014), Regional variations in the influence of mesoscale eddies on near-surface chlorophyll, *Journal of Geophysical Research: Oceans*, *119*, 8195-8220, doi:10.1002/ 2014JC010111.

Gaube, P., D. J. McGillicuddy Jr., and A. J. Moulin (2018), Mesoscale eddies modulate mixed layer depth globally, *Geophysical Research Letters*, *46*(3), 1505-1512, doi:10.1029/2018GL080006.

Gentemann, C. L., M. R. Fewings, and M. García-Reyes (2017), Satellite sea surface temperatures along the West Coast of the United States during the 2014-2016 northeast Pacific marine heat wave, *Geophysical Research Letters*, *44*, 312-319, doi:10.1002/2016gl071039.

Gruber, N., Z. Lachkar, H. Frenzel, P. Marchesiello, M. Münnich, J. C. McWilliams, T. Nagai, and G.-K. Plattner (2011), Eddy-induced reduction of biological production in eastern boundary upwelling systems, *Nature Geoscience*, *4*, 787-792, doi:10.1038/ngeo1273.

Haidvogel, D. B., et al. (2008), Ocean forecasting in terrain-following coordinates: Formulation and skill assessment of the Regional Ocean Modeling System, *Journal of Computational Physics*, *227*, 3595-3624, doi:10.1016/j.jcp.2007.06.016.

Haidvogel, D. B., A. Beckmann, and K. S. Hedström (1991), Dynamical simulations of filament formation and evolution in the coastal transition zone, *Journal of Geophysical Research*, *96*(C8), 15,017-015,040.

Haynes, R., and E. D. Barton (1991), Lagrangian observations in the Iberian coastal transition zone, *Journal of Geophysical Research: Oceans*, *96*(C8), 14731-14741, doi:10.1029/91JC00907.

Haynes, R., E. D. Barton, and I. Pilling (1993), Development, persistence and variability of upwelling filaments off the Atlantic coast of the Iberian Peninsula, edited, pp. 22681-22692, doi:10.1029/93JC02016.

Huyer, A. (1983), Coastal upwelling in the California Current System, *Progress in Oceanography*, *12*, 259-284, doi:10.1016/0079-6611(83)90010-1.

Huyer, A., M. Knoll, T. Paluszkiewicz, and R. L. Smith (1991), The Peru Undercurrent: a study in variability, *Deep Sea Research Part A. Oceanographic Research Papers*, *38*, S247-S271, doi:10.1016/S0198-0149(12)80012-4.

Huyer, A., and R. L. Smith (1974), A subsurface ribbon of cool water over the continental shelf off Oregon, *Journal of Physical Oceanography*, *4*(3), 381-391, doi:10.1175/1520-0485(1974)004<0381:ASROCW>2.0.CO;2.

Huyer, A., R. L. Smith, and J. Fleischbein (2002), The coastal ocean off Oregon and northern California during the 1997-9 El Niño, *Progress in Oceanography*, *54*, 311-341, doi:10.1016/S0079-6611(02)00056-3.

Huyer, A., R. L. Smith, and T. Paluszkiewicz (1987), Coastal upwelling off Peru during normal and El Niño times, 1981–1984, *Journal of Geophysical Research: Oceans*, *92*(C13), 14297-14307, doi:10.1029/JC092iC13p14297.

Jacox, M. G., J. Fiechter, A. M. Moore, and C. A. Edwards (2015), ENSO and the California Current coastal upwelling response, *Journal of Geophysical Research: Oceans*, *120*, 1691-1702, doi:10.1002/ 2014JC010650.

Jacox, M. G., E. L. Hazen, K. D. Zaba, D. L. Rudnick, C. A. Edwards, A. M. Moore, and S. J. Bograd (2016), Impacts of the 2015–2016 El Niño on the California Current

System: Early assessment and comparison to past events, *Geophysical Research Letters*, *43*, 7072-7080, doi:10.1002/ 2016GL069716.

Jacox, M. G., A. M. Moore, C. A. Edwards, and J. Fiechter (2014), Spatially resolved upwelling in the California Current System and its connections to climate variability, *Geophysical Research Letters*, *41*, 3189-3196, doi:10.1002/2014gl059589.

Kahru, M., E. Di Lorenzo, M. Manzano-Sarabia, and B. G. Mitchell (2012), Spatial and temporal statistics of sea surface temperature and chlorophyll fronts in the California Current, *Journal of Plankton Research*, *34*(9), 749-760, doi:10.1093/plankt/fbs010.

Kahru, M., M. G. Jacox, and M. D. Ohman (2018), GCE1: Decrease in the frequency of oceanic fronts and surface chlorophyll concentration in the California Current System during the 2014-2016 northeast Pacific warm anoamlies, *Deep-Sea Research I*, *140*, 4-13, doi:10.1016/j.dsr.2018.04.007.

Karnauskas, K. B., A. J. Busalacchi, and R. Murtugudde (2008), Low-frequency variability and remote forcing of gap winds over the east Pacific warm pool, *Journal of climate*, *21*(19), 4901-4918, doi:10.1175/2008JCLI1771.1.

Kessler, W. S. (2006), The circulation of the eastern tropical Pacific: A review, *Progress in Oceanography*, *69*, 181-217, doi:10.1016/j.pocean.2006.03.009.

Kosro, P. M., and A. Huyer (1986), CTD and velocity surveys of seaward jets off northern California, July 1981 and 1982, *Journal of Geophysical Research*, *91*(C6), 7680-7690, doi:10.1029/JC091iC06p07680.

Kostianoy, A. G., and J. R. E. Lutjeharms (1999), Atmospheric effects in the Angola-Benguela frontal zone, *Journal of Geophysical Research: Oceans*, *104*(C9), 20963-20970, doi:10.1029/1999jc900017.

Kurian, J., F. Colas, X. Capet, J. C. McWilliams, and D. B. Chelton (2011), Eddy properties in the California Current System, *Journal of Geophysical Research*, *116*, C08027, doi:10.1029/2010jc006895.

Legeckis, R. (1988), Upwelling off the Gulfs of Panama and Papagayo in the tropical Pacific during March 1985, *Journal of Geophysical Research: Oceans*, *93*(C12), 15485-15489, doi:10.1029/JC093iC12p15485.

Lehahn, Y., F. d'Ovidio, M. Lévy, Y. Amitai, and E. Heifet (2011), Long range transport of a quasi isolated chlorophyll patch by an Agulhas ring, *Geophysical Research Letters*, *38*, L16610, doi:10.1029/2011GL048588.

Lentz, S. J. (1993), The accuracy of tide-gauge measurements at subtidal frequencies, *Journal of atmospheric and oceanic technology*, *10*(2), 238-245, doi:10.1175/1520-0426(1993)010<0238:TAOTGM>2.0.CO;2.

Letelier, J., O. Pizarro, and S. Nuñez (2009), Seasonal variability of coastal upwelling and the upwelling front off central Chile, *Journal of Geophysical Research: Oceans*, *114*(C12), doi:10.1029/2008JC005171.

Liang, J. H., J. C. McWilliams, and N. Gruber (2009), High-frequency response of the ocean to mountain gap winds in the northeastern tropical Pacific, *Journal of Geophysical Research: Oceans*, *114*(C12), doi:10.1029/2009JC005370.

Lovecchio, E., N. Gruber, and M. Münnich (2018), Mesoscale contribution to the long-range offshore transport of organic carbon from the Canary Upwelling System to

the open North Atlantic, *Biogeosciences*, *15*, 5061-5091, doi:10.5194/bg-15-5061-2018.

Lynn, R. J., and J. J. Simpson (1987), The California Current System: The Seasonal Variability of its Physical Characteristics, *Journal of Geophysical Research*, *92*(C12), 12947-12966, doi:10.1029/JC092iC12p12947.

Macias, D., M. Landry, R., A. Gershunov, A. J. Miller, and P. J. S. Franks (2012), Climatic control of upwelling variability along the western North-American coast, *PloS one*, *7*(1), e30436, doi:10.1371/journal.pone.0030436.

Marchesiello, P., J. C. McWilliams, and A. Shchepetkin (2003), Equilibrium structure and dynamics of the California Current System, Journal of Physical Oceanography, 33, 753-783, doi:10.1175/1520-0485(2003)33<753:esadot>2.0.co;2.

Martinez-Diaz-De-Leon, A., I. Robinson, D. Ballestero, and E. Coen (1999), Wind driven ocean circulation features in the Gulf of Tehuantepec, Mexico, revealed by combined SAR and SST satellite sensor data, *International Journal of Remote Sensing*, *20*(8), 1661-1668, doi:10.1080/014311699212669.

Mauzole, Y., H. Torres, and L. L. Fu (2020), Patterns and Dynamics of SST Fronts in the California Current System, *Journal of Geophysical Research: Oceans*, *125*(2), e2019JC015499, doi:10.1029/2019JC015499.

Mavor, T. P., and J. J. Bisagni (2001), Seasonal variability of sea-surface temperature fronts on Georges Bank, *Deep-Sea Research II*, *48*, 215-243, doi:10.1016/S0967-0645(00)00120-X.

McWilliams, J. C. (2016), Submesoscale currents in the ocean, *Proceedings of the Royal Society A*, *472*, 20160117, doi:10.1098/rspa.2016.0117.

Medeiros, P. M., M. Seidel, N. D. Ward, E. J. Carpenter, H. R. Gomes, J. Niggemann, A. V. Krusche, J. E. Richey, P. L. Yager, and T. Dittmar (2015), Fate of the Amazon River dissolved organic matter in the tropical Atlantic Ocean, *Global Biogeochemical Cycles*, *29*(5), 677-690, doi:10.1002/2015GB005115.

Medeiros, P. M., E. L. Sikes, B. Thomas, and K. H. Freeman (2012), Flow discharge influences on input and transport of particulate and sedimentary organic carbon along a small temperate river, *Geochimica et Cosmochimica Acta*, *77*, 317-334, doi:10.1016/j.gca.2011.11.020.

Mesias, J. M., R. P. Matano, and P. T. Strub (2003), Dynamical analysis of the upwelling circulation off central Chile, *Journal of Geophysical Research: Oceans*, *108*(C3), doi:10.1029/2001JC001135.

Meunier, T., E. D. Barton, B. Barreiro, and R. Torres (2012), Upwelling filaments off Cap Blanc: Interaction of the NW African upwelling current and the Cape Verde frontal zone eddy field?, *Journal of Geophysical Research: Oceans*, *117*(C8), doi:10.1029/2012JC007905.

Meyers, S. D., A. Melsom, G. T. Mitchum, and J. J. O'Brien (1998), Detection of the fast Kelvin wave teleconnection due to El Niño-Southern Oscillation, *Journal of Geophysical Research: Oceans*, *103*(C12), 27655-27663, doi:10.1029/98jc02402.

Mooers, C. N. K., and A. R. Robinson (1984), Turbulent jets and eddies in the California Current and inferred cross-shore transports, *Science*, *223*(4631), 51-53, doi:10.1126/science.223.4631.51.

Nagai, T., N. Gruber, H. Frenzel, Z. Lachkar, J. C. McWilliams, and G.-K. Plattner (2015), Dominant role of eddies and filaments in the offshore transport of carbon and nutrients in the California Current System, *Journal of Geophysical Research: Oceans*, *120*, 5318-5341, doi:10.1002/2015jc010889.

Nieto, K., H. Demarcq, and S. McClatchie (2012), Mesoscale frontal structures in the Canary Upwelling System: New front and filament detection algorithms applied to spatial and temporal patterns, *Remote Sensing of Environment*, *123*, 339-346, doi:10.1016/j.rse.2012.03.028.

Oerder, V., J. P. Bento, C. E. Morales, S. Hormazabal, and O. Pizarro (2018), Coastal upwelling front detection off central Chile (36.5–37 S) and spatio-temporal variability of frontal characteristics, *Remote sensing*, *10*(5), 690, doi:10.3390/rs10050690.

Overland, J. E., and R. Preisendorfer (1982), A significance test for principal components applied to a cyclone climatology, *Monthly Weather Review*, *110*(1), 1-4, doi:10.1175/1520-0493(1982)110<0001:ASTFPC>2.0.CO;2.

Pegliasco, C., A. Chaigneau, and R. Morrow (2015), Main eddy vertical structures observed in the four major Eastern Boundary Upwelling Systems, *Journal of Geophysical Research: Oceans*, *120*, 6008-6033, doi:10.1002/2015jc010950.

Peliz, Á., T. L. Rosa, A. M. P. Santos, and J. L. Pissarra (2002), Fronts, jets, and counter-flows in the Western Iberian upwelling system, *Journal of marine systems*, *35*(1-2), 61-77, doi:10.1016/S0924-7963(02)00076-3.

Penven, P., C. Roy, A. Colin de Verdière, and J. Largier (2000), Simulation of a coastal jet retention process using a barotropic model, edited, pp. 615-634, doi:10.1016/S0399-1784(00)01106-3.

Putrasahan, D. A., A. J. Miller, and H. Seo (2013), Regional coupled ocean–atmosphere downscaling in the Southeast Pacific: impacts on upwelling, mesoscale air–sea fluxes, and ocean eddies, *Ocean Dynamics*, *63*(5), 463-488, doi:10.1007/s10236-013-0608-2.

Ramp, S. R., P. F. Jessen, K. H. Brink, P. P. Niiler, F. L. Daggett, and J. S. Best (1991), The physical structure of cold filaments near Point Arena, California, during June 1987, *Journal of Geophysical Research: Oceans*, *96*(C8), 14859-14883, doi:10.1029/91JC01141.

Relvas, P., and E. D. Barton (2002), Mesoscale patterns in the Cape Sao Vicente (Iberian peninsula) upwelling region, *Journal of Geophysical Research: Oceans*, *107*(C10), 28-21-28-23, doi:10.1029/2000JC000456.

Røed, L. P., and X. B. Shi (1999), A numerical study of the dynamics and energetics of cool filaments, jets, and eddies off the Iberian Peninsula, *Journal of Geophysical Research: Oceans*, *104*(C12), 29817-29841, doi:10.1029/1999JC900175.

Romero-Centeno, R., J. Zavala-Hidalgo, A. Gallegos, and J. J. O'Brien (2003), Isthmus of Tehuantepec wind climatology and ENSO signal, *Journal of Climate*, *16*, 2628-2639, doi:10.1175/1520-0442(2003)016<2628:IOTWCA>2.0.CO;2.

Sangrà, P., et al. (2009), The Canary Eddy Corridor: A major pathway for long-lived eddies in the subtropical North Atlantic, *Deep-Sea Research I*, *56*(12), 2100-2114, doi:10.1016/j.dsr.2009.08.008.

Santos, F., M. Gomez-Gesteira, M. DeCastro, and I. Alvarez (2012), Differences in coastal and oceanic SST trends due to the strengthening of coastal upwelling along the Benguela current system, *Continental Shelf Research*, *34*, 79-86, doi:10.1016/j.csr.2011.12.004.

Satinsky, B. M., B. C. Crump, C. B. Smith, S. Sharma, B. L. Zielinski, M. Doherty, J. Meng, S. Sun, P. M. Medeiros, and J. H. Paul (2014), Microspatial gene expression patterns in the Amazon River Plume, *Proceedings of the National Academy of Sciences*, *111*(30), 11085-11090, doi:10.1073/pnas.1402782111.

Schlax, M. G., and D. B. Chelton (2016), *The "growing method" of eddy identification and tracking in two and three dimensions*, College of Earth, Ocean and Atmospheric Sciences, Oregon State University. Retrieved from http://wombat.coas.oregonstate.edu/eddies/Growing_Method_of_Eddy_Identification_and_Tracking.pdf.

Schwing, F. B., T. Murphree, L. deWitt, and P. M. Green (2002), The evolution of oceanic and atmospheric anomalies in the northeast Pacific during the El Niño and La Niña events of 1995-2001, *Progress in Oceanography*, *54*, 459-491, doi:10.1016/S0079-6611(02)00064-2.

Shaffer, G., O. Pizarro, L. Djurfeldt, S. Salinas, and J. Rutllant (1997), Circulation and low-frequency variability near the Chilean coast: Remotely forced fluctuations during the 1991–92 El Nino, *Journal of Physical Oceanography*, *27*(2), 217-235, doi:10.1175/1520-0485(1997)027<0217:CALFVN>2.0.CO;2.

Small, L. F., and F. G. Prahl (2004), A Particle Conveyor Belt Process in the Columbia River Estuary: Evidence from Chlorophyll *a* and Particulate Organic Carbon, *Estuaries*, *27*(6), 999-1003.

Snyder, M. A., L. C. Sloan, N. S. Diffenbaugh, and J. L. Bell (2003), Future climate change and upwelling in the California Current, *Geophysical Research Letters*, *30*(15), 1823, doi:10.1029/2003GL017647.

Spillane, M., D. Enfield, and J. Allen (1987), Intraseasonal oscillations in sea level along the west coast of the Americas, *Journal of Physical Oceanography*, *17*(3), 313-325, doi:10.1175/1520-0485(1987)017<0313:IOISLA>2.0.CO;2.

Steenburgh, W. J., D. M. Schultz, and B. A. Colle (1998), The structure and evolution of gap outflow over the Gulf of Tehuantepec, Mexico, *Monthly Weather Review*, *126*, 2673-2691, doi:10.1175/1520-0493(1998)126<2673:TSAEOG>2.0.CO;2.

Stegmann, P. M., and F. Schwing (2007), Demographics of mesoscale eddies in the California Current, *Geophysical Research Letters*, *34*, L14602, doi:10.1029/2007GL029504.

Stramma, L., T. Fischer, D. S. Grundle, G. Krahmann, H. W. Bange, and C. A. Marandino (2016), Observed El Niño conditions in the eastern tropical Pacific in October 2015, *Ocean Science*, *12*, 861-873, doi:10.5194/os-12-861-2016.

Stramski, D., et al. (2008), Relationships between the surface concentration of particulate organic carbon and optical properties in the eastern South Pacific and eastern Atlantic Oceans, *Biogeosciences*, *5*, 171-201, doi:10.5194/bg-5-171-2008.

Strub, P. T., J. S. Allen, A. Huyer, R. L. Smith, and R. Beardsley (1987), Seasonal cycles of currents, temperatures, winds, and sea level over the northeast Pacific

continental shelf: 35 N to 48 N, *Journal of Geophysical Research: Oceans*, *92*(C2), 1507-1526, doi:10.1029/JC092iC02p01507.

Strub, P. T., V. Combes, F. A. Shillington, and O. Pizarro (2013), Currents and Processes along the Eastern Boundaries, in *Ocean Circulation and Climate: A 21st Century Perspective*, edited by G. Siedler, S. M. Griffies, J. Gould and J. A. Church, pp. 339-384, Academic Press, doi:10.1016/b978-0-12-391851-2.00014-3.

Strub, P. T., and C. James (2000), Altimeter-derived variability of surface velocities in the California Current System: 2. Seasonal circulation and eddy statistics, *Deep-Sea Research II*, *47*, 831-870, doi:10.1016/S0967-0645(99)00129-0.

Strub, P. T., and C. James (2002), The 1997–1998 oceanic El Niño signal along the southeast and northeast Pacific boundaries—an altimetric view, *Progress in Oceanography*, *54*, 439-458, doi:10.1016/S0079-6611(02)00063-0.

Strub, P. T., and C. James (2002), Altimeter-derived surface circulation in the large-scale NE Pacific Gyres. Part 2: 1997-1998 El Niño anomalies, *Progress in Oceanography*, *53*, 185-214, doi:10.1016/S0079-6611(02)00030-7.

Strub, P. T., C. James, V. Montecino, J. A. Rutllant, and J. L. Blanco (2019), Ocean circulation along the southern Chile transition region (38–46 S): Mean, seasonal and interannual variability, with a focus on 2014–2016, *Progress in oceanography*, *172*, 159-198, doi:10.1016/j.pocean.2019.01.004.

Strub, P. T., P. M. Kosro, and A. Huyer (1991), The Nature of the Cold Filaments in the California Current System, *Journal of Geophysical Research*, *96*, 14,743-714,768.

Strub, P. T., J. M. Mesias, V. Montecino, J. Rutllant, and S. Salinas (1998), Coastal ocean circulation off western South America, in *The Sea*, edited by A. R. Robinson and K. H. Brink, pp. 273-313, John Wiley & Sons.

Sullivan, B. E., F. G. Prahl, L. F. Small, and P. A. Covert (2001), Seasonality of phytoplankton production in the Columbia river: A natural or anthropogenic pattern?, *Geochimica et Cosmochimica Acta*, *65*(7), 1125-1139.

Sun, F., and J. Y. Yu (2006), Impacts of Central America gap winds on the SST annual cycle in the eastern Pacific warm pool, *Geophysical research letters*, *33*(6), doi:10.1029/2005GL024700.

Sydeman, W. J., M. García-Reyes, D. S. Schoeman, R. R. Rykaczewski, S. A. Thompson, B. A. Black, and S. J. Bograd (2014), Climate change and wind intensification in coastal upwelling ecosystems, *Science*, *345*(6192), 77-80, doi:10.1126/science.1250830.

Trasviña, A., E. Barton, J. Brown, H. Velez, P. M. Kosro, and R. L. Smith (1995), Offshore wind forcing in the Gulf of Tehuantepec, Mexico: The asymmetric circulation, *Journal of Geophysical Research: Oceans*, *100*(C10), 20649-20663, doi:10.1029/95JC01283.

Ullman, D. S., and P. C. Cornillon (1999), Satellite-derived sea surface temperature fronts on the continental shelf off the northeast U.S. coast, *Journal of Geophysical Research: Oceans*, *104*(C10), 23459-23478, doi:10.1029/1999jc900133.

Ulloa, O., R. Escribano, S. Hormazabal, R. A. Quiñones, R. R. González, and M. Ramos (2001), Evolution and biological effects of the 1997-98 El Niño in the upwelling

ecosystem off northern Chile, *Geophysical Research Letters*, *28*(8), 1591-1594, doi:10.1029/2000gl011548.

Vazquez-Cuervo, J., B. Dewitte, T. M. Chin, E. M. Armstrong, S. Purca, and E. Alburqueque (2013), An analysis of SST gradients off the Peruvian Coast: The impact of going to higher resolution, *Remote Sensing of Environment*, *131*, 76-84, doi:10.1016/j.rse.2012.12.010.

Veitch, J., J. Hermes, T. Lamont, P. Penven, and F. Dufois (2018), Shelf-edge jet currents in the southern Benguela: A modelling approach, *Journal of Marine Systems*, *188*, 27-38, doi:10.1016/j.jmarsys.2017.09.003.

Veitch, J. A., and P. Penven (2017), The role of the Agulhas in the Benguela Current system: A numerical modeling approach, *Journal of Geophysical Research: Oceans*, *122*(4), 3375-3393, doi:10.1002/2016JC012247.

Walsh, J. J. (1977), A biological sketchbook for an eastern boundary current, in *The Sea*, edited by E. D. Goldbert, I. N. McCave, J. J. O'Brien and J. H. Steele, pp. 923-968, Wiley-Interscience, Hoboken, N. J.

Wang, Y., and R. M. Castelao (2016), Variability in the coupling between sea surface temperature and wind stress in the global coastal ocean, *Continental Shelf Research*, *125*, 88-96, doi:10.1016/j.csr.2016.07.011.

Wang, Y., R. M. Castelao, and Y. Yuan (2015), Seasonal variability of alongshore winds and sea surface temperature fronts in Eastern Boundary Current Systems, *Journal of Geophysical Research: Oceans*, *120*, 2385-2400, doi:10.1002/2014jc010379.

Wang, Y., J. Liu, H. Liu, P. Lin, Y. Yuan, and F. Chai (2021), Seasonal and interannual variability in the sea surface temperature front in the eastern Pacific Ocean,

Journal of Geophysical Research: Oceans, e2020JC016356, doi:10.1029/2020JC016356.

Woodson, C. B., and S. Y. Litvin (2015), Ocean fronts drive marine fishery production and biogeochemical cycling, *Proceedings of the National Academy of Sciences of the United States of America*, *112*(6), 1710-1715, doi:10.1073/pnas.1417143112.

Xiu, P., F. Chai, E. N. Curchitser, and F. S. Castruccio (2018), Future changes in coastal upwelling ecosystems with global warming: The case of the California Current System, *Scientific Reports*, *8*, 2866, doi:10.1038/s41598-018-21247-7.

Yuan, Y., and R. M. Castelao (2017), Eddy-induced sea surface temperature gradients in Eastern Boundary Current Systems, *Journal of Geophysical Research: Oceans*, *122*, 4791-4801, doi:10.1002/2017JC012735.

APPENDIX A

SUPPLEMENTARY MATERIAL FOR CHAPTER 2

OFFSHORE TRANSPORT OF PARTICULATE ORGANIC CARBON IN THE CALIFORNIA CURRENT SYSTEM BY MESOSCALE EDDIES

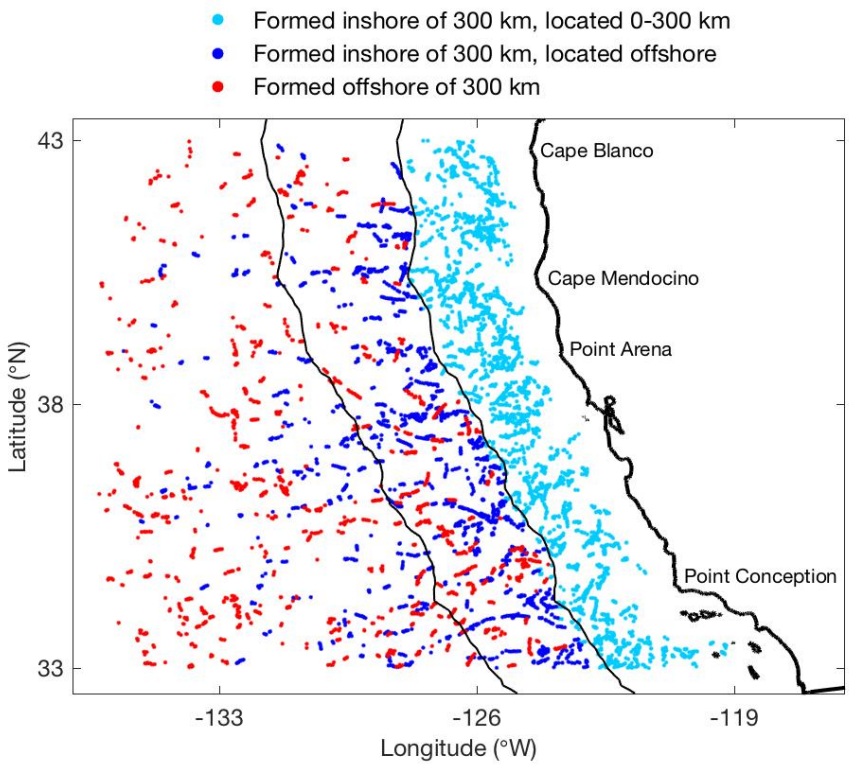

Figure A.1. Locations of cyclonic eddy occurrences in the California Current System under clear-sky conditions. Cyclonic eddy occurrences identified in the eddy dataset (Chelton et al., 2011) with at least 90% particulate organic carbon pixel coverage inside one eddy radius and 75% coverage inside two radii. Thin black lines mark 300 and 600 km from the coast.

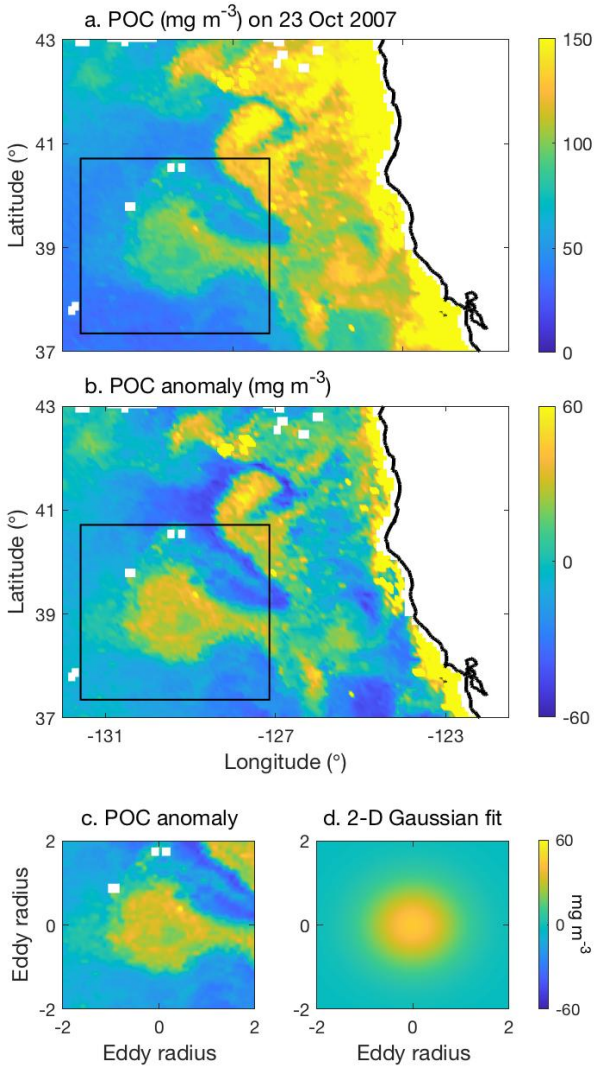

Figure A.2. Procedure for extracting the particulate organic carbon anomaly inside eddies. (a) Particulate organic carbon (POC) and (b) POC anomaly in the California Current System on 23 October 2007. Black box marks the region within 2 by 2 eddy radii from the eddy center, as identified by altimetry (Chelton et al., 2011). (c) POC anomaly extracted within the black box in panel b. (d) POC anomaly based on 2-D Gaussian fit (Yuan and Castelao, 2017) to the field in panel c (see Methods for details).

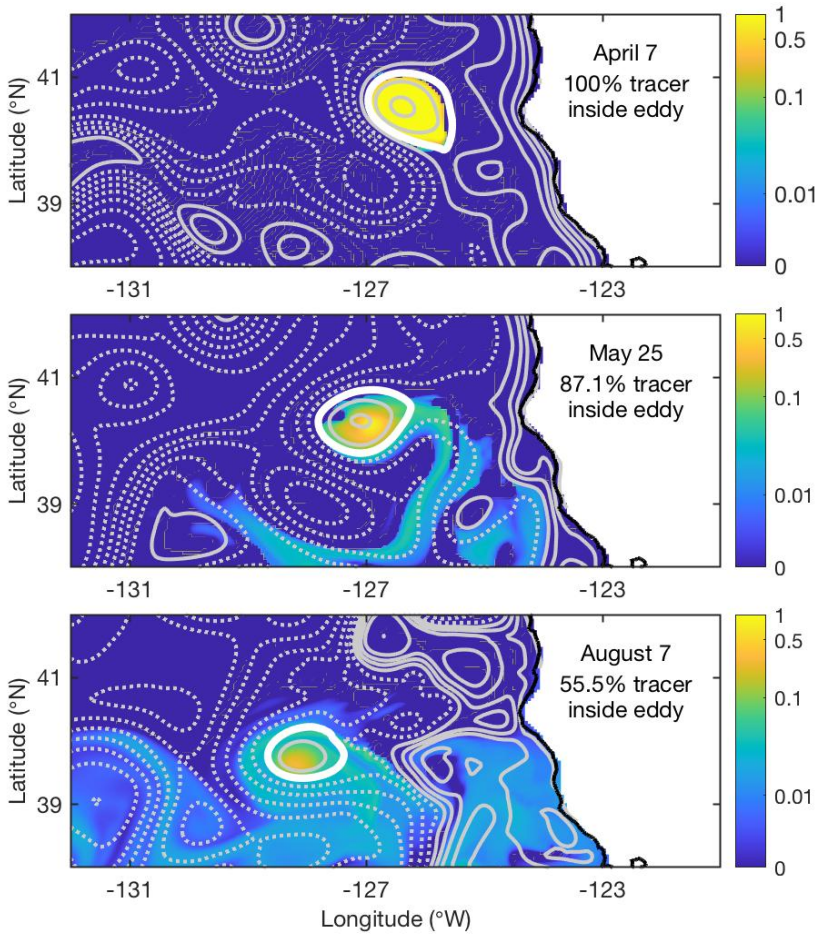

Figure A.3. Model simulation of eddy transporting coastal water. Example of model simulation of cyclonic eddy using a passive tracer to track eddy lateral transport. Sea surface height is shown by grey contours at 4 cm intervals. Solid contours are negative. Thick white circle marks the boundary of the eddy in each snapshot. The fraction of the tracer that is located in the eddy interior (top 400 m) as the eddy propagates westward is also given.

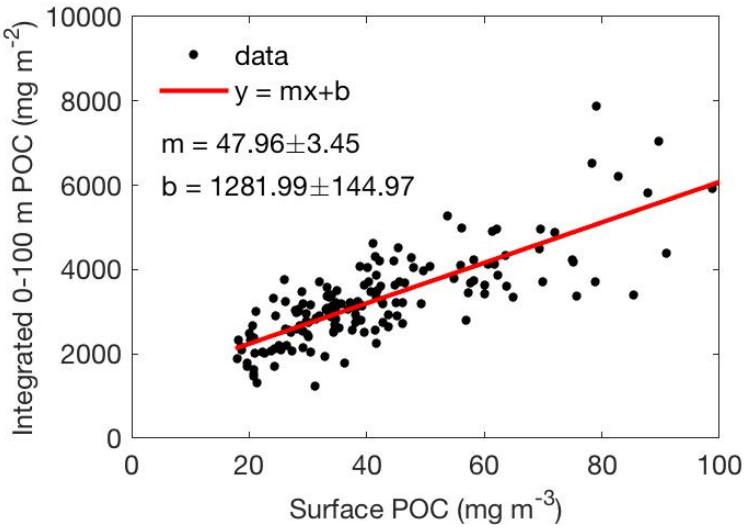

Figure A.4. Relationship between in situ surface particulate organic carbon and integrated particulate organic carbon in top 100 m. In situ particulate organic carbon concentrations measured in the California Current System between 2006-2016 (Aluwihare, 2018) integrated from the surface to 100 m depth (mg m^{-2}) and correlated with concentrations at the surface (mg m^{-3}). Red line shows the linear fit (see Methods).

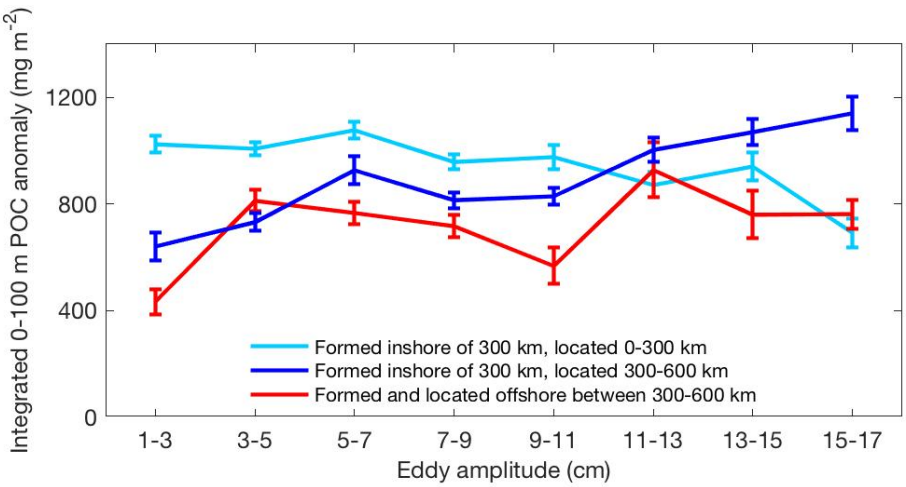

Figure A.5. Integrated particulate organic carbon anomaly in top 100 m. Mean integrated particulate organic carbon anomaly (mg m^{-2}) in top 100 m and standard error within one eddy radius calculated using the linear relationship shown in Supplementary Fig. 4 and grouped by eddy amplitude.

Table A.1. General characteristics of cyclonic eddies with lifetime longer than 4 weeks generated within 600 km from the coast in the California Current System (1993-2015) from an existing global eddy dataset (Chelton et al., 2011).

	Cyclones generated and located 0-300 km from the coast	**Cyclones generated 0-300 km and located 300-600 km from the coast**	**Cyclones generated and located 300-600 km from the coast**
Number of eddies	110	138	121
Amplitude (cm)	5.95 ± 2.94	8.42 ± 4.06	6.77 ± 3.70
Radius (km)	63.77 ± 19.29	83.02 ± 24.88	72.86 ± 24.25
Rotational speed (cm s^{-1})	17.51 ± 5.34	19.42 ± 6.23	16.71 ± 5.88

APPENDIX B

SUPPLEMENTARY MATERIAL FOR CHAPTER 3

OFFSHORE ENRICHMENT OF PARTICULATE ORGANIC CARBON BY MESOSCALE EDDIES IN EASTERN BOUNDARY CURRENT SYSTEMS

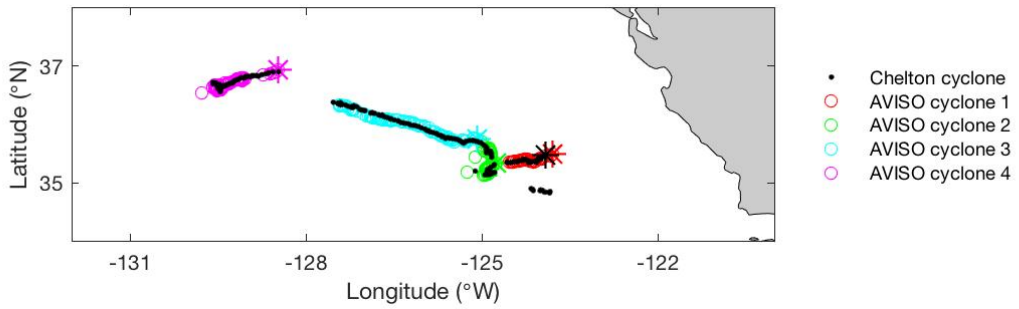

Figure B.1. Example of a cyclonic eddy track in the Chelton et al. (2011) fourth release of the global mesoscale eddy dataset compared to the AVISO+ dataset (https://www.aviso.altimetry.fr/). The dots and circles mark the center point of the eddy at daily intervals along its track. The "Chelton" dataset identifies and tracks one cyclonic eddy, while this same eddy is identified as multiple different eddies in the "AVISO" dataset. Analysis of sea surface height fields show that this is one cyclonic eddy. The different cyclones that were identified in the "AVISO" dataset appear to occur when the eddy interacts with other mesoscale features as it propagates offshore, making the tracking difficult. The jump in the "Chelton" track around -128°W occurs as the cyclonic eddy becomes elongated offshore, so the algorithm marks the center of the eddy farther offshore. This example shows imperfections in both tracking algorithms when eddies change shape, merge, or interact with other eddies as they propagate offshore (as seen in the sea surface height fields).

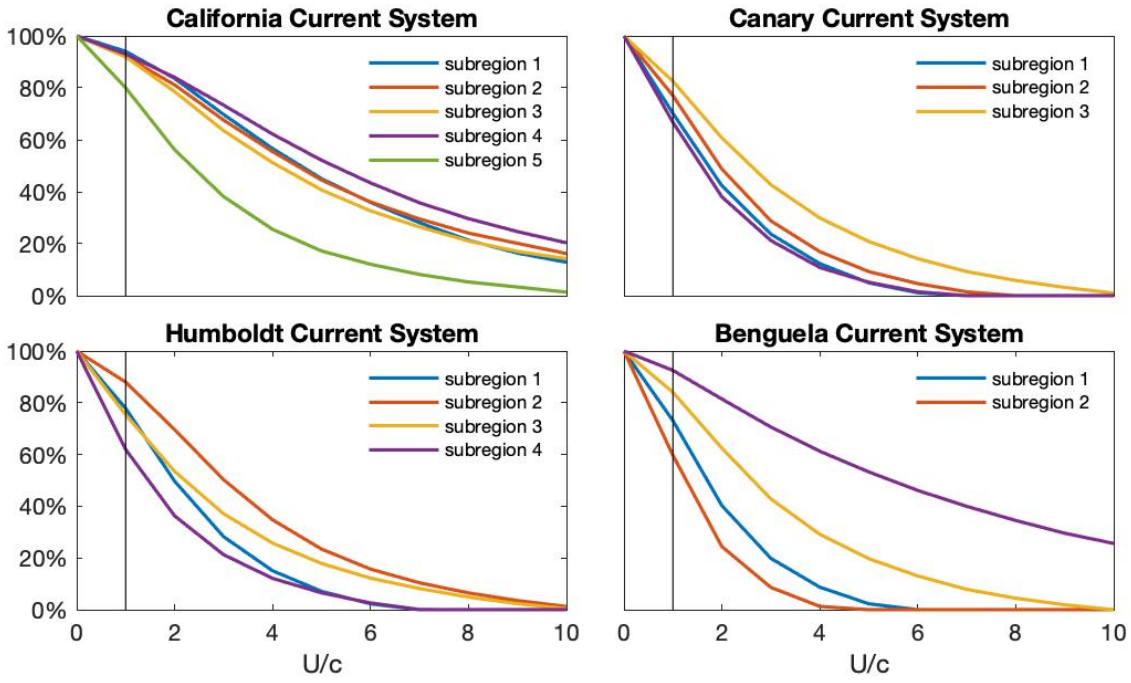

Figure B.2. Percentage of cyclonic eddies located 0-300 km from the coast whose nonlinearity parameter (U/c) is greater than the value on the x-axis in each subregion in the EBCS. The vertical black line marks U/c = 1. The subregions in each subplot correspond to the subregions in Table 3.1.

APPENDIX C

SUPPLEMENTARY MATERIAL FOR CHAPTER 4

INFLUENCE OF THE EL NIÑO-SOUTHERN OSCILLATION ON SST FRONTS ALONG THE WEST COASTS OF NORTH AND SOUTH AMERICA

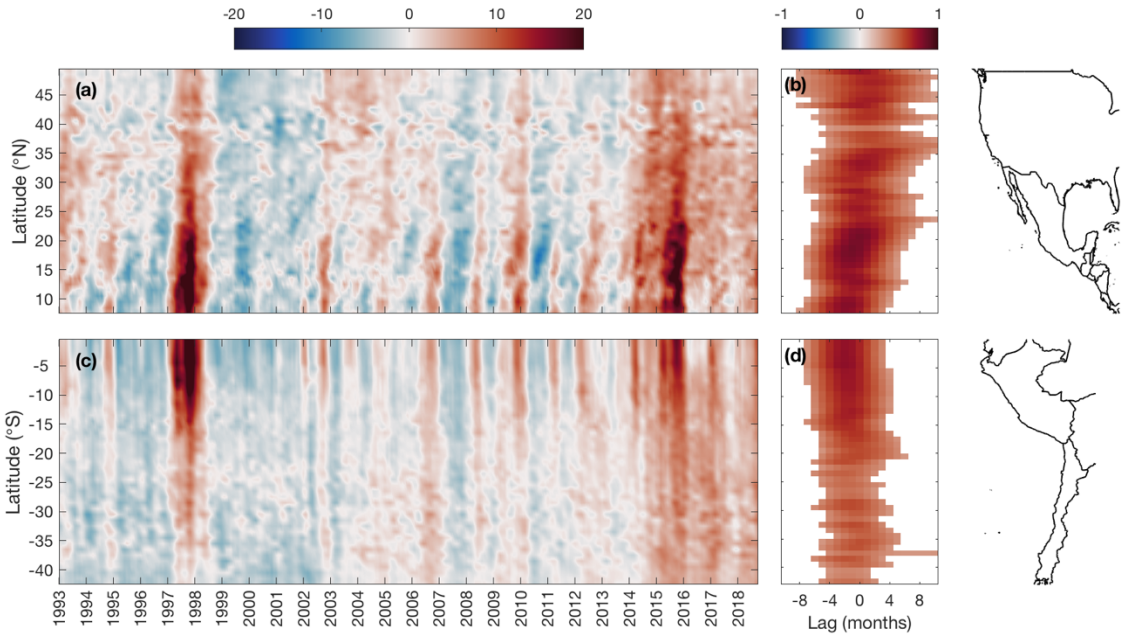

Figure C.1. (a, c) The three-month running mean of sea level anomaly (SLA; cm) computed by subtracting the climatological monthly mean (2003-2013) from each individual month using SLA produced and distributed by the Copernicus Climate Change Service. Anomalies were averaged within 0-300 km of the coastline in 1° latitude boxes. (b, d) Lagged correlation between SLA anomalies in panels a and c and the ONI (Figure 4.2) at each latitude. The x-axis represents the months by which SLA lags the ONI (positive lag is defined as the changes in SLA occurring after the peak in the ONI). Only significant correlations are shown.

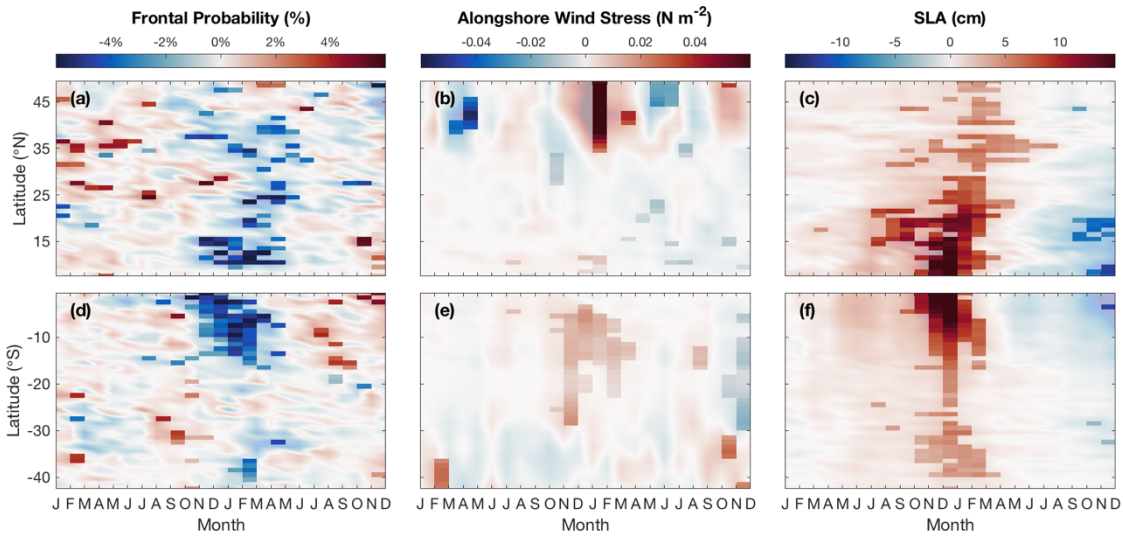

Figure C.2. 2-year composite differences computed by subtracting the neutral composite from the composite for moderate to strong El Niño events (defined as ONI ≥ 1°C for at least 3 consecutive months) in each 1° latitude box within 0-300 km offshore for (a, d) mean SST frontal probability (%), (b, e) mean alongshore wind stress (N m^{-2}), and (c, f) mean SLA (cm) along the west coasts of North (a, b, d) and South (d, e, f) America. Light shading (transparency of 60%) indicates values that are not significant (p-value > 0.05). The El Niño (neutral) composites for frontal probability, alongshore wind stress, and SLA included 8 (10), 6 (9), and 5 (6) events, respectively. The same data are shown in Figure 8, but with significance levels determined using a p-value of 0.1.

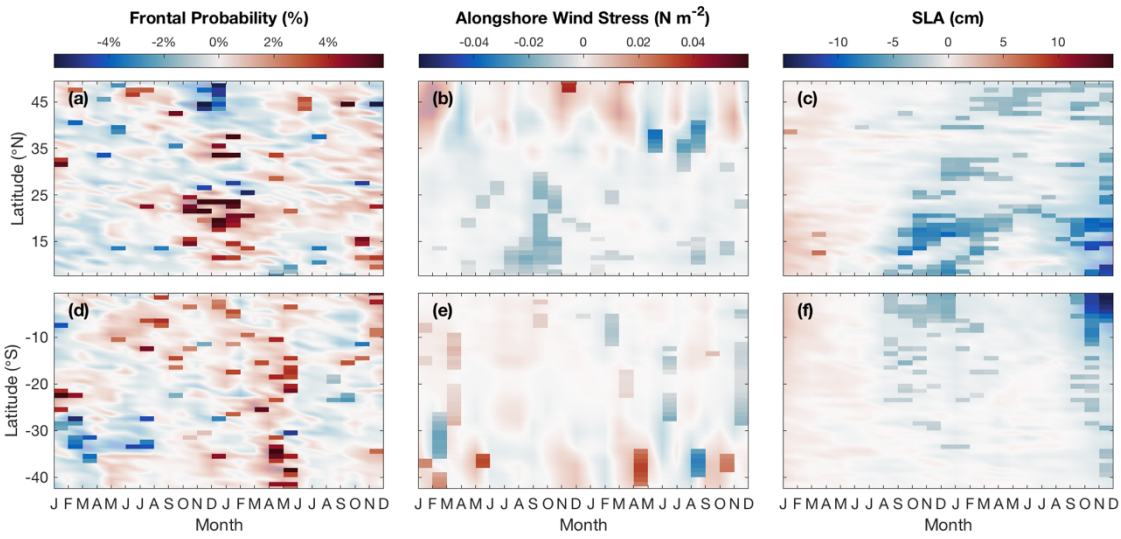

Figure C.3. 2-year composite differences computed by subtracting the neutral composite from the composite for moderate to strong La Niña events (defined as ONI ≤ -1°C for at least 3 consecutive months) in each 1° latitude box within 0-300 km offshore for (a, d) mean SST frontal probability (%), (b, e) mean alongshore wind stress (N m^{-2}), and (c, f) mean SLA (cm) along the west coasts of North (a, b, d) and South (d, e, f) America. Light shading (transparency of 60%) indicates values that are not significant (p-value > 0.05). The La Niña (neutral) composites for frontal probability, alongshore wind stress, and SLA included 7 (10), 7 (9), and 6 (6) events, respectively. The same data are shown in Figure 9, but with significance levels determined using a p-value of 0.1.